DOCTORAATSPROEFSCHRIFT

2001

Faculteit Wetenschappen

# Looking at molecular multidomain behaviour of polymer systems through NMR-relaxometry

Proefschrift voorgelegd tot het behalen van de graad van
Doctor in de Wetenschappen, richting Scheikunde,
te verdedigen door

Liesbet STORME

Promotoren : Prof. Dr. J. Gelan
Dr. P. Adriaensens

LIMBURGS
UNIVERSITAIR
CENTRUM
IN HET CENTRUM VAN DE KENNIS

**2001**

**Faculteit Wetenschappen**

# Looking at molecular multidomain behaviour of polymer systems through NMR-relaxometry

Proefschrift voorgelegd tot het behalen van de graad van
Doctor in de Wetenschappen, richting Scheikunde,
te verdedigen door

Liesbet STORME

Promotoren : Prof. Dr. J. Gelan
Dr. P. Adriaensens

LIMBURGS
UNIVERSITAIR
CENTRUM
IN HET CENTRUM VAN DE KENNIS

According to the guidelines of the Limburgs Universitair Centrum,
a copy of this publication
has been filed in the Royal Library Albert I, Brussels,as publication
D/2001/2451/40

*In eerste instantie leek doctoreren voor mij een werk van lange duur, vier jaar lang proberen om de NMR techniek in al zijn facetten onder de knie te krijgen en er eveneens wetenschappelijke resultaten mee behalen. Het eindpunt leek dan ook ver weg, maar de voorbije jaren zijn in sneltreinvaart voorbijgegaan. Het bleek echter geen opdracht voor mij alleen te zijn maar voor een hele ploeg mensen die elk op een andere manier een beetje bijgedragen hebben tot dit werk.*

*Prof. Dr. Jan Gelan, de drijvende kracht achter het NMR onderzoek heeft mij de mogelijkheid aangeboden om in Diepenbeek te doctoreren. Het NMR onderzoek bleek algauw een boeiend en divers domein waarin vele kansen en mogelijkheden aangeboden werden. Jan, bedankt voor de enthousiaste begeleiding van dit onderzoekswerk niet alleen binnen het universiteitsleven maar ook samen met de industriële wereld.*

*Dr. Peter Adriaensens, misschien wel het meest essentiële onderdeel van 'onze' NMR toestellen, steeds gedreven om iets nieuws en iets extra uit te proberen, is erin geslaagd om het abstracte van NMR steeds eenvoudig uit te leggen. Niet alleen de metingen moesten precies en gestructureerd gebeuren, ook van de verwerkingen en de verslagen werd een precisie vereist die geleid heeft tot een verdere ontwikkeling van mijn wetenschappelijke geest en uiteindelijk tot het behalen van deze resultaten. Peter, bedankt voor het geduldig aanbrengen van de NMR geheimen en het zoeken naar de oplossingen van de problemen die ons werden voorgelegd.*

*Prof. Dr. Dirk Vanderzande, Dr. Laurence Lutsen en Dr. Robert Carleer, leiders van bloeiende onderzoeksgroepen, ben ik dankbaar voor de getoonde interesse in mijn onderzoek. Het fundamenteel onderzoek werd door Robert dichter bij de toepassingen gebracht dankzij de nauwe contacten met en de opdrachten vanuit de bedrijven. Robert zijn uitgebreide kennis bracht ons ook vaak een stuk dichter bij de oplossing.*

*Prof. Dr. H. Berghmans en Prof. Dr. F. Du Prez ben ik dankbaar voor de nauwe samenwerking in het kader van het IUAP wat geleid heeft tot deze NMR resultaten, passend in een mooi wetenschappelijk geheel.*

*Prof. Dr. Roel Marissen en Dr. Victor Litvinov van DSM Research hebben eveneens heel wat bijgedragen aan dit werk, niet enkel in de zoektocht naar geschikte materialen om onder mechanische spanning te bestuderen maar vooral door via talrijke wetenschappelijke discussies een grote interesse voor dit onderzoekswerk op te wekken.*

*Dr. Jan D'Haen en Hilde Pellaers stonden steeds paraat om de SEM beelden op te nemen. Ook Ir. Ludo Naelaerts was altijd bereid om rek-spannings curves op te meten.*
*Jos Kaelen ontwierp een gesofistikeerde 'stretching device' wat het mogelijk maakte om unieke beelden van de materialen onder mechanische spanning in de magneet, op te nemen.*
*Koen Van Vinckenroye zorgde niet alleen voor het operationeel houden van onze toestellen, wat niet altijd eenvoudig was, maar was ook een aangename gesprekspartner tijdens het opzetten van de metingen.*
*De administratieve molen wordt uitstekend draaiende gehouden door Christel Rappoort en het SBG secretariaat.*
*De collega's zorgden voor een sfeer die doctoreren bijzonder maakt en die er ook voor zorgde dat de voorbije vier jaar om gevlogen zijn. De NMR collega's, Ben, Anne, Robby, Hilde en vanaf nu ook Roel en de synthetiserende collega's Dirk, Lieve, Veerle, Iris, Stijn, Els, Joachim, Filip, Anja, Iwona, Hugette, Pierre-Henry en Pawel maakten er een levendige en enthousiaste groep van.*
*Veerle, eveneens hartelijk dank voor het efficiënt nalezen van mijn thesis!*
*De ploeg van anorganische scheikunde en de hele FTO ploeg, zorgden steeds voor een aangename babbel tussen de werkuren.*
*Het IUAP ben ik erkentelijk voor de financiële steun.*
*Van mijn ouders, die al die jaren het verloop van mijn studies van nabij volgden, heb ik bijzonder veel steun en aanmoediging gekregen.*
*Een speciaal woord van dank aan Tom, die de evolutie van dit doctoraat van heel dichtbij gevolgd heeft en me altijd heeft bijgestaan.*

# 1

# Introduction to Nuclear Magnetic Resonance Microscopy and Relaxometry

The phenomenon of Nuclear Magnetic Resonance microscopy (NMR) was first observed in 1946 independently by the research groups of Bloch[1] and of Purcell.[2] It has grown enormously in power and versatility since that time, particularly with the introduction of pulsed Fourier Transform (FT) NMR, a technique whose development has been closely linked with the rapid advances made in computer technology and of higher magnetic fields.

NMR is a powerful instrumental method to obtain detailed information on chemical systems at the molecular level. It is mainly known from liquid state NMR as a characterisation tool for synthesists. However, also in the solid state and as imaging method (not only in medicine but also in material science) NMR provides fast, non-invasive and non-destructive tools for research on the structure and dynamic behaviour of molecules. NMR-relaxometry reveals many secrets about the molecular mobility and the miscibility of polymer systems: as a volume average in the solution and solid state and in a localised way by NMR imaging.[3,4,5]

The work in this thesis demonstrates that the possibilities of NMR are unlimited in order to obtain declaration of macroscopic properties on the basis of molecular information through NMR relaxometry.

In this chapter, first a brief introduction of the basic principles of NMR is given. Secondly the possibilities of NMR-relaxometry in liquid state NMR, solid state NMR and NMR imaging are discussed.

## 1.1 The physical basis of NMR microscopy

Most nuclei possess a nuclear or intrinsic angular momentum P. Quantum mechanical considerations show that this angular momentum is quantified:

$$P = h/2\pi\,(I(I + 1))^{1/2} \tag{1.1}$$

I is the angular momentum spin quantum number, simply the nuclear spin and h is Planck's constant. The angular momentum has associated with it a magnetic moment $\mu$:

$$\mu = \gamma\, P \tag{1.2}$$

where $\gamma$ is the gyromagnetic ratio, a proportionality constant typical for the kind of nucleus, and which essentially measures the strength of the nuclear magnets.

From equations 1.1 and 1.2 it is shown that only nuclei with $I \neq 0$ have a nuclear magnetic moment. These nuclei contain an odd number of protons and/or an odd number of neutrons. In the presence of an external magnetic field the angular momentum takes up an orientation such that its component $P_z$ along the direction of the field is an integral or half-integral multiple of $h/2\pi$:

$$P_z = m\, h/2\pi \tag{1.3}$$

m is the magnetic quantum number and can take any of the values m = I, I-1, ... -I. There are (2I + 1) different values of m and consequently an equal number of possible orientations of the magnetic moment in the magnetic field, each having a characteristic energy.

Among all nuclei, $^1H$ and $^{13}C$ are of main interest, as their resonances are the most important ones for determining the structures of organic molecules and polymers. These nuclei with I =1/2, can take up two orientations, a low energy orientation aligned with the applied field and a high energy orientation opposed to the applied field (two Zeeman levels) (Figure 1.1). The difference in energy is given by:

$$\Delta E = h\gamma B_0/2\pi \tag{1.4}$$

where $\gamma$ is the gyromagnetic ratio and $B_0$ is the strength of the applied magnetic field.

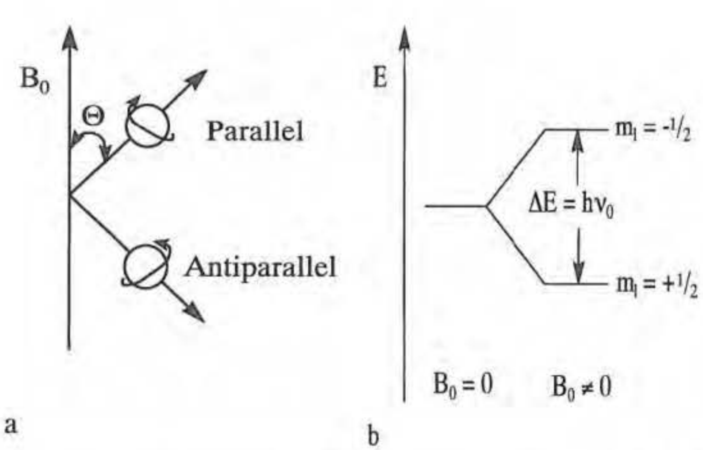

*Figure 1.1*: *(a) Orientations of the $\mu$ vectors in a magnetic field $B_0$ of a nuclei with a nuclear spin $I = {}^1/_2$ ($\Theta = 54° 44'$), parallel ($m_I = +{}^1/_2$) or anti-parallel ($m_I = -{}^1/_2$). (b) Energy scheme of a nuclei ($I = {}^1/_2$) in a magnetic field.*

When a nucleus with a magnetic moment $\mu$ is brought in a uniform magnetic field $B_0$, it starts to precess around the field vector (Figure 1.2). The precession frequency $\omega_L$ is called the Larmor frequency and depends on the strength of the main magnetic field $B_0$ and the nature of the nucleus in question:

$$\omega_L = \gamma B_0 \tag{1.5}$$

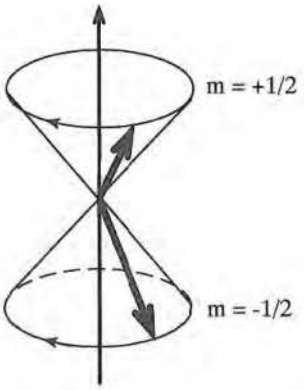

*Figure 1.2: Precession of nuclear dipoles with spin I = 1/2 around a double cone; the angle of the cone is 54° 44".*

The nuclei are spread over the two energy levels. The number of nuclei in the low energy state ($N_\alpha$) and the number in the high energy state ($N_\beta$) will differ by an amount determined by the Boltzmann distribution:

$$N_\beta/N_\alpha = \exp(-\Delta E/kT) \tag{1.6}$$

The sum of all the contributing magnetic moments $\mu_i$ of the individual nuclei results in a resultant magnetisation $M_0$ along the z-axis (Figure 1.3).

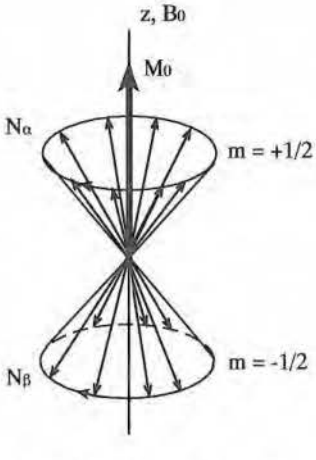

*Figure 1.3: Distribution of the precessing nuclear dipoles around the double cone. Because $N_\alpha > N_\beta$ there is a resultant macroscopic magnetisation $M_0$.*

In a nuclear magnetic resonance experiment transitions are induced from the low to the high energy level by irradiating the nuclei with a superimposed radiofrequency (rf) field $B_1$, applied perpendicular to the original field $B_0$. This is called a pulse. The result of such act is that the sum magnetisation ($M_0$) is being tipped away from the z-axis, in a plane perpendicular to the direction of $B_1$, by rotation around the $B_1$ field axis. This is shown in Figure 1.4.

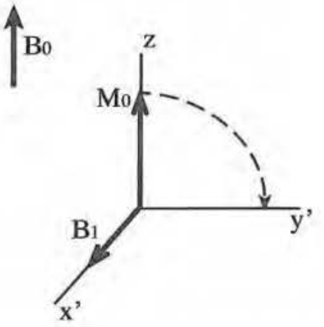

*Figure 1.4: The precession of the macroscopic magnetisation vector $M_0$ around $B_1$.*

However, due to the precession around $B_0$, the magnetisation $M_0$ will not be along the y-axis after the pulse but somewhere in the x, y plane. Since the initial y-component (y-axis = receiver-axis) determines the intensity of the signal, the lab frame is replaced by the so-called rotating frame x'y', that rotates with the Larmor frequency $\omega_L$. If the $B_1$ field is along the x' axis of the rotating frame, the effect of $B_1$ is to turn the vector $M_0$ around the x'-axis, i.e. into the y'z-plane (Figure 1.4). As a result, after a 90° pulse (see later) the sum magnetisation $M_0$ is tipped along the y' receiver-axis. Therefore, the diagram in Figure 1.4 is for convenience already drawn in the rotating frame. The result of using the rotating frame concept in the NMR theory is that it removes the time dependence of some quantities: in the rotating frame the $B_1$ field is static and no precession of the sum magnetisation $M_0$ around the $B_0$ field occurs.
The vector $M_0$ can be tilted over a different angle $\Theta$, the pulse angle.

$$\Theta = \gamma B_1 \tau_p \tag{1.7}$$

This angle increases with the amplitude of $B_1$ when applied during a fixed time period or depends on the length of time ($\tau_p$) of the pulse in a fixed $B_1$ field.

The pulse is called after the direction of $B_1$: if $B_1$ is along the x'-axis the pulse is called $90^\circ_{x'}$ or $180^\circ_{x'}$ depending on the pulse length; when the B1 field is along the y'-axis, the pulse is called $90^\circ_{y'}$ or $180^\circ_{y'}$ In Figure 1.5 the position of the magnetisation vector following a $90^\circ_{x'}$ and a $180^\circ_{x'}$ pulse is shown. From these vector diagrams it is seen that the transverse magnetisation $M_{y'}$ is greatest after a $90^\circ_{x'}$ pulse and is zero for a $180^\circ_{x'}$ pulse.

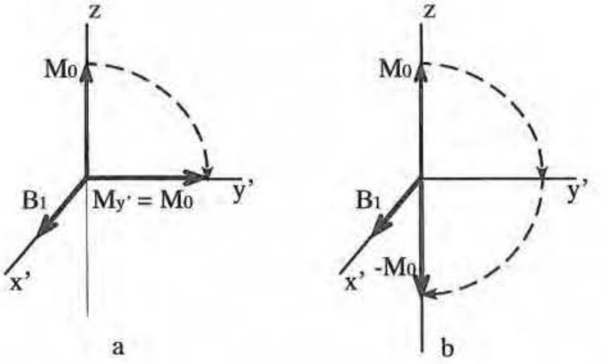

*Figure 1.5: Direction of the macroscopic magnetisation vector $M_0$ in the rotating co-ordinate system: a) after a $90^\circ_{x'}$ pulse b) after a $180^\circ_{x'}$ pulse.*

The signal detected in NMR is the current induced in the coil by the precessing magnetisation vector. The receiver coil is oriented along the y'-direction thus the signal is directly proportional to the magnetisation component $M_{y'}$. Immediately after such a $90^\circ_{x'}$ pulse the transverse magnetisation $M_{y'}$ is maximal and the spin relaxation starts in the x' y' plane by spin-spin or $T_2$ relaxation and in the z-direction by spin lattice or $T_1$ relaxation (see section 1.2). A few microseconds after the transmitter pulse (to prevent pulse break through in the receiver), during the detection period, the magnetisation component $M_{y'}$ is recorded, in the time domain. Due to x' y' precession and the $T_2$ relaxation process, the profile of the magnetisation component $M_{y'}$ will be that of an oscillating exponential decreasing function. This is called the free induction decay (FID). Due to the presence of several resonance frequencies and scalar spin-spin coupling, the FID is a complex composition of oscillations. This FID is converted into the frequency domain spectrum by a fast Fourier transformation.

For a deeper understanding and a quantum-mechanical description of the basic principles of NMR some general NMR texts are referred to.[6,7,8,9,10]

## 1.2 Relaxometry

Besides classical NMR spectroscopy, NMR relaxometry opens the possibility to gain information about the molecular mobility and molecular miscibility of the system. Moreover, relaxometry in magnetic resonance imaging (MRI) allows to determine image contrast by $T_1$ or $T_2$ weighting, comparable to the different colouring techniques used in histology. While NMR relaxometry in the liquid and the solid phase studies the molecular dynamics and/or miscibility as bulk properties, MRI results in localised information of the relaxation behaviour.

In this section some fundamentals of spectroscopic relaxometry in the liquid and the solid phase and relaxometry as used in MRI, will be explained.

### 1.2.1 The principles of relaxation

In NMR experiments, the magnetisation is perturbed from along the direction of the static field by a pulse. When the pulse is switched off, the spin system reverts to its equilibrium state by relaxation. This relaxation is induced by magnetic interactions of the excited atom with the environment. The relaxation processes can mostly be described on the basis of exponential functions and first order rate constants $k_i$. Time constants instead of rate constants will be used because the relaxation processes are studied as time dependent measurements. The most fundamental relaxation times are the spin-lattice ($T_1$) and the spin-spin ($T_2$) relaxation times. Another important relaxation time, used in this thesis, is the spin-lattice relaxation time in the rotating frame ($T_{1\rho}$).

#### 1.2.1.1 Spin-lattice relaxation

The $T_1$ time constant governs the return of the magnetisation along the z-axis ($M_z$) to its original value $M_0$ (Figure 1.6). The interactions of the $\mu$ vectors with the changing electromagnetic dipoles (due to movements of electrons, atoms and molecules) in the direct environment, result in a transfer of the excess energy of the spin system to its surroundings, called the lattice. This process is an exchange of spin energy with the thermal motions of the surroundings.

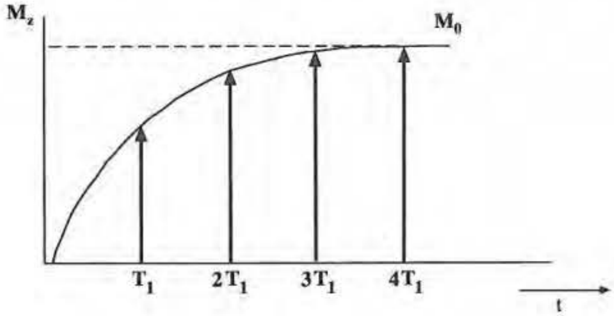

*Figure 1.6: The $T_1$ relaxation time determines the recovery of the magnetisation along the z-axis after a 90° pulse.*

Spin-lattice or longitudinal relaxation is generally a first-order process described by the following Bloch equation: [11]

$$\frac{dM_z}{dt} = \frac{-(M_z - M_0)}{T_1} \tag{1.8}$$

and the magnetisation recovery towards the equilibrium value $M_0$ is described by the following exponential equation:

$$M_z = M_0 \ (1 - e^{-t/T_1}) \tag{1.9}$$

To obtain quantitative results, a delay time of ± 5 times $T_1$ has to be respected between two successive pulses. The equilibrium magnetisation M0 is recovered to 99.3 % after a delay time of 5 times T1.

Most T1 relaxation time measurements are performed by means of the inversion recovery method (see section 3.4.3).

### 1.2.1.2 Spin-spin relaxation

Spin-spin relaxation is the process in which the net magnetisation along the y' axis (My') decays to zero. The spin-spin interactions induce a loss of the phase coherence of the μ vectors so that a random distribution of these vectors around the z-axis is obtained and the magnetisation in the x'y'-plane is divided (Figure 1.7).

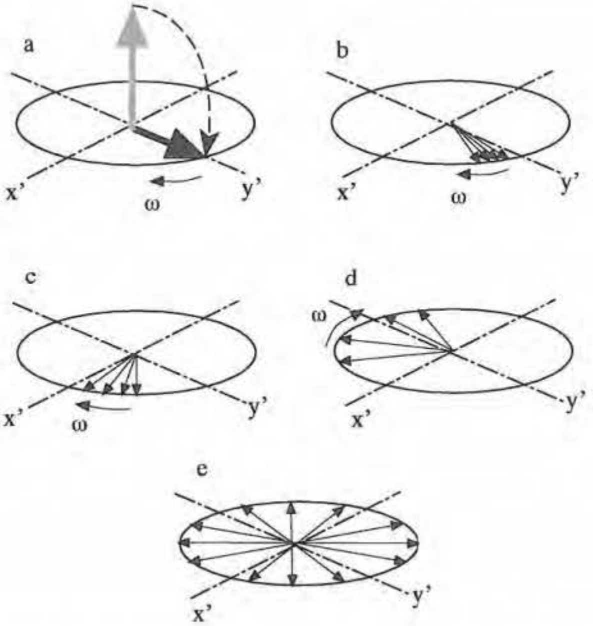

*Figure 1.7: (a) 90° pulse, (b-e) increasing dephasing of the μ vectors due to the spin-spin relaxation what is determined by the spin-spin relaxation time $T_2$.*

The transversal relaxation process is an energy conserving one, no overall change in the population of the energy levels occurs.

If it is assumed that the $T_2$-decay is, at least approximately, a first order process, the decay of the x'y'-magnetisation can be written by means of the Bloch equations:[11]

$$\frac{dM_{x'}}{dt} = -\frac{M_{x'}}{T_2} \tag{1.10}$$

$$\frac{dM_{y'}}{dt} = -\frac{M_{y'}}{T_2} \tag{1.11}$$

The transversal magnetisation process is described by the following exponential equation:

$$M_{y'} = M_0 \, e^{-t/T_2} \tag{1.12}$$

with $T_2$ the spin-spin relaxation time constant.

$T_2$ determines the line width of the signals in a frequency spectrum. The half-height width is then given by:

$$\Delta\nu_{1/2} = \frac{1}{\pi \ T_2^*} \tag{1.13}$$

$T_2$* is the spin-spin relaxation time in which the contribution of dephasing of the μ vectors caused by inhomogeneities of the static magnetic field, is incorporated. The intrinsic transversal relaxation time constant $T_2$ has to be determined by means of a spin-echo pulse sequence (see sections 2.4.2 and 4.6.2).

From previous definitions of $T_1$, $T_2$ and $T_2$* it can be concluded that $T_2^* < T_2 < T_1$ because the transversal $M_{y'}$ component decreases to zero by spin-spin interactions while the magnetisation along the z-axis (the equilibrium population) is not recovered completely.

### 1.2.1.3 Spin-lattice relaxation in the rotating frame

The $T_{1\rho}$ time constant prescribes the return of the z-component of spins in the spin-locked state.

If in a pulse sequence a classical $90^{\circ}_{x'}$ pulse, bringing $M_0$ along the y'-axis, is immediately followed by a 90° phase shift of the transmitter then we get a situation where the $B_1$ vector and the $M_0$ vector are both directed along the y' axis (Figure 1.8).

The magnetisation is kept in 'spin lock'. The spin-lock field is keeping $M_0$ along the y'-axis making relaxation more difficult due to competition between $B_1$ and $B_0$. The main field $B_0$ however, being much stronger than $B_1$, will re-establish the $M_0$ vector along the z-axis during a relaxation process governed by the spin-lock decay time $T_{1\rho}$, also called the *spin-lattice relaxation time in the rotating frame*. As for $T_1$, $T_{1\rho}$ relaxation is also governed by molecular motions in the surrounding. Molecular motions stimulate this relaxation most efficiently when their frequencies match the frequencies dictated by the strength of the spin lock field ($\omega_1 = \gamma_i B_1$) which is in the order of tens of kHz. This causes $T_1$ and $T_{1\rho}$ to be influenced by different molecular motions.

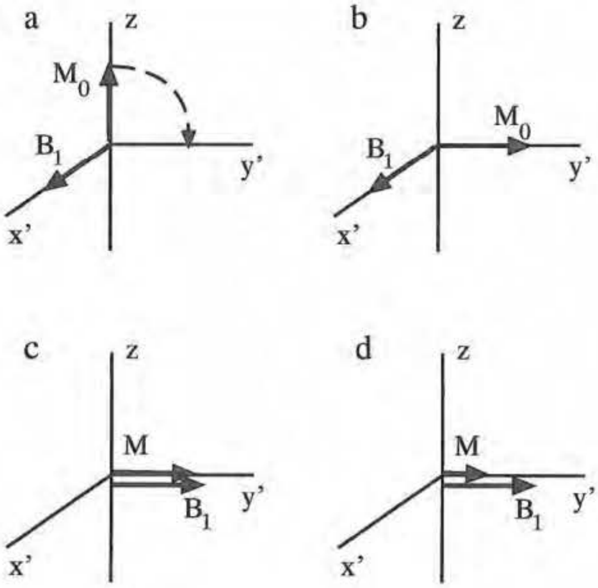

*Figure 1.8: (a) 90° pulse, (b) 90° phase shift of the $B_1$ vector, (c-d) magnetisation kept in 'spin lock'.*

The decrease of the magnetisation in spin lock as a function of the variable spin lock time t can be described by the following exponential equation:

$$M_z = M_0 \, e^{-t/T_{1\rho}} \tag{1.14}$$

The pulse sequence to determine the $T_{1\rho H}$ decay time is described in section 3.4.3.

### 1.2.1.4 Relaxation times as a function of the correlation times and the magnetic field strength

The relaxation times are influenced by molecular motions, as mentioned before, internuclear distances and the magnetic field. One of the most important relaxation mechanisms for nuclei with a nuclear spin quantum number I = $^1/_2$ is the dipole-dipole interaction. The local magnetic field, $B_l$, felt by a nuclei I as a result of the magnetic moment $\mu_S$ of nuclei S nearby, can be expressed with the following equation:

$$B_l = \mu_S \frac{1}{r_{I,S}^3}\left(3\cos^2\theta_{I,S} - 1\right) \tag{1.15}$$

hereby is $r_{I,S}$ the internuclear distance and $\theta_{I,S}$ the angle between the internuclear vector and the main magnetic field $B_0$. Molecular motions cause modulations of $\theta_{I,S}$ so that relaxation can occur. The relaxation time constants are strongly dependent on the way that dipole-dipole interactions are varied by molecular motions, which are characterised by a correlation time $\tau_c$. The correlation time of a molecule is corresponding roughly to the interval between two successive reorientations or positional changes of the molecule (by vibration, rotation, or translation). These random motions are spread over a broad frequency region.

The dependence of the relaxation time constants on the dipolar relaxation is expressed in the equations developed by Bloembergen, Purcell and Pound.[12] They give the dipolar relaxation rates for two equal spins at a distance r, with an isotropic rotational motion, characterised by the correlation time $\tau_c$, as follows:

$$\frac{1}{T_1} = \frac{3}{10}\frac{\gamma^4\hbar^2}{r^6}\left[J(\omega_L) + 4J(2\omega_L)\right] \tag{1.16}$$

$$\frac{1}{T_2} = \frac{3}{20}\frac{\gamma^4\hbar^2}{r^6}\left[3J(0) + 5J(\omega_L) + 2J(2\omega_L)\right] \tag{1.17}$$

$$\frac{1}{T_{1\rho}} = \frac{3}{10}\frac{\gamma^4\hbar^2}{r^6}\left[\frac{5}{2}J(\omega_L) + J(2\omega_L) + \frac{3}{2}J(\omega_1)\right] \tag{1.18}$$

In these equations $J(\omega)$ is the spectral density which describes the probability available at angular frequency $\omega$ from the fluctuating interaction, as expressed in equation 1.19:

$$J(\omega) = \frac{2\tau_c}{1+\omega^2\tau_c^2} \tag{1.19}$$

The correlation time $\tau_c$ and consequently $T_1$, $T_{1\rho}$, and $T_2$ are depending on the viscosity, temperature, aggregation and the molecular weight.

From these equations it is known that molecular motions at the Larmor frequency ($J(\omega_L)$) or twice the Larmor frequency ($J(2\omega_L)$), motions in the MHz region, influence the three relaxation times, the longitudinal relaxation time in both the laboratory and the rotating frame, as well as the transverse relaxation time. The static term $J(0)$ on the other hand only contributes to spin-spin relaxation. It is this static term that describes the spin-spin interactions which causes the fanning out of the transverse magnetisation $M_{y'}$, without having an effect on the longitudinal magnetisation $M_z$. The longitudinal relaxation time in the rotating frame, $T_{1\rho}$, has also an additional term $J(\omega_1)$. This term is depending on modulations with frequencies depending on the $B_1$ field, therefore situated in the kHz region.

The spectral density $J(\omega)$ is a function of the frequency $\omega$ as is shown in Figure 1.9. The area under the curves is always constant. In Figure 1.10 the dependence of the relaxation times $T_1$, $T_{1\rho}$, and $T_2$ on the correlation time $\tau_c$ is presented. From the Figures 1.9 and 1.10; and from equations 1.16 to 1.19 three distinct regions can be evaluated:

1) The region for short $\tau_c$ times or if $\omega_L^2\,\tau_c^2 << 1$. This region is characteristic to mobile molecules in the solution state for which the molecular motions are spread over a wide frequency region as shown in Figure 1.9a. $J(\omega)$ is small for every value of $\omega$ and therefore all frequencies have small probability and relaxation processes are not efficient. This region is known as the *extreme narrowing region*. In Figure 1.10 one can see that $T_1$, $T_{1\rho}$ and $T_2$ are equal and change linear as a function of the correlation time. This implies that the spin relaxation decay times decrease as $\tau_c$ increases, thus as the mobility decreases.

However, if $\tau_c$ increases sufficiently so that it becomes on the order of $\omega_L^{-1}$, a new region is entered.

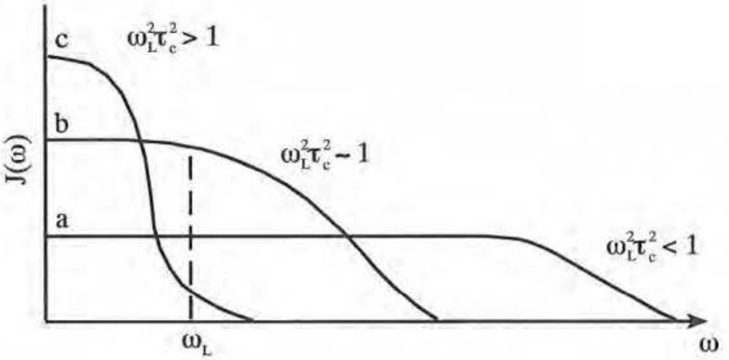

*Figure 1.9: Plot of the spectral density J(ω) as a function of the frequency ω for (a) the extreme narrowing region, as for small, mobile molecules, (b) moderate mobility and (c) for rigid molecules. $\omega_L$ is the Larmor frequency.*

2) If $\omega_1^2\ \tau_c^2 \approx 1$ the spectral density J(ω) is high at or near the Larmor frequency (Figure 1.9b). In this region the $T_1$ relaxation is most efficient and has its minimum. The $T_1$ minimum occurs when the sudden drop in J(ω) as a function of ω (see Figure 1.9) corresponds to the resonance frequency, i.e. when $\tau_c = \omega_L^{-1}$. For long $\tau_c$ times a third region is observed.

3) If $\omega_L^2\ \tau_c^2 >> 1$ most of the molecular motions have a low frequency and high frequency motions are absent (Figure 1.9c). This situation is typical for immobile molecules like polymers in the solid state. The spectral densities $J(\omega_L)$ and $J(2\omega_L)$ are small and the $T_1$ decay, which is influenced by motions near the Larmor frequency, are less efficient. In this case $J(\omega_L)$ and $J(2\omega_L)$ contributions to the $T_2$ relaxation are negligible as compared to the static term J(0) and the spin-spin relaxation is determined quasi only by static dipolar interactions. In the region in between, the $T_{1\rho}$ minimum is found when $\tau_c = \omega_1^{-1}$ with $\omega_1 = \gamma B_1$.

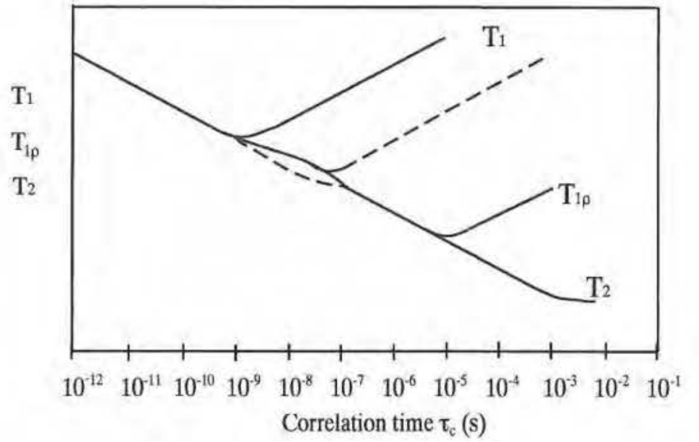

*Figure 1.10: The dependence of* $T_1$, $T_{1\rho}$ *and* $T_2$ *on the correlation time* $\tau_c$ *and for* $T_1$ *on the magnetic field strength (—400 MHz, --- 20 MHz).*

The dependence of the relaxation decay times on the dipolar relaxation as expressed in equations 1.16 to 1.18 holds for the dipolar relaxation rate for two equal spins with isotropic rotational motion. For dipolar interactions between different spins and/or anisotropic motions, these equations are extended with additional terms implying more correlation times.[9]

### 1.2.2 Spectroscopic relaxometry in the liquid and the solid state

The molecular dynamics and the degree of miscibility of polymer systems can be studied by relaxometry in the liquid as well as in the solid state. Both techniques examine the properties of the materials in the bulk. Each isotope or molecular environment has its own $T_1$, $T_{1\rho}$ and $T_2$.

For liquids high frequency Brownian motions average out the dipolar couplings. For rigid polymers below $T_g$, different sets of nuclei can be coupled by dipolar interactions and as a consequence, their relaxation times can be averaged out.[13] For plastics above $T_g$, the dipolar couplings become strongly reduced by molecular motions but not averaged out as in the liquid state.

### 1.2.2.1 Spin diffusion

For isotopically abundant, non-isolated nuclei (e.g. $H^1$) in solids, the $T_{1H}$ and $T_{1\rho H}$ relaxation times of protons in different environments often are averaged out by spin diffusion.[10,14]

Spin diffusion is not a process of molecular diffusion but is the transport of spin energy within the spin system by mutual, energy-conserving spin flips. Like in every other diffusion process there is a gradient at the basis, in this case a magnetisation gradient. This can be expressed as in the next equation:

$$\frac{\partial M(q,t)}{\partial t} = D\frac{\partial^2 M(q,t)}{\partial r^2} \qquad (1.16)$$

where M(q,t) describes the magnetisation on a position q at a time t, D is the spin diffusion coefficient, depending on the jump frequency and the distance between the neighbouring nuclei. The magnetisation gradient comes about because some areas in a solid show a more efficient relaxation than others.

Due to spin diffusion all abundant nuclei of the same type within the solid phase can show the same, averaged $T_{1H}$ and $T_{1\rho H}$ decay time. In this way, the relaxation times become volume properties and so it is possible to detect the existence of distinct domains and to measure the domain sizes in heterogeneous systems (polymer blends and networks, semi-crystalline polymers).[15] The maximum pathway L over which spin diffusion can take place depends on the relaxation time t as expressed in the following equation:

$$L = \sqrt{6\,Dt} \qquad (1.17)$$

with t being the relaxation time $T_{1H}$ or $T_{1\rho H}$. $T_{1H}$ is on the order of seconds and consequently the pathway is larger than 10 nm. $T_{1\rho H}$ is on the order of milliseconds and thus a shorter pathway L of 1 to 10 nm is obtained. Since the $T_2$ relaxation of rigid molecules is very fast (microseconds), it is not averaged out by spin diffusion and remains a local property.

### 1.2.2.2 Most important relaxation times

The most important relaxation times in order to study the molecular dynamics and the molecular miscibility in polymer systems are $T_{1H}$, $T_{1\rho H}$ and $T_{2H}$. These relaxation parameters are used in the experimental part of this thesis and the utility of them is considered below. The parameters $T_{1C}$, $T_{1\rho C}$ and $T_{2C}$ are used in a less extent because of the low abundance of the $^{13}C$ isotope and the duration of the experiments (repetition times of 5 times the longest $T_{1C}$).[16,17]

In solid state NMR $T_{1H}$, $T_{1\rho H}$ and $T_{2H}$ are the relaxation times measured after a polarisation transfer from $^1H$ to $^{13}C$ is undertaken. The $^1H$ magnetisation is detected indirectly via the $^{13}C$ NMR signal. Consequently, the high selectivity of the cross polarisation/magic angle spinning[10] (CP/MAS) $^{13}C$ NMR experiment is combined with the volume properties in the case of $T_{1H}$, $T_{1\rho H}$.

*The utility of the proton spin-lattice relaxation time, $T_{1H}$*

The proton spin-lattice relaxation time is dominated by molecular motions in the MHz region. In liquids $T_{1H}$ is determined by molecular dynamics while for solids below the glass transition temperature ($T_g$) not only molecular dynamics but also spin diffusion determines the $T_{1H}$ decay. In the solid state at temperature below $T_g$, $T_{1H}$ is dominated by mobile end group and side chain processes, while above $T_g$ the relaxation via backbone motions also becomes important.

Below $T_g$ $T_{1H}$ is a material phase property for solids because spin diffusion is very efficient for the high abundant $^1H$ protons which have a high gyromagnetic ratio. This means that all the protons in the region over which spin diffusion takes place (typically 10-100nm) have the same $T_{1H}$ relaxation time, conversely to the liquid state where $T_{1H}$ times are usually different for chemical distinct protons. Generally, the spin-lattice relaxation is a rather slow process causing the relaxation to be averaged out over large domains. Often only one $T_{1H}$ relaxation time is found for a polymer or a thermoset, although there are different regions (at the cross-links, between the cross-links, end groups). The protons of the network relax through the protons of the mobile end groups due to spin diffusion.

*The utility of the proton spin-lattice relaxation time in the rotating frame, $T_{1\rho H}$*

$T_{1\rho H}$ is an important relaxation time parameter to investigate polymers since this relaxation time is affected by motions in the kHz region. The proton $T_{1\rho H}$ relaxation time is a volume property averaged over a shorter distance than $T_{1H}$ (typically 1-2 nm) by spin diffusion. In solids below $T_g$ strong dipolar couplings between protons are the cause of efficient spin diffusion. Therefore, it is possible to measure the homogeneity of mixing in a blend or a copolymer because the rate of spin diffusion is strongly influenced by the spatial mixing of the polymer chains. $T_{1\rho H}$ (ms) is mostly shorter than $T_{1H}$ (s) which means that the relaxation is averaged out over smaller regions. This can result in several $T_{1\rho H}$ components, while for $T_{1H}$ there is often only one relaxation time observed.

*The utility of the proton spin-spin relaxation time, $T_{2H}$*

Compared to $T_{1H}$ and $T_{1\rho H}$, the spin-spin relaxation time $T_{2H}$ is easier to interpret because a longer $T_{2H}$ relaxation time always indicates a higher mobility (Figure 1.10). With $T_{2H}$, the local molecular mobility can be studied because during the rather short $T_{2H}$ relaxation time (tens of microseconds for solids), spin diffusion does not have the time to average out the relaxation over the domains. Moreover, the value of $T_{2H}$ is much less dependent on the strength of the static magnetic field $B_0$ or spin lock field $B_1$ than is the case for $T_{1H}$ and $T_{1\rho H}$. For rigid systems the spin-spin relaxation is mainly determined by slow, almost static molecular motions of 100-1000 Hz, reflected by the contribution J(0).

### 1.2.3 Relaxometry as applied in NMR imaging[18,19,20]

The success of NMR as an imaging technique derives from the availability of contrast features in a non-invasive and non-destructive way. MRI is not restricted to surfaces but allows to 'look' at the inside properties of materials. The image contrast can be used for many purposes and gives localised information on the micrometer scale while localised relaxometry can be used to obtain spatially dependent information of the chain dynamics and miscibility of polymer materials on the nanometer scale.

To obtain images with an acceptable spatial resolution, the spectral line width of the resonance to image (e.g. water protons) has to be smaller or small enough as compared to the width of a pixel element expressed in Hertz caused by the applied magnetic field gradient. The field gradient is applied in order to induce spatial variation in the resonance frequency of the resonance that will be imaged in order to obtain a two-dimensional image. For liquids the line width is narrowed by fast molecular motions to several tens of Hertz or less and so liquids (and ingressed solvents) can be imaged easily by means of a simple spin-echo pulse sequence (see section 4.6.2). For solids the molecular motions are slowed down, resulting in much broader line widths and consequently a low spatial resolution will be obtained. Moreover, the signal will be relaxed by the $T_2$ relaxation before the 180° spin-echo refocusing pulse will be applied. To image rigid polymeric materials single-point imaging is required.[21,22] Elastomers exhibit properties that are in between those for liquids and solids. They are still suitable materials for investigations by NMR imaging.

*Image contrast*

NMR imaging is an excellent technique because one can choose the physical parameter which will be employed. Mobile proton density (spin density $M_0$), spin-lattice relaxation or spin-spin relaxation weighting can be applied in the NMR image. Usually all three parameters will be involved to a greater or a lesser extent depending on the operating conditions and the NMR technique used. Thus regions of a specimen which contain an equal density of mobile protons may well have different image intensities through relaxation time differences.

Most imaging experiments are based on a Hahn spin-echo which causes a refocusing of the magnetisation.[23,24] The echo time (TE) is the time between excitation and the echo signal formation (see section 4.6.2). The intensity of the observed echo signal is determined by the proton spin density and by the $T_2$ relaxation during the echo time TE. The repetition time (TR) of the pulse sequence is prescribed by the recovery of z-magnetisation and is determined by the $T_1$ relaxation time.

A spin density weighted image is obtained with a short TE and a long TR (TR = 5 times $T_1$) to permit complete recovery of magnetisation.

A $T_1$ filter selects the rapidly recovering magnetisation components from the slow recovering ones by partial saturation or inversion recovery. Reduction of the repetition time between successive scans in the MRI experiment leads to partial saturation of the magnetisation with long $T_1$ times and suppression of the corresponding signals in the image. Consequently, in a $T_1$ weighted image bright or high-intensity areas correspond to sites with a relatively short $T_1$ value that has recovered considerably magnetisation during TR as compared to the dark (low intensity) areas that have not. Because the $T_1$ relaxation time is determined by molecular motion having frequencies in the order of the Larmor frequency,[25] image contrast is generated by segmental mobility at a time scale between $10^{-8}$ and $10^{-12}$ seconds. The $T_1$ filter is a filter for long correlation times.

Another well-known filter is the $T_2$ filter. An increase of TE leads to $T_2$ weighted images. Here the magnetisation components with a $T_2 << TE$ are suppressed in the image. Image areas in which the $T_2$'s are long will appear relatively bright at longer echo times whereas areas in which the $T_2$'s are short will have a reduced intensity and hence appear darker. Since $T_2$ is very sensitive to slow molecular motions, the $T_2$ filter is a filter for rigid protons having a $T_2 < 500$ microseconds.

## 1.3 Scope of the thesis

A general introduction into the basic principles of NMR spectroscopy is represented in Chapter 1, followed by a description of relaxometry.

In Chapter 2, NMR relaxometry is utilised in the liquid state to examine the gelation mechanism of syndiotactic poly(methyl methacrylate) (sPMMA). By means of a spin-spin relaxation time study, components with a different molecular mobility and their accompanying fractions reveals a better understanding of the two step gelation mechanism of sPMMA in toluene.

The phase morphology of segmented polymer networks and the corresponding polymer blends is examined in detail by $^{13}C$ NMR relaxometry in the solid state in Chapter 3. The segmented polymer networks are nano-structured amphiphilic networks based on poly(1,3-dioxalane) (PDXL) and poly(methyl methacrylate) (PMMA) with varying PDXL/PMMA ratio. Small domain sizes are observed in all networks while for the blends the phase morphology strongly depends on the PDXL weight fraction.

Chapter 4 contains three main sections in which different toughened materials are studied under load by MRI relaxometry. The materials are measured under load in the magnet. The first section describes the material response of acrylonitrile-butadiene-styrene (ABS) upon mechanical stress. Discrete damage bands in the damage zone are visualised in detail. Localised analysis of the spin density ($M_0$), the spin-lattice ($T_1$) and the spin-spin ($T_2$) relaxation time in these damage bands, reveals spatial dependent information about the molecular chain dynamics and cavitation as well under load as after unloading,.

In the second section, a block copolymer of poly(butadiene terephthalate) (PBT) and poly(tetramethylene oxide) (PTMO) is investigated under load. Localised analysis of the $T_2$ decay time shows a spatial dependent change in the chain mobility induced by the applied stress.

Two types of polyamide 6 (PA6) specimen are investigated in section 3 of Chapter 4. One type contains pure maleic anhydride grafted ethylene-propylene (EPM-*g*-MA), dispersed in the PA6 matrix while the other type contains PA6 occlusions in the dispersed rubbery phase. Both types are examined under load and show remarkable differences in the behaviour of the molecular chain dynamics.

A short summary, general conclusions and perspectives are given in Chapter 5, in English and Dutch respectively.

## 1.4 References

---

1. Bloch, F.; Hansen, W.W.; Packard, M. *Phys. Rev.* **1946**, 69, 127.
2. Purcell, E.M.; Torrey, H.C.; Pound, R.V. *Phys. Rev.* **1946**, 69, 37.
3 Apple, T.M.; *Applied spectroscopy* **1995**, 49, 12A.
4 Smith, M.E.; Strange, J.H. *Meas. Sci. Technol.* **1996**, 7, 449.
5 Koenig, J.L. *Macromol. Symp.* **1994**, 86, 283.
6 Harris, R.K.; "Nuclear Magnetic Resonance Microscopy, A physicochemical View", Pitman publishing Inc., London, 1983.
7 Bovey, F.A.: "Nuclear Magnetic Resonance Spectroscopy"; Academic Press: London, 1988.
8 Friebolin, H.: "Basic One- and Two-Dimensional NMR Spectroscopy"; VCH: Weinheim, 1991.
9 van de Ven, F.J.M.; "Multidimensional NMR in Liquids, Basic Principles and Experimental methods", VCH Publishers, Inc., New York, 1995.
10 Komoroski, R.A.; "High resolution NMR spectroscopy of Synthetic Polymers in Bulk"; VCH: Florida, 1986.
11 Bloch, F. *Phys. Rev.* **1946**, 70, 460.
12 Bloembergen, N.; Purcell, E.M.; Pound, R.V. *Phys. Rev.* **1948**, 73, 679.
13 Fyfe, C.A.: "Solid State NMR for Chemists"; CFE Press: Ontaria, Canada, 1984.
14 McBierty, V.J.; Douglass, D.C. *J. Polym. Sci., Macromol. Rev.* **1981**, 16, 295.
15 Wang, J. *J. Chem. Phys.* **1996**, 104, 4850.
16 Voelkel, R. *Angew.Chem. Int. Ed. Engl.* **1988**, 27, 1468.
17 Laupretre, F. *Prog. Polym. Sci* **1990**, 15, 425.
18 Blümler, P.; Blümich, B. *Rubber Chemistry and Technology* **1997**, 70, 468.
19 Callaghan, P.T. *"Principles of Nuclear Magnetic Resonance Microscopy"*, Clarendon Press, Oxford, 1991.
20 Morris, P.G. *"Nuclear Magnetic Resonance Imaging in Medicine and Biology"*, Clarendon Press, Oxford, 1990.

21 Beyea, S.D.; Balcom, B.J.; Prado, P.J.; Cross, A.R.; Kennedy, C.B.; Armstrong, R.L.; Bremner, T.W. *J. Magn. Reson.* **1998**, 135, 156.

22 Kennedy, C.B.; Balcom, B.J.; Mastikhin, I.V. *Canadian Journal of Chemistry* **1998**, 76, 1753.

23 Hahn, E.L. *Physical Review* **1950**, 80, 580.

24 Hennig, J. *Concepts in Magnetic Resonance* **1991**, 3, 125.

25 Blümler, P.; Blümich, B. *Magn. Reson. Imaging* **1992**, 10, 779.

# 2

# NMR relaxometry in the liquid state: Study of the gelation of sPMMA in toluene

This chapter discusses a liquid $^1$H NMR study concerning the gelation mechanism of sPMMA in toluene. The NMR study is performed within the scope of an 'Inter University Attraction Pole' (IUAP) collaboration. The synthesis and the preparation of solutions and gels of PMMA in toluene have been done at the Laboratory for Polymer Research of Prof. Berghmans at the University of Leuven. Gels of PMMA in toluene are extensively studied by means of rheology and FTIR experiments by Prof. Berghmans et al.[1] A combination of the results of the NMR study with the information obtained from rheology and FTIR analysis has led to the unambiguous correlation between a co-operative conformational transition and gelation of sPMMA in toluene.[2]

## 2.1 Introduction

A polymeric network that contains solvent, is usually called a polymeric gel. During reaction, polymers may be cross-linked to several distinguishable levels. At the lowest level, branched polymers are formed. At this stage, the polymers remain soluble, sometimes known as the sol stage. As cross-links are added, clusters are formed, and the cluster size increases. Eventually, the structure becomes infinite in size: that is, the composition gels. Gelation may be conceived as the point where a three dimensional network is formed and where the solvent is dissolved in the polymer. From a physico-chemical point of view, the viscosity of the reacting mass goes to infinity at the gelation point. In spite of the existence of a continuous liquid phase, no flow appears. The polymers go from being a liquid to being a solid.

There are several types of polymeric gels. They may be categorised into two major classes, according to the type of cross-links: gels may be prepared using either chemical or physical cross-links.

The chemical cross-linked or permanent gels consist of solvent-logged covalently bonded polymer networks. One family of such networks is formed by cross-linking pre-existing polymer chains, as in the process of vulcanisation. Another family makes use of simultaneous polymerisation and cross-linking (multifunctional monomers).

Thermoreversible gels generally belong to the physical cross-linked gels. These thermoreversible gels undergo a transition from a solid-like form to a liquid-like form at a certain characteristic temperature. The links between the polymeric chains are transient in nature and support a stable polymeric network only below a characteristic "melting" point; the physical bonds break at elevated temperature and reform at lower temperatures. Physical cross-links in gels may involve dipole-dipole interactions, traces of crystallinity, multiple helices, and so on and thus vary greatly with the number and strength of the bonds. The number of physical cross-links depends on time, pressure and temperature.[3] In this chapter the gelation mechanism of syndiotactic poly(methyl methacrylate), a thermoreversible gel is studied. Therefore only a more detailed view on the gelation mechanisms of thermoreversible gels, will be discussed.

### 2.1.1 Gelation mechanisms

Depending on the type of physical cross-links that will be formed between the polymer chains a more pronounced differentiation of the gelation mechanisms can be made.

Gelation by crystallisation occurs when intermolecular crystals, existing of different polymer chains form the cross-links.[4] The crystals originating from dilute solutions are lamellar plates whereas the lamellar crystals arising from concentrate solutions are parts of spherical supramolecular structures (spherulites). A typical example of this kind of gelation appears from polyethylene solutions.[5]

A liquid-liquid phase separation can precede the crystallisation. A phase separation into a polymer rich and a polymer poor solution occurs by cooling down the polymer solution. Further cooling results in the crystallisation of the polymer rich phase. If the polymer rich phase forms a continuous phase, a network will be formed. This mechanism has been detected e.g. in solutions of polyethylene and poly(vinyl alcohol).[6,7,8]

Non-crystallisable polymers can form gels by liquid-liquid phase separation and glazing if the glass-transition temperature ($T_g$) is situated in the same temperature region. This kind of gelation takes place in solutions of atactic polystyrene in decahydronaftalene and atactic poly(methyl methacrylate) in aliphatic alcohols.[9,10]

Another important gelation mechanism for physical cross-linking is the conformational gelation. The first step in this type of gelation is a change of the conformation of the polymer chains to form ordered structures. In solutions with stereo-regular polymers a coil-to-helix transition will be introduced upon cooling, followed by the association of helices into larger multichain association units. These units form the physical cross-links of the polymer gel. A well-known example of this mechanism is found for biopolymers. Two different models have been proposed for the structures formed by cooling. The model of Rees et al. described the formation of a double helix in the first step, followed by the association of these double helices in a second step.[11] In the other model, introduced by Smidsrød, a transition to a single-helix, stabilised by intramolecular H-bonds, is proposed in the first step followed by the association of these helices to form the gel. In this kind of mechanism, the solvent and the ionic interactions become of interest. Besides the biopolymers also synthetic polymers can form gels following this mechanism, such as iso- and syndiotactic polystyrene and syndiotactic poly(methyl methacrylate).[12,13,14,15] For the latter polymer, a mechanism of gelation has already been proposed by Berghmans et al.[16,17] and will be further clarified in this chapter.

*Detection of the gel point.*

The viscoelastic properties of the polymer-solvent system change dramatically during the gelation process. The viscosity increases as a function of time until an infinite value is reached; this is by definition at the gel point. The storage modulus G' and the loss modulus G'', measured as a function of frequency, are important parameters to study the evolution of gel formation. Initially the system acts as a liquid and so the slope of log G' as a function of log $\omega$ is equal to 2. After some time the network will be formed gradually. The increase of G' can be on the order of $10^4$. Just behind the gel point, a rubbery plateau should be obtained. This can only be detected if the viscoelastic properties can be measured at very low frequencies, which is technically impossible for most of the instruments. The most important methods to detect the gel point are the detection of the mechanical properties (G' and G'') and the method of Winter and Chambon.[18,19] and the falling boll method. In the latter, a steel or glass boll sinks down because of its weight trough the test sample, which has been filled into the fall tube. The sinking time of the ball is measured. The kinematic viscosity is calculated from this.[20]

## 2.1.2 Gelation of syndiotactic poly(methyl methacrylate)

Syndiotactic poly(methyl methacrylate) (sPMMA) forms thermoreversible gels in polar as well as in apolar solvents because of its ability to form ordered structures. The final structure depends strongly on the degree of stereoregularity of the PMMA and on the type of solvent. Interaction of long stereoregular sequences leads to association of the sPMMA in solution. Consequently a minimal length of syndiotactic sequences is required to obtain associates in the solution. This minimal length is depending on the solvent e.g. 7-8 monomer units are necessary to form associates of sPMMA in toluene.[21] In o-xylene and toluene a transparent gel will be formed[21,22] while this in acetone or butylacetate is rather opaque.[23,24] In chloroform ($CHCl_3$), a better solvent, no association will be found.

The mechanism of the thermoreversible gelation of sPMMA has been studied extensively using a wide variety of experimental techniques.

Association of the polymer chains in solution can be conveniently studied by $^1H$ NMR. Molecular mobility in monomer units, which are part of ordered associated structures, is usually hindered so that these protons escape often detection in the liquid NMR spectra. Consequently the observed spectrum of such systems corresponds to non-associated monomer units.[16,21,22,23,25,26]

The effects of temperature and equilibration time on the molecular mobility in polymer solutions appear as a change in the $^1H$ resonance line width.[17] The influence of the solvent on structure formation can be obtained out of $^{13}C$ CP/MAS spectra. The existence of a double helix in solid samples of sPMMA gels in toluene, after evaporating the solvent, was demonstrated.[27]

By means of $T_1$ relaxometry the stereo-regularity and the influence of the solvent on the molecular mobility was examined.[28,29] The $T_1$ relaxation time differs strongly depending on the stereoregularity.[28] The temperature dependence of the $T_1$ value of the carbon resonances of sPMMA in $CDCl_3$ and $C_6D_6$ was examined by Inoue et al.[29] In $CDCl_3$ a linear increase of $T_1$ with increasing temperature for all three protonated carbon atoms of the monomer unit was observed while in deuterated benzene ($C_6D_6$) this was only found for the methylene carbon atom. For the side groups, from 55 °C an increased slope was obtained due to increased activation energy for rotation caused by the steric hindrance of large side-chain groups. The existence of a polymer-solvent complex in gels of sPMMA in bromobenzene has been shown by means of the spin-lattice relaxation experiments.[30]

Infrared observations clearly demonstrate the formation of sequences with regular conformation.[31,32,33] The appearance of a second absorption at a higher frequency in the carbonyl stretching region is characteristic for intermolecular interactions.[31,33,34] The transition from a predominantly trans-gauche (TG) to a trans-trans (TT) conformation is revealed by an increase of the intensity of the —$CH_2$— rocking vibration at 860 $cm^{-1}$ at the expense of the intensity of the peak at 843 $cm^{-1}$. This molecular order is maintained after removal of the solvent.[12,17,32,33,34]

By means of wide-angle X-ray scattering (WAXS) a unit cell and conformation has been determined.[32,35,36,37] Aggregation of sPMMA in solution was also proved by osmometry, viscometry and light scattering.[21,23,]

### 2.1.3 Conclusion

Based on a literature study, it can be concluded that the structure formation of sPMMA is a complicate problem depending on the stereo-regularity of the polymer, the type of solvent, temperature and the concentration.

Spevacek et al. suggested a model of aggregation of sPMMA in n-butyl acetate with three distinguishable processes: 'globulation', nucleation and flocculation.[24] In toluene an intramolecular change of the conformation from a coil-to-single helix was recognised. Simultaneously close contact of the ester groups of two interacting s-sequences leads to the formation of a double helix.[34]

This model bears resemblance to the gelation mechanism of gelatine and some saccharides.[38]

Berghmans et al. determined a mechanism of gelation of sPMMA in o-xylene and toluene different from the model described above.[12,16,17] The combination of infrared and calorimetric data with rheological observations demonstrated clearly the occurrence of a two step gelation mechanism. The first step of the gelation is a coil-to-single helix transition, followed by the association of helices into larger multichain association units. The coil-to-helix transition is a true equilibrium process that can be detected separately through kinetic trapping.[17] The conformational transition is largely affected by a complicated interplay of polymer-polymer and polymer-solvent interactions.

The purpose of this chapter is to assess the fundamental role played by the conformational transition in the gelation process. The conformational transitions are studied by $^1$H NMR spin-spin ($T_2$) relaxation time experiments. Conformational changes in polymer chains are strongly correlated with appreciable changes in the mobility of the chain backbone and the chain side groups. This will lead to important changes in the $T_2$ relaxation times. The technique is very selective so that the behaviour of the different groups in the polymer chains can be studied separately.

Information obtained from $T_2$ relaxation measurements is combined with that derived from rheology and FTIR analysis which are performed at the laboratory of Prof. Berghmans.[2]

## 2.2 Aggregation of sPMMA in toluene

The conformational coil-to-helix transition is studied by NMR via line width analysis and spin-spin relaxation time measurements in order to get a more quantitative insight into the proposed two step gelation mechanism of sPMMA in toluene. By means of the $T_2$ relaxation time measurements, populations with different molecular mobility and their matching fraction can be detected. The fraction of sPMMA incorporated in helix structures will thus be quantified. An aPMMA solution in toluene serves as a reference system since no thermoreversible gelation, caused by helix structure formation, occurs for aPMMA due to the low degree of stereoregularity.

To measure under equilibrium conditions, the successive $T_2$ experiments were accomplished as a function of increasing temperature (to avoid hysteresis that occurs upon cooling)[17] and were initiated only after a thermal stabilisation period of at least 20 min.

### 2.2.1 $^1$H NMR spectra of aPMMA and sPMMA

Figure 2.1 shows the $^1$H NMR spectra of aPMMA at ambient temperature and aPMMA and sPMMA at 70 °C in toluene-$d_8$. The methoxy group appears at ± 3.3 ppm, the methylene proton region is situated around 2 ppm and the $\alpha$-methyl protons resonate in the region around 1 ppm. Increasing the temperature results in faster molecular motion and so a reduced line width.

The tacticity of both polymers used in this study was derived from $^{13}$C NMR spectra in $CDCl_3$ on the basis of the intensities of the $\alpha$-methyl triads.[39] For sPMMA and aPMMA, a ratio of 88/12/0 (rr/mr/mm) and 58/37/5 was found, respectively.

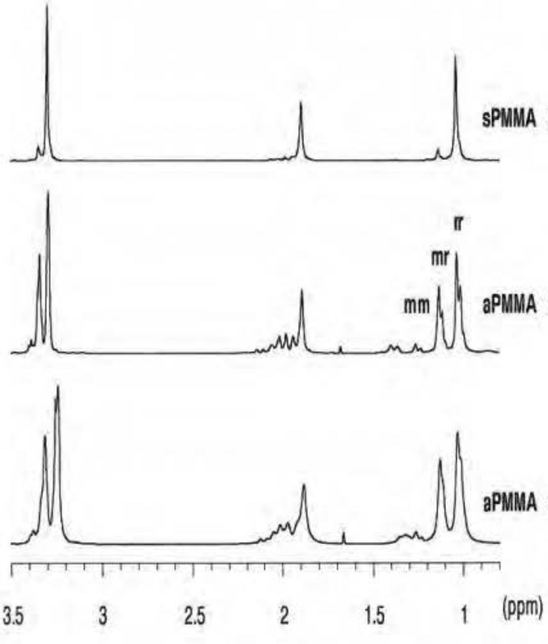

*Figure 2.1: $^1$H-NMR spectra of aPMMA at ambient temperature and aPMMA and sPMMA at 70 °C in toluene-$d_8$.*

### 2.2.2 $^1$H NMR line width experiments

The influence of temperature on molecular mobility can be studied through the evolution of the $^1$H spectral line width ($\Delta\nu_{1/2}$) at half height. The line width is directly related to the spin-spin relaxation time $T_2$*:

$$\Delta\nu_{1/2} \approx (\pi\, T_2^*)^{-1} \tag{2.1}$$

The $^1$H NMR line width ($\Delta\nu_{1/2}$) of the main resonance of the three different proton groups, was measured as a function of increasing temperature, for solutions of aPMMA and sPMMA in toluene-$d_8$ with a polymer weight fraction ($w_2$) of 0.10. The results are represented in Figure 2.2.

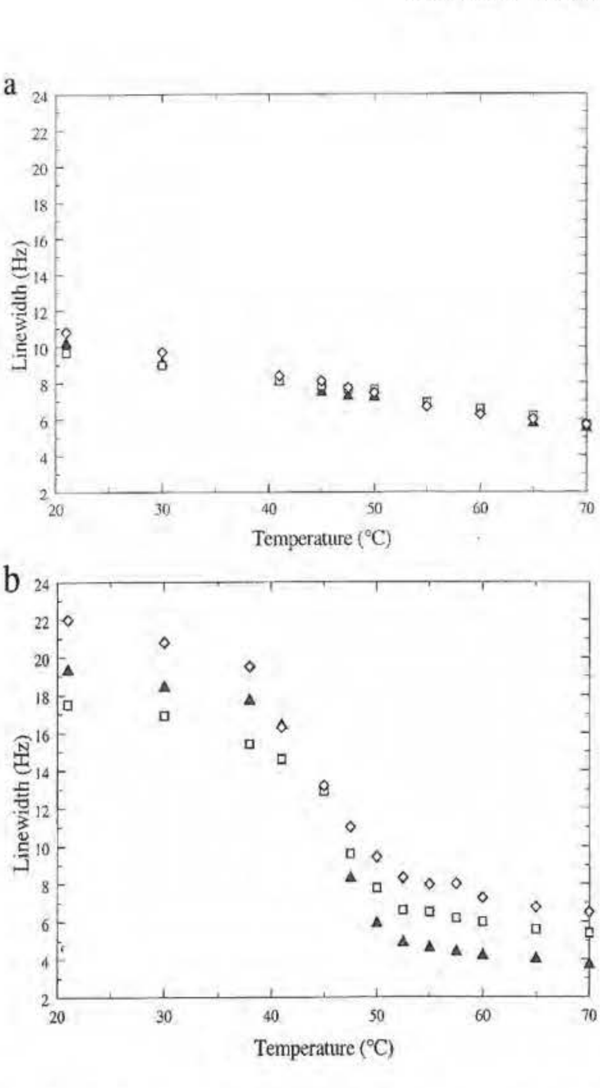

*Figure 2.2: $^1$H NMR line width vs. temperature for a solution of aPMMA (a) and sPMMA (b) in toluene-$d_8$ having a polymer mass fraction of 0.10: (▲) methoxy, (□) $\alpha$-methyl and (◇) backbone methylene.*

While the line width decreases continuously for aPMMA, mainly due to a lowering of the viscosity, a clear sigmoidal transition, characteristic for a conformational transition, is observed for sPMMA. The transition temperature of this helix to random coil transition is situated around 45 °C in agreement with FTIR and rheology observations.[2,17] A quite similar transition temperature of about 45 °C is observed for the $\alpha$-methyl, the methoxy and the backbone methylene resonances. The line widths of aPMMA are measured after deconvolution of the NMR signals. The line width of sPMMA at low temperatures is larger as compared to this of aPMMA due to the gelation (reduced mobility) of sPMMA.

Besides the advantage that this method is fast as compared to spin-spin relaxation time measurements, some drawbacks in using the line width of NMR resonances to study conformational transitions have to be mentioned. 1) If two proton environments of the same functionality strongly differ in molecular mobility ($T_2$ relaxation time), a superposition of a sharp and broad resonance signal should be present. However, probably the broad resonances will not be detected at the line width at half heights. 2) The line width is dependent on the homogeneity of the magnetic field. 3) An accurate determination of the line width is often complicated by (higher) tacticity effects (e.g. pentad splitting) in polymers. Moreover no quantification of the amount of helical structures is possible from a line width analysis.

The line width experiments show clearly the melting region and the transition temperature of the gel. More accurate and quantified results regarding the transition of the molecular motions can be obtained by $T_2$ relaxation time measurements.

### 2.2.3 Spin-spin relaxation time ($T_2$) measurements

The spin-spin relaxation times for two different groups, i.e. the $\alpha$-methyl and the ester methyl were measured. The intensity versus evolution time relationship can vary from simple mono-exponential to a three exponential behaviour, as clearly revealed by logarithmic plots. A multi-exponential analysis is justified if the resulting relaxation times differ considerably. Moreover, an acceptable part of the proton fraction has to correspond to each $T_2$ decay time.

#### 2.2.3.1 Temperature dependence of the $T_2$ relaxation behaviour

The temperature dependence of the $T_2$ relaxation time was investigated for the $\alpha$-methyl and the methoxy group of both aPMMA and sPMMA. Solutions with a polymer mass fraction of 0.10 in toluene were used.

### α-methyl group

For aPMMA, a mono-exponential behaviour of the integrated intensity (total intensity of the region) versus evolution time is observed for the α-methyl group over the whole temperature range. This corresponds to a single $T_2$ decay time. The change of $T_2$ as a function of the temperature is shown in Figure 2.3a. The continuous increase of $T_2$ reflects the increase in molecular mobility with temperature, mainly caused by a decrease of the viscosity of the solution. Similar results were obtained upon analysing the rr and mr triad resonance signals of the α-methyl group separately.

For sPMMA the situation is more complex. The $T_2$ decay time could be fitted only by a bi-exponential approach for temperatures up to 50 °C, as illustrated in Figure 2.3b (Δ, long $T_2$ decay time or $T_2^l$; O, short $T_2$ decay time or $T_2^s$). At 21 °C, 28% of the α-methyl groups has a short $T_2$ relaxation time (low molecular mobility), while 72% has a long $T_2$ relaxation time (high molecular mobility). The temperature dependence of these fractions is represented in Figure 2.3c. They are almost constant up to 38 °C. A further increase of temperature increases the fraction with high molecular mobility at the expense of the fraction with low molecular mobility.

Above 50 °C the data can be analysed using a single $T_2$ relaxation time (Figure 2.3b). The temperature dependence of the long $T_2$, $T_2^l$ is quite similar to that of the mono-exponential $T_2$ relaxation time of the α-methyl group of aPMMA (Figure 2.3a vs. b).

As expected, slow exchange is observed between the helix and the random coil environment on the NMR time scale, resulting in two $T_2$ relaxation times up to 50 °C. This means that the rate of exchange between the helix and random coil is slow as compared to the difference in $1/T_2$. The fraction with the short $T_2$ decay time (28 %) reflects the amount of helix structures and shows a transition temperature of 45 °C, in agreement with the FTIR, rheology and line width results.[2] Notice that at high temperatures the $T_2$ decay times of a- and sPMMA are identical. This means that the helix-to-coil transition is only observed in the line width analysis because the short $T_2$ decay time of the helix is still long enough to contribute to the line width of the observed resonance signal at half height.

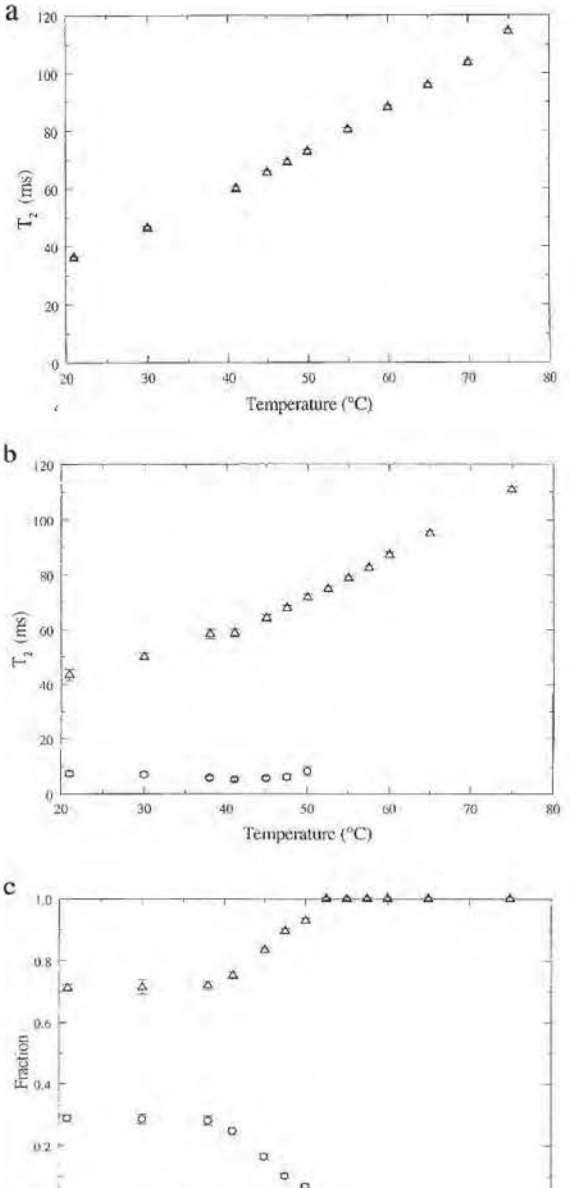

*Figure 2.3: $T_2$ decay time vs. temperature for the $\alpha$-methyl group in toluene-$d_8$: (a) aPMMA; (b) sPMMA, ($\Delta$) long $T_2$ or $T_2^l$; (O) short $T_2$ or $T_2^s$. (c) Fraction distribution vs. temperature of the fractions of the groups with very low mobility, $T_2^s$ (O), and with high mobility, $T_2^l$ ($\Delta$), for sPMMA in toluene-$d_8$.*

## Methoxy group

For aPMMA the experimental data obtained for the $OCH_3$ group can only be analysed using a bi-exponential fitting. The temperature dependence of both $T_2$ values is reported in Figure 2.4a. Figure 2.4b represents the fractional distribution of the methoxy groups over the two relaxation times. A quasi-sigmoidal variation in the temperature dependence is observed between 48 °C and 60 °C. At 21 °C, the ratio of distribution values of {mobile or $T_2^l$}/{less mobile, medium $T_2$, or $T_2^m$}, is $[T_2^l]/[T_2^m] = 0.30/0.70 = 0.43$. This ratio increase slightly with temperature up to 48 °C after which it decreases to $0.20/0.80 = 0.25$ at 75 °C. Comparable results are obtained by analysing the two main methoxy resonance signals separately.

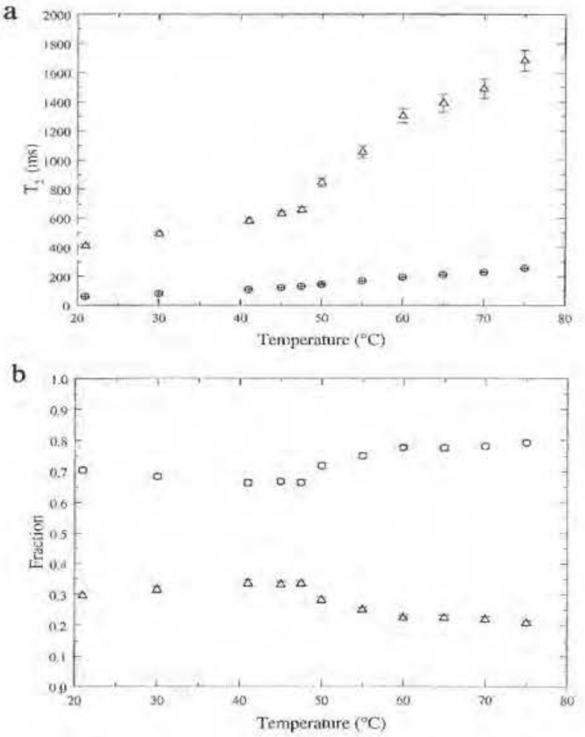

*Figure 2.4: (a) Temperature dependence of $T_2$ for the $OCH_3$ of aPMMA in toluene-$d_8$:long $T_2$ decay time (Δ) and medium $T_2$ decay time (O). (b) Temperature dependence of the fractions of groups with medium mobility, $T_2^m$ (O), and with high mobility, $T_2^l$ (Δ), for aPMMA in toluene-$d_8$.*

For sPMMA a three exponential fit is required in the temperature range between 21 °C and 50 °C and three relaxation times have to be taken into account: $T_2^l$ and $T_2^m$ as observed for aPMMA and a third, very short, relaxation time, $T_2^s$, that corresponds to methoxy groups having a very low mobility. The temperature dependence of all three decay times and the corresponding fractions are represented in Figure 2.5a-b.

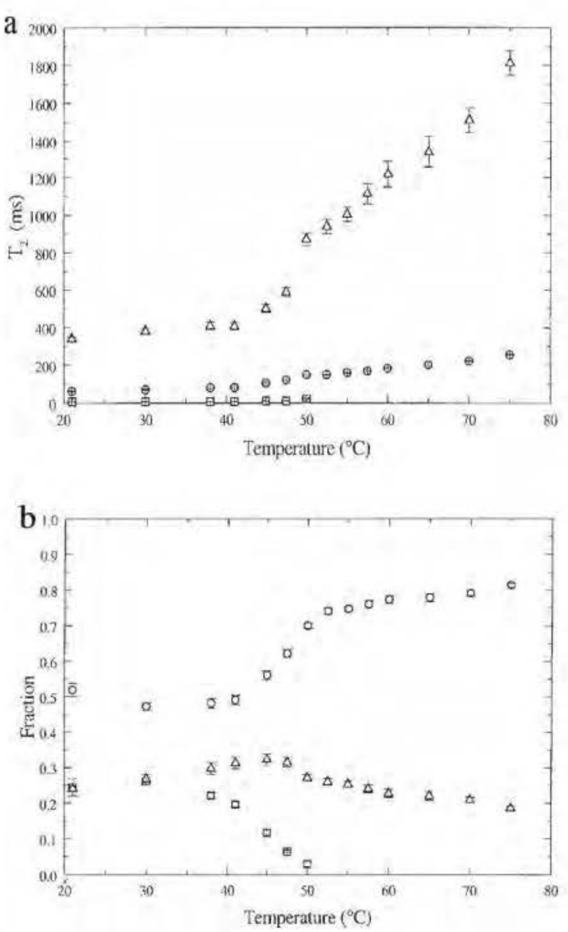

*Figure 2.5: (a) Temperature dependence of $T_2$ for the $OCH_3$ of sPMMA in toluene-$d_8$: long $T_2$ decay time (Δ), medium $T_2$ decay time (O) and short $T_2$ decay time (□). (b) Temperature dependence of the fractions of groups with very low mobility, $T_2^s$ (□), with medium mobility, $T_2^m$ (O) and with high mobility, $T_2^l$ (Δ), for sPMMA in toluene-$d_8$*

The values and the temperature dependence of both $T_2^l$ and $T_2^m$ are very similar to what is observed for aPMMA. On the other hand, the values of $T_2^s$ are much shorter, pointing to the presence of a fraction of methoxy groups with very low mobility. At 21 °C, this fraction is around 0.24, a value close to the fraction obtained for the α-methyl group (Figure 2.3c). This fraction and decay time, representing methoxy groups with very low mobility has completely disappeared around 55 °C, i.e. at the temperature at which both G' and FTIR band intensities level of in the heating mode. These observations allow to conclude that the methoxy groups with very low mobility belong to the chain repeating units incorporated in the helical junctions. At 21 °C, $[T_2^l]/[T_2^m] = 0.24/0.52 = 0.46$, i.e. very close to the ratio observed for aPMMA (0.43). This fraction has decreased to about 0.20/0.80 at 75 °C, as for aPMMA. Figure 2.6 shows the difference plot of the fraction distribution of sPMMA and aPMMA as a function of temperature. The helix fraction (shortest $T_2$) mainly adds up to the intermediate component ($T_2^m$). More precisely, the fraction corresponding to this group passes from 0.70 in aPMMA to 0.52 in sPMMA. The difference (0.18) amounts to 75 % of the fraction of groups of sPMMA with very low mobility, $T_2^s$ (0.24).

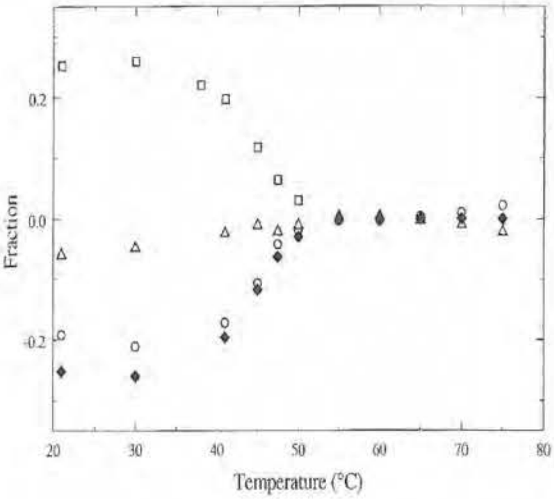

*Figure 2.6: Difference plot of the fraction distribution for the methoxy region of sPMMA and aPMMA vs. temperature. (□) helical phase, (○) intermediate molecular mobility, (Δ) high molecular mobility and (◆) sum of the two last fractions.*

### 2.2.3.2 Influence of the solvent and the tacticity

The amount of helices participating in the gel formation has been quantified out of the temperature dependence of the $T_2$ relaxation times. Still striking is the appearance of two $T_2$ decay times for the methoxy NMR resonance of sPMMA and aPMMA in toluene-$d_8$ even at high temperature. To get a better understanding of the origin of $T_2^l$ and $T_2^m$, the influence of the solvent or a possible structure formation in solution were investigated by performing the same measurements in $CDCl_3$. In $CDCl_3$, being a good solvent for PMMA, no thermoreversible gelation of sPMMA into helix structures appears. Even at low temperatures, only two relaxation times are observed for sPMMA, $T_2^l$ and $T_2^m$. The fractional distribution of methoxy groups with high and medium mobility at 21 °C is $[T_2^l]/[T_2^m] = 0.32/0.68 = 0.47$ for both sPMMA and aPMMA. This value is in good agreement with the values observed in toluene, a solvent in which gelation takes place at low temperature. This demonstrates that the bi-exponential behaviour of the methoxy group is not solvent induced.

Moreover, a fraction distribution of 0.30/0.70 observed for aPMMA as well as for sPMMA and iPMMA at 21 °C, confirms that the bi-exponential behaviour is not due to tacticity differences.

To exclude the occurrence of (unexpected) cis-trans isomers, due to hindered rotation around the O-CO bond and resulting in syn and anti orientations of the O-Me bond with respect to the C=O bond, the $T_2$ relaxation behaviour of two model esters compounds, methylpropionate and methyl-2,2-dimethylpropionate, was determined. As expected, the methoxy group of both compounds shows a mono-exponential $T_2$ relaxation behaviour.

### 2.2.3.3 Concentration dependence and influence of temperature

The concentration dependence of the fraction distribution $[T_2^l]/[T_2^m]$ of the methoxy group was investigated for solutions of aPMMA.

At 21 °C the $T_2$ relaxation behaviour is bi-exponential over the whole concentration range (polymer weight fractions between 0.2 and 0.0001) showing a constant fraction distribution, $[T_2^l]/[T_2^m] = 0.30/0.70 = 0.43$ in toluene as well as in chloroform. Both $T_2$ values increase upon lowering the polymer concentration due to the decreasing viscosity of the solutions. The $T_2$

relaxation times and the matching fractions of the methoxy signal of aPMMA in toluene-$d_8$, as a function of the concentration are represented in Figure 2.7.

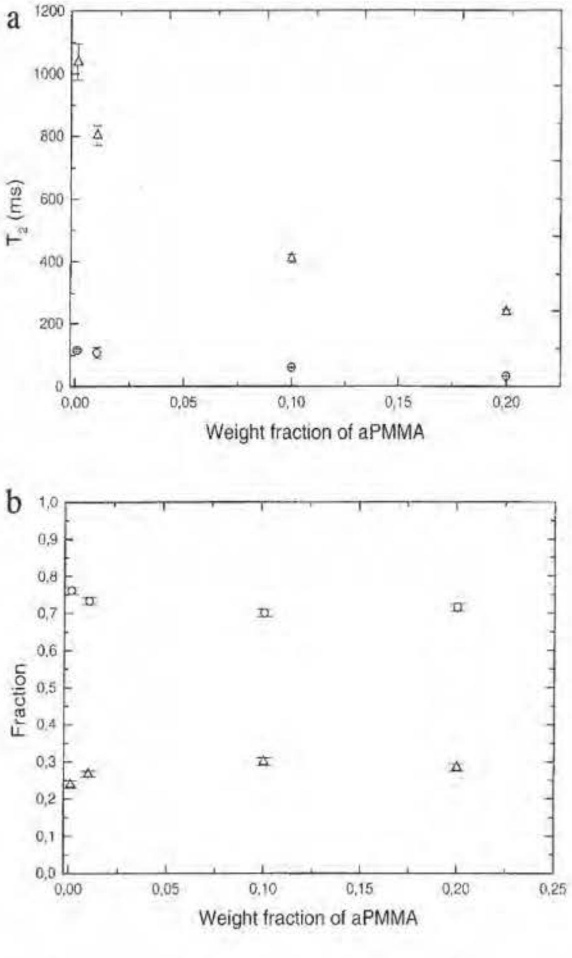

*Figure 2.7: Concentration dependence of the $T_2$ relaxation of the methoxy group of aPMMA in toluene-$d_8$ at 21 °C. (a) $T_2$ as a function of concentration: (O) $T_2^m$; (Δ) $T_2^l$. (b) Fraction distribution as a function of concentration: (O) $T_2^m$; (Δ) $T_2^l$.*

At high temperature the $T_2$ relaxation behaviour however behaves quite different (Figure 2.8 a-b). For polymer concentrations, $w_2 \geq 0.10$ in toluene-$d_8$ at 102°C the fraction distribution remains quasi unaffected (0.20/0.80) while both $T_2$ values also decrease slightly with increasing concentration (not shown in figures). Upon diluting to polymer weight fractions between 0.10 and 0.0001, the fraction of the long $T_2$ component (most mobile environment) starts to increase while both time constants decrease (Figure 2.8a-b).

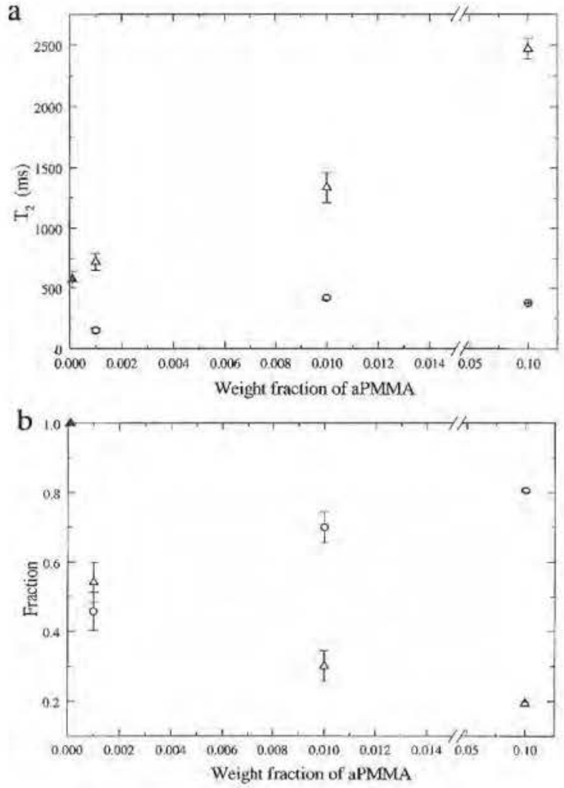

*Figure 2.8:Concentration dependence of the $T_2$ relaxation of the methoxy group of aPMMA in toluene-$d_8$ at 102 °C. (a) $T_2$ as a function of concentration: (O) $T_2^m$; (Δ) $T_2^l$; (▲) mono-exponential $T_2$ behaviour. (b) Fraction distribution as a function of concentration: (O) $T_2^m$; (Δ) $T_2^l$; (▲) mono-exponential $T_2$ behaviour.*

To understand this decrease in $T_2$ decay times (lowering of a molecular mobility) one has to realise that each $T_2$ component represents the weighted average of a population (distribution) of molecular mobilities. Upon diluting, the methoxy groups in the most mobile environments of the less mobile population (short $T_2$ population) add up to the mobile (long $T_2$) population, reducing the average molecular mobility of the latter. Of course, also the average molecular mobility of the less mobile $T_2$ population decreases. At polymer weight fractions ≤ 0.0001 the relaxation behaviour clearly becomes mono-exponential with a $T_2$ decay time of 573 ms. This is an indication that the bi-exponential behaviour of the methoxy group could be the result of intermolecular polymer-polymer interactions.

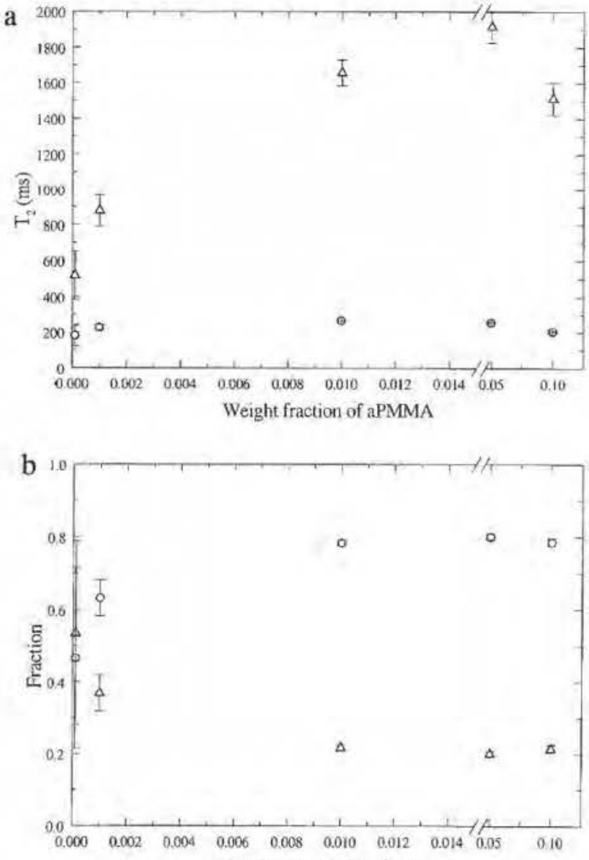

*Figure 2.9:Concentration dependence of the $T_2$ relaxation of the methoxy group of a solution of aPMMA in $CDCl_3$ at 55 °C. (a) $T_2$ as a function of concentration: (O) $T_2^m$; (Δ) $T_2^l$. (b) Fraction distribution as a function of concentration: (O) $T_2^m$; (Δ) $T_2^l$.*

In $CDCl_3$ the fraction distribution also remains unaffected for polymer weight fractions ≥ 0.01 (0.20/0.80). As for toluene, further dilution towards a polymer weight fraction of 0.0001 results in an increase of the fraction of the long $T_2$

component while both $T_2$ decay times decrease (Fig. 2.9a-b). Although at polymer weight fractions of 0.0001 the $T_2$ behaviour can be analysed bi-exponentially, the difference between both $T_2$ decay times has seriously dropped ($T_2$ ratio of about 2.5) while the error of the analysis seriously increased. This is a clear indication that a single $T_2$ decay time will be observed upon further dilution. With respect to toluene the intermolecular polymer-polymer interactions in $CDCl_3$ only disappear completely at somewhat lower polymer concentrations. This can be explained by the difference in solvent quality of the two solvents with respect to PMMA. $CDCl_3$ is known to be a better solvent for PMMA than toluene. In $CDCl_3$ the radius of gyration of the polymer is larger than in toluene. This means that the critical overlap concentration, the concentration at which polymer chains starts to overlap, has to be lower in $CDCl_3$ than in toluene and explains the difference in concentration where the $T_2$ behaviour becomes mono-exponential. However, neither the difference in temperature (55 °C for $CDCl_3$ versus 102 °C for toluene) at which the measurement took place can be excluded.

In summary it can be concluded that the large fraction with short $T_2$ decay time represents highly associated ester groups while the long $T_2$ decay time arises from solvated ester groups that are more free. Zajicek e.a.[40] observed already a spatial anisotropy of internal motions for highly concentrated ($w_2 > 0.30$) solutions of PMMA in $CDCl_3$ by $^1H$ MAR (Magic Angle Rotation) NMR which was ascribed to intermolecular interactions of the ester groups. Notice that this intermolecular interaction is rather strong since even at 102 °C the rate of exchange between the intermolecular associated and non-associated environment is slow enough to be observed by NMR.

## 2.3 Conclusions

NMR relaxation measurements have shown to be a powerful tool for the study of the helix-to-coil transition and the quantification of the helical phase in gels of sPMMA in toluene. Upon heating the amount of helical phase starts to decrease around 40°C and has completely disappeared at 55°C, the gel melting point. The conformational transition can be observed from line width analysis as well as by the $T_2$ relaxometry. In this chapter the advantage of a $T_2$ relaxation time analysis vs. line width analysis is demonstrated. Although both techniques can be used to detect the transition region, quantification of the different phases is only possible by means of $T_2$ relaxation experiments. In the gel of sPMMA in toluene at ambient temperature about 25% of the repeating units is build in the helical phase. These NMR $T_2$ relaxometry results were used to calibrate a FTIR method for the quantification of the amount of helical phase.

Moreover, the bi-exponential $T_2$ relaxation behaviour of the methoxy signal of aPMMA (and sPMMA above 55 °C) is caused by intermolecular polymer-polymer interactions. These intermolecular interactions are rather strong since even at high temperature the rate of exchange between the non-associated and the associated environment is slow enough to be observed by NMR.

## 2.4 Experimental part

### 2.4.1 Materials.

All materials used in this chapter were synthesised at the Laboratory of Polymer Research at the University of Leuven. A short overview of this synthesis is given below.

sPMMA was polymerised in toluene using aluminium triethyl and titanium (IV) chloride as the catalyst at - 78 °C. The atactic isomer (aPMMA) was supplied by ICI under the trade name of Diakon. The tacticity was evaluated by analysis of $^{13}$C NMR spectra in $CDCl_3$ and was based on the intensities of the $\alpha$-methyl triads. The molecular weight was determined by GPC at room temperature in tetrathydrofuran. The characteristics of the polymers are reported in Table 2.1.

| | $M_n$ kg/mol | $M_w$ kg/mol | % syndiotactic triads (rr) | % heterotactic triads (rm) | % isotactic triads (mm) |
|---|---|---|---|---|---|
| sPMMA | 108 | 195 | 88.0 | 12.0 | 0.0 |
| aPMMA | 91 | 149 | 58.0 | 37.0 | 5.0 |

*Table 2.1: Characteristics of the PMMA samples.*

*Preparation of solutions and gels.*

Homogeneous solutions for the high-resolution NMR measurements were first prepared in glass tubes. These tubes were sealed under vacuum and the solution was then homogenised at a temperature near the boiling point of the solvent for a few hours. After homogenising the solution was cooled to room temperature and transferred into 5mm NMR tubes. These tubes were also sealed under vacuum to keep the concentration of the solutions constant. Preparing the samples in this way prevents the presence of air bubbles in the gel that could disturb the relaxation measurements. The solvents used for the relaxation measurements were in the deuterated form: toluene-$d_8$ (Acros, 100.0% atom D) and $CDCl_3$ (>99.5% atom D). The polymer concentration is expressed as polymer mass fraction, $w_2$ (typically $w_2 = 0.10$). The use of different concentrations is explicitly indicated in the text.

## 2.4.2 Experimental techniques

*The CPMG pulse sequence*

The CPMG (Carr-Purcell-Meiboom-Gill) pulse sequence,[41,42] used to determine the $T_2$ relaxation times is schematically represented in Figure 2.10. The CPMG pulse sequence is based on a spin-echo sequence,[43] a 90° pulse which is followed by a series of 180° refocusing pulses.

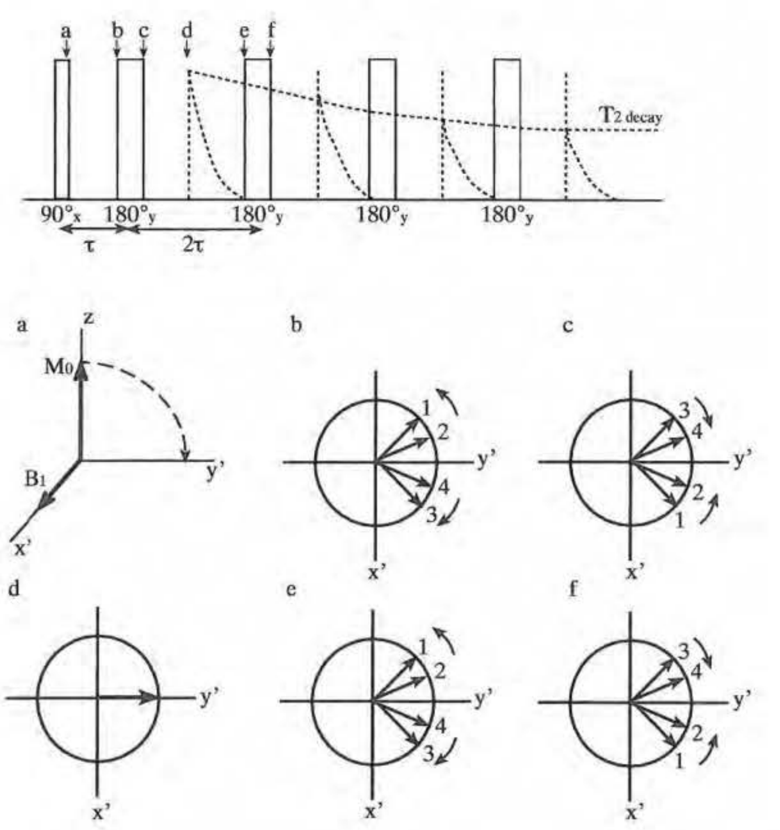

*Figure 2.10: Schematic representation of the CPMG pulse sequence. The 90° pulse in the x' direction is followed by a variable set of 180° pulses in the y' direction*

The magnetisation is excitated by a 90° pulse along the x' axis into the +y' axis (Figure 2.10a). After application of the 90° pulse, the magnetisation vectors fan out (Figure 2.10b) due to $T_2$ relaxation but also due to inhomogeneities of $B_0$ over the sample volume. This should result in an observed $T_2^*$, which is shorter than the intrinsic $T_2$. Therefore, after a period of dephasing $\tau$ (TE/2), a refocusing pulse of 180° along the y' direction, is applied. The isochromats continue to move in their original sense and so rephase along the y'-axis after a further time $\tau$ (Figure 2.10d). The echo then seen will be reduced in amplitude by an amount, which depends solely on the natural $T_2$. They then again disperse during a second $\tau$ period and will be refocused by a next 180° pulse after a period $2\,\tau$(Figure 2.10e-f). Thus, the 90° pulse is followed by a series of 180° pulses and the time between the 180° pulses is twice the time interval between the 90° pulse and the first 180° pulse. The echoes are observed halfway between two 180° pulses. Detection occurs after a variable time $t = 4n\,\tau$ with n an integer.

The decline of the intensity of the echo signals is determined by $T_2$ as follows:

$$M = M_0 \exp(-t/T_2) \tag{2.2}$$

*Parameters*

High-resolution NMR experiments were performed on a Varian Inova 400 spectrometer equipped with a dedicated 5 mm proton probe. The proton spin-spin relaxation times ($T_2$) were measured using the CPMG pulse sequence $(\pi/2)_X - (\tau - \pi_Y - \tau)_n$ - acquisition with $\tau = 0.2$ ms and $4n.\,\tau$ the total time for $T_2$ relaxation. The latter is an array of 35 values varying from 0.8 ms to 0.8 s. All experiments are performed with 8 scans, a preparation delay of 5 s, an acquisition time of 2.2 s and a $\pi/2$ pulse width of 4.85 μs while the temperature was controlled with an accuracy of 0.1 °C.

To measure under equilibrium conditions, the successive $T_2$ experiments were accomplished as a function of increasing temperature (to avoid hysteresis that occurs upon cooling) and were initiated only after a thermal stabilisation period of at least 20 min. A typical standard deviation of about 3% was obtained from $T_2$ measurements (in 4-fold) at 21 °C, 45 °C and 70 °C. These measurements were done on the same sample but with an equilibration period of at least several days between consecutive sessions.

Non-linear least square multi-exponential analysis of all relaxation data were accomplished on a Macintosh computer using the program KaleidaGraph 3.0 (Marquardt-Levenberg algorithm).

In the figures representing the temperature and concentration dependence of the $T_2$ relaxation times and fractions, error bars indicate the 95% confidence interval.

## 2.5 References

1 Ruytinx, B. 'Structuurvorming in oplossingen van stereoregelmatige vinylpolymeren', doctoraatsproefschrift, KULeuven (1999).

2 Ruytinx, B.; Berghmans, H.; Adriaensens, P.; Storme, L.; Vanderzande, D.; Gelan, J. *Macromolecules* **2001**, 34,3,522.

3 Sperling, L.H. 'Introduction to Physical Polymer Science', John Wiley & Sons, Inc.; New York, (1992).

4 Till, P.H. *J. Polym. Sci., Part B, Polym. Phys.* **1996**, 34, 1169.

5 Vereecke, S. 'Fasegedrag en structuurvorming in oplossingen van polyethyleen Doctoraatsproefschrift', KULeuven, (1998).

6 Aerts, L.; Kuntz, M.; Berghmans,H.; Koningsveld, R. *Makromol. Chem.* **1993**, 194, 2697.

7 Stoks, W.; Berghmans, H.; Moldenaers, P.; Mewis, J. *Brit. Polym. J.* **1988**, 20,361.

8 Stoks, W.; Berghmans, H. *J. Polym. Sci.,Part B, Polym. Phys* **1991**, 29.601.

9 Arnauts, J.; Berghmans, H. *Polym. Commun.* **198**, 28, 66.

10 Vandeweerdt, P.; Berghmans, H.; Tervoort, Y. *Macromolecules* **1991**, 24.3547.

11 Rees, D.A. *Pure Appl. Chem.* **1981**, 53, 1.

12 Berghmans, H.; Donkers, A.; Frenay, L; ;Stoks, W.; De Schrijver, F.C.; Moldenaers, P.; Mewis, J. *Polymer* **1987**, 28.97.

13 Deberdt, F.; Berghmans, H. *Polymer* **1993**, 34, 2192.

14 Deberdt, F.; Berghmans, H. *Polymer* **1994**, 35, 1694.

15 Roels, T.; Deberdt, F.; Berghmans, H. *Macromolecules* **1994**, 27, 6216.

16 Berghmans, M.; Thijs, S.; Corette, M.; Berghmans, H.; De Schrijver, F.C. *Macromolecules* **1994**, 27, 7669.

17 Buyse, K.; Berghmans, H.; Bosco, M.; Paoletti, S. *Macromolecules* **1998**, 31, 9224.

18 Chambon, F.; Petrovic, Z.S.; Macknight, W.; Winter, H.H. *Macromolecules* **1986**, 19, 2146.

19 Winter, H.H.; Morganelli, P.; Chambon, F. *Macromolecules* **1988**, 21, 532.

20 Mezger, T. 'A little course in rheology. Part 1', Physica Messtechnik GmbH, Germany (1998).

21 Spevacek, J., Schneider, B.; Bohdanecky, M.; Sikora, A. *J. Polym. Sci., Part B: Polym. Phys.* **1982**, 20, 1624.

22 Spevacek, J. *J. Polym. Sci., Part B: Polym. Phys.* **1978**, 16, 523.

23 Mrkvickova, L.; Stejskal, J.; Spevacek, J.; Horska, J.; Quadrat, O. *Polymer* **1983**, 24, 700.

24 Sedlacek, B.; Spevacek, J.; Mrkvickova, L.; Stejskal, J.; Horska, J.; Baldrian, J.; Quadrat, O. *Macromolecules* **1984**, 17, 825.

25 Zajicek, J. *Makromol. Chem.* **1981**, 182, 3169.

26 Zajicek, J. *Makromol. Chem.* **1981**, 182, 3177.

27 Spevacek, J.; Schneider, B.; Straka, J. *Macromolecules* **1990**, 23, 3042.

28 Hatada, K.; Okamoto, Y.; Ohta, K.; Yuki,H. *J. Polym. Sci. , Polym. Lett. Ed.* **1976**, 14,51.

29 Inoue, I; Konno,T. *Makromol. Chem.* **1978**, 179,1311.

30 Spevacek, J.; Suchoparek, M. *Macromolecules* **1997**, 30, 2178.

31 Dybal, J.; Stokr, J.; Schneider, B. *Polymer* **1983**, 24,971.

32 Spevacek, J.; Schneider, B.; Baldrian, J.; Dybal, J.; Stokr, J. *Polymer Bulletin* **1983**, 9, 495.

33 Spevacek, J.; Schneider, B.; Dybal, J.; Stokr, J.; Baldrian, J.; Pelzbauer, Z. *J. Polym. Sci., Part B: Polym. Phys.* **1984**, 22, 617.

34 Dybal, J.; Spevacek, J.; Schneider, B. . *J. Polym. Sci., Part B: Polym. Phys.* **1986**, 24, 657.

35 Kusuyama, H.; Takase, M.; Tseng, H-T.; Chatani, Y.; Tadokoro, H. *Polymer* **1982**, 23, 1256.

36 Saiani, A.; Guenet, J-M. *Macromolecules* **1997**, 30, 966.

37 Saiani, A.; Spevacek, J.; Guenet, J-M. *Macromolecules* **1998**, 31, 703.

38 Rees, D.A. *Pure Appl. Chem.* **1981**, 53,1.

39 Ibbett, R.N. NMR spectroscopy of Polymers; Blackie academic & Professional: Glasgow, Scotland, 1993, Chapter 1.

40 Zajicek, J.; Pivcova, H.; Schneider, B. *Makromol. Chem.* **1981**, 182, 3169.

41 Hahn, E.L. *Phys. Rev.* **1950**, 80,580.

42 Carr, H.Y.; Purcell, E.M. *Phys. Rev.* **1954**, 94, 630.

43 Meiboom, S.; Gill, D. *Rev. Sci. Instr.* **1958**, 29(8), 688.

# 3

# NMR relaxometry in the solid state: Comparative morphological study of PDXL/PMMA segmented networks and blends

A solid state relaxometry investigation on the morphology of poly(dioxalane) (PDXL)/ poly(methyl methacrylate) (PMMA) segmented networks and the corresponding polymer blends, is described in this chapter.

The NMR study is performed in co-operation with the Laboratory of Polymer Research at the University of Gent as part of an 'Interuniversity Attraction Pole' (IUAP) collaboration. The synthesis of the segmented polymer networks with varying PDXL/PMMA ratio and the corresponding polymer blends is performed at the laboratory of Professor Goethals and Professor Du Prez at the University of Gent. The examination on the morphology of these materials by thermal analysis (executed at the Laboratory of Polymer Research) and the NMR relaxation study results in a detailed clarification of the phase morphology.[1] The morphology on the nanometer scale, determined by the way of preparation, is very important in view of the technical applications of this kind of materials.

## 3.1 Introduction

When two polymers are mixed, the most frequent result is a system that exhibits almost total phase separation. Qualitatively this can be explained in terms of the reduced combinatorial entropy of mixing two types of polymer chains. Prior to the 1970s, the scientific literature on polymer blends was dominated by the idea that polymer-polymer miscibility would always be the rare exception. This was based on numerous experiments, and the theoretical work of Scott.[2] Thus the usual endothermic heat of mixing and the very small combinatorial entropy of mixing made it seem unlikely to realise the necessary negative free energy of mixing. In response to the developing field of polymer blends, the Flory-Huggins theory has been developed. This theory predicts the free energy of mixing polymer solutions by considering the polymer molecules to be chains of segments, each segment being equal in size to a solvent molecule.

The evolution of modern polymeric materials emanates largely from the combination of different polymers into one compatible blend. Due to grafting of polymers with reactive end-groups, the synthesis of block copolymers and the combination of polymers in networks, polymers are forced to compatibilise and a combination of the properties of both polymers is obtained in the final material.

### 3.1.1 Different kinds of polymeric networks

Two important classes of multicomponent polymer networks can be distinguished, namely interpenetrating polymer networks (IPNs) and cross-linked multicomponent networks.

IPNs are combinations of two or more polymers in network form; with at least one synthesised in the presence of the other. Semi-interpenetrating networks are constituted by an entangled combination of two polymers. Only one polymer is cross-linked, the other one is linear or branched.[3]

In cross-linked multicomponent networks one polymer is bonded to the other at both chain ends or at various points along the chains. The total product is a network composed of two different polymers. Segmented networks (SPNs) are formed if one polymer is an end-functionalised macromolecular cross-linker for the other polymer; the ends may be grafted to different chains or the same chain. Segmented networks are a sub-class of cross-linked multicomponent networks.[4] These structures are illustrated in Figure 3.1.

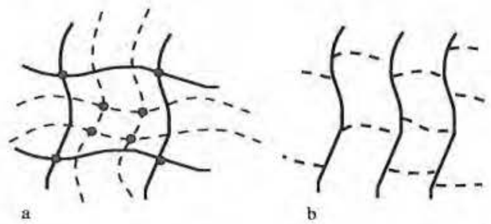

*Figure 3.1: (a) An interpenetrating network (IPN) and (b) a cross-linked multicomponent network.*

When properly engineered, most IPNs do not interpenetrate at the molecular level. They may form divided phase domains in the nanometer size range, which interpenetrate one another, forming co-continuous materials. It is often the co-continuous phase behaviour of IPNs that leads to their unique properties which result in a wide range of application possibilities such as biomaterials, membranes, solid phase extraction etc. Due to the chemical cross-links in cross-linked multicomponent networks, intrinsically immiscible polymers could be combined and a greater control of the phase morphology of the end products is allowed. The physicochemical properties of these networks are expected to be the result of a combination of the properties of segmented structures such as block or graft copolymers on one hand and of polymer networks on the other hand. Properties may be varied by changing the cross-link density what will change the domain sizes in the segmented networks.

### 3.1.2 Preparation of SPNs

Bamford and Eastmond described a general method of preparing cross-linked multicomponent networks.[4] Radical sites on the side groups of polymer A are formed by removing the halogen atoms by a metal carbonyl. These macroradicals initiate polymerisation of monomer B to produce growing chains of polymer B attached to the A-chains. Combination termination of the propagating grafts produces cross-links of polymer B. In this way, cross-links of polymer B are randomly introduced into an assembly of chains of polymer A. In another case of preparing these networks, a precursor polymer A with reactive functions at both chain ends is coupled with a multifunctional polymer B.[5] Also the lamellar liquid crystalline phase can be used as a matrix to create amphiphilic polymer networks which are highly anisotropic.[6]

However most of the preparation methods make use of telechelics or bis-macromonomers.[7,8] These are uniform-size polymers with a suitable reactive end group. They are the macromolecular building blocks for the synthesis of precisely designed cross-linked networks. Where only few of the synthesis methods result in the formation of well-defined networks with good control of the molecular weight between the cross-links and the number of branches at the junction points, the latter one does.

A few examples are mentioned briefly. Polybutadiene was polymerised by an anionic polymerisation with a reactive poly(ethylene oxide) bis-macromonomer as cross-linker to form hydrophilic-hydrophobic (amphiphilic) two-component networks.[9] Tezuka et al. proposed a system for the synthesis of two-component model networks based on a macromolecular ion-coupling reaction between pyrrolidinium and carboxylate-containing prepolymers.[10] Bis-macromonomers of hydrophobic poly(vinyl ether)s have been radically polymerised with vinyl monomers such as methyl methacrylate, butyl acrylate and hydroxyethyl acrylate for the synthesis of hydrophobic, amphiphilic or hydrophilic segmented copolymer networks by Du Prez et al.[11]
Amphiphilic networks are macromolecular substances in which segments of opposite philicity (hydrophilic and hydrophobic) are covalently bonded to form one segmented network.

### 3.1.3 Applications

Homogeneous and heterogeneous polymer networks play an important role in polymer chemistry and technology. The multipurpose character of these materials originates from their controllable nano-structure. A unique phase morphology is obtained by the method of synthesis what results in simultaneous cross-linking and phase separation.

One of the key features of amphiphilic conetworks is their capability to swell in both aqueous and organic media. For a given solvent, the degree of swelling depends on the fraction that has a good affinity with the solvent. By the selection of the network components, amphiphilic networks exhibit a different swelling characteristic.[12] In this respect, amphiphilic networks can be used as a membrane in pervaporation experiments. Pervaporation is a technique used for the separation of liquid mixtures. The feed mixture remains in contact with one side of a dense polymeric membrane, while the permeate is removed in the vapour state at the opposite side by vacuum or gas sweeping. Segmented polymer networks, in which a bis-macromonomer of hydrophilic PDXL acts as cross-linker for hydrophobic PMMA chains (and which are studied by NMR relaxometry in this chapter), have been used for the preparation of dense polymer membranes. These networks where used for the dehydration of ethanol-rich mixtures by the pervaporation technique. The homogeneity together with the mechanical stability of the segmented network structure leads to control of the permeability and the selectivity to water.[13]

Nanophase separated poly(2-hydroxyethyl methacrylate)-*l*-polyisobutylene (PHEMA-*l*- PIB) amphiphilic conetworks were obtained by Scherble et al.[14] The dry conetworks exhibited hydrophilic and hydrophobic phases. Swelling of the network with aqueous cadmium-chloride solution, followed by exposure to $H_2S$, resulted in CdS assemblies in the conetwork. These assemblies have a shape similar to the network domains they were formed in. The polymeric network served as template for nano-sized inorganic assemblies.

Segmented polymer networks with LCST (lower critical solution temperature) behaviour have been prepared by Reyntjens et al.[15] The use of thermoresponsive networks for thermocontrollable solid phase extraction (SPE) has been investigated. SPE is used for the separation and pre-concentration of analytes from non-volatile solvents (e.g. water). Normally, the selectivity is determined by the nature of the packing of the material. By the use of thermoresponsive polymer materials, the selectivity for SPE could be controlled by changing the water temperature.

Besides the abovedescribed applications these kinds of networks play an important role in other technical and chemical applications such as coatings, adhesives, matrix resins, etc.

Much less is known about the morphology development of amphiphilic conetworks, which is of great importance in view of these applications. Some morphological studies have been performed by microscopy techniques and small-angle X-ray scattering,[14] but much more efforts are necessary to correlate the nanometer scale domain structures with their physical properties. By means of $^{13}C$ solid state NMR and thermal analysis (DMA, DSC and TGA) a detailed characterisation of the morphology of PDXL/PMMA segmented networks is performed and described in this chapter.

## 3.2 Results and discussion

In the present study, SPNs with varying PDXL/PMMA ratio and the corresponding polymer blends have been prepared. Their phase morphology will be evaluated and compared by $T_{1H}$ and $T_{1\rho H}$ relaxation time studies and DMA, TGA and DSC analysis.

### 3.2.1 Material characteristics

Transparent, mechanically stable PDXL/PMMA segmented network films with three different weight fractions of PDXL, respectively about 20%, 40% and 60%, have been prepared for the solid state NMR and thermal analysis studies. The networks are coded as illustrated in the following example: *net*-poly(DXL(40)-*co*-MMA(60)). In this network, 40% PDXL bis-macromonomer has been copolymerised with 60% MMA. For convenience sake, a shorter abbreviation will be used such as 'network 40/60', in which the first number always indicates the PDXL content.

Blends with the same weight fractions of PDXL have been prepared to investigate a comparative study between segmented networks and blends. An abbreviation such as 'blend 40/60' will be used, in accordance with that for the networks, to indicate the fractions of both components in the blends. All the polymer blends have been prepared in the form of rectangular films. The blend 20/80 is a transparent material while blends with larger PDXL fractions are opaque, brittle materials.

### 3.2.2 Solid state NMR and thermal analysis of segmented networks.

For rigid polymer systems below the glass transition temperatures ($T_g$), the proton relaxation times $T_{1H}$ and $T_{1\rho H}$ provide information about the level of heterogeneity (morphology) on the nm scale due to the process of proton spin diffusion (see section 1.2.2.1).[16] At the condition of efficient spin diffusion, both proton relaxation times can be directly related to the sizes of molecular domains. The proton $T_{1\rho H}$ decay time, in the order of milliseconds, will be averaged out over a short distance (in the order of 1-2 nanometer), making it a rather local property. Since the $T_{1\rho H}$ relaxation time is sensitive to frequency motions of several tens of kilohertz, it reflects the motion of short segments in the polymer chain. The $T_{1H}$ decay time on the other hand, in the order of seconds, is sensitive to the Larmor frequency motions (several hundred MHz) and is averaged out over a larger distance (in the order of tens of nanometers), making it a more large-scale molecular property, like $T_g$. The maximum path length L, over which proton-proton spin-diffusion can occur, is approximately given by $L \approx (6DT_i)^{1/2}$ where D is the spin diffusion coefficient ($= 10^{-16} m^2/s$ for rigid solids) and $T_i$ the relaxation time $T_{1H}$ or $T_{1\rho H}$.[17] If the intrinsic relaxation times of the molecular domains are sufficiently different, multiple relaxation times will only be observed if the domain sizes are larger than L.

Figure 3.2 shows a typical $^{13}C$ solid state NMR spectrum of the network 60/40. The carbon resonances are assigned as depicted in Figure 3.2. Since the carbon resonances of PDXL are completely separated from those of PMMA, the investigation of the proton relaxation behaviour of both polymers can be investigated separately.

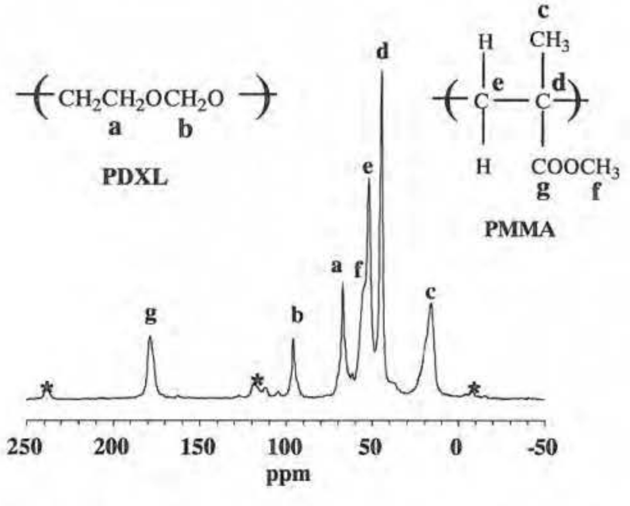

*Figure 3.2: 100 MHz solid state $^{13}C$ CP/MAS spectrum of a PDXL/PMMA segmented network. Peaks marked with an asterisk are spinning side bands.*

For the three polymer networks, a similar $T_{1H}$ decay time of ca. 0.8 s was observed via all the carbon resonances of PMMA as well as via those of PDXL due to efficient spin diffusion of proton magnetisation throughout the network (Table 3.1). This means that, if the networks have a phase separated morphology, the domain sizes have to be smaller than about 20 nm.

| Networks | $T_{1H}$ (s) | |
|---|---|---|
| | PMMA | PDXL |
| 20/80 | 0.81 | 0.81 |
| 40/60 | 0.79 | 0.78 |
| 60/40 | 0.79 | 0.79 |

*Table 3.1: $T_{1H}$ relaxation times of the segmented networks. The averaged 95% confidence limit for $T_{1H}$ is about 3%.*

Similar conclusions can be drawn from DMA-analysis of the networks. The influence of the composition on the final morphology of the segmented networks, as expressed by the shape of their dissipation factor (tan δ) versus temperature curves, is illustrated in Figure 3.3.

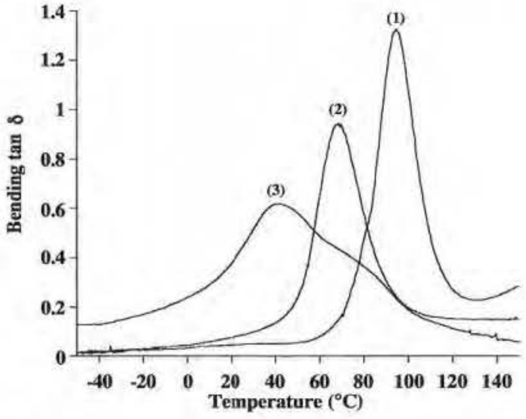

*Figure 3.3: DMA curves of the different PDXL/PMMA segmented networks: (1) network 20/80; (2) network 40/60; (3) network 60/40.*

Only a single transition, situated between the $T_g$ of PDXL (-50°C) and PMMA (110°C), is observed for all networks, which indicates the high degree of compatibility of both polymer components in the networks. The temperature corresponding to this maximum is governed by the ratio of the two components and is generally higher than the one predicted by the equation of Fox for random copolymers.[18] This phenomenon is ascribed to the decrease of the polymer chain dynamics in the networks by the introduction of the junction points between them.[13]

The forced compatibility of the two network components on a scale of 20 nm, as concluded from the $T_{1H}$ relaxation analysis, is further confirmed by the absence of crystallisation of PDXL-rich domains in DSC and DMA-curves for all the networks investigated. However, for the network with the highest PDXL content (curve 3 of Figure 3.3), a broad transition situated between the $T_g$'s of both components is observed which demonstrates its microheterogeneous phase morphology. This observation already indicates that the thermodynamics of phase separation between PDXL and PMMA begin to rule the overall phase morphology and are not counterbalanced anymore by the forced compatibility between them.

For the investigation of the phase morphology on the nanometer scale, the $T_{1\rho H}$ decay times of the network components have been determined (Table 3.2).

| Networks | $T_{1\rho H}$ (ms) | $T_{1\rho H}^L$ (ms)/ $M_0^L$ (%) | $T_{1\rho H}^S$ (ms)/ $M_0^S$ (%) |
|---|---|---|---|
| | PMMA | PDXL | PDXL |
| 20/80 | 9.4 | 9.3/47 | 1.0/53 |
| 40/60 | 7.1 | 6.8/32 | 0.9/68 |
| 60/40 | 5.5 | 5.3/34 | 1.0/66 |

*Table 3.2: $T_{1\rho H}$ relaxation times of the segmented networks. For $T_{1\rho H}$ of PDXL, the $T_{1\rho H}^L$ and $T_{1\rho H}^S$ fractions ($M_o^L$ and $M_0^S$) are normalised to 100. The averaged 95% confidence limit for $T_{1\rho H}$ and $M_0$ is about 7% and 10%, respectively.*

For both PDXL carbon resonances, the $T_{1\rho H}$ decay behaves bi-exponentially resulting in a short ($T_{1\rho H}^{S}$) and long ($T_{1\rho H}^{L}$) $T_{1\rho H}$ decay time. The bi-exponential character of the $T_{1\rho H}$ decay of PDXL is clearly demonstrated in Figure 3.4, in which an example of a curve fit, both in mono- and bi-exponential mode is given. Since both decay times are rather identical for both the $OCH_2$ and $OCH_2CH_2O$ carbon resonance, their averaged value is presented in Table 3.2.

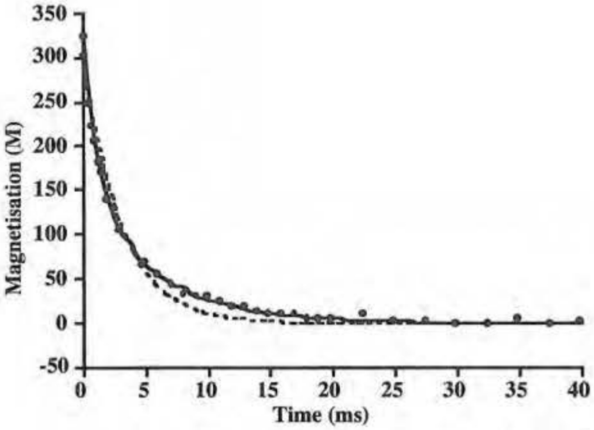

*Figure 3.4: Example of a bi-exponential curve fit of the $T_{1\rho H}$ decay of PDXL in the PDXL/PMMA networks and the blends. The mono-exponential fit is indicated by the dotted line.*

The presence of two relaxation times is indicative for a heterogeneous phase morphology on a scale of 1 to 2 nm. On the other hand, the $T_{1\rho H}$ decay time observed via all PMMA carbon resonances behaves mono-exponentially and has a value which is similar to this of $T_{1\rho H}^{L}$ of PDXL (Table 3.2). Also for PMMA only the averaged $T_{1\rho H}$ value observed via all five-carbon resonances is presented in Table 3.2.

With increasing PDXL fraction in the networks, an increase of the PMMA chain mobility is observed as expressed by the decreasing $T_{1\rho H}$ value of PMMA. Due to efficient spin diffusion between PMMA and the immobilised PDXL fraction, the $T_{1\rho H}^{L}$ of PDXL decreases in accordance with $T_{1\rho H}$ of PMMA. The relation between the $T_{1\rho H}^{L}$ decay time and chain mobility can be deducted from the log $T_{1\rho H}$ – log $\tau_c$ correlation diagram (see Figure 1.10) which shows a minimum around $\tau_c$ corresponding to the frequency of the spin lock field (50 kHz). In this diagram the $T_{1\rho H}$ decay times of PMMA and of

immobilised PDXL are situated at the long correlation time side (slow molecular dynamics).[19] An increase of the PDXL fraction in the networks will therefore result in a decrease of $\tau_c$ (higher chain mobility) and a faster $T_{1\rho H}$ relaxation (smaller $T_{1\rho H}{}^{L}$ decay value). This is further confirmed by measurements at a lower spin lock field of 25 kHz which result in a decreased $T_{1\rho H}$ value of 3.5 ms for both PMMA and the immobilised PDXL fraction ($T_{1\rho H}$ values are only dependent on the strength of the spin-lock field at the long $\tau_c$ side of the correlation diagram, see section 1.2.1.4).
From this it can be concluded that the long decay time $T_{1\rho H}{}^{L}$ represents amorphous PDXL chains that are constrained by the rigid PMMA chains due to the presence of chemical cross-links and physical entanglements. The short decay time $T_{1\rho H}{}^{S}$ of ca. 1 ms represents mobile amorphous PDXL chains, at longer distance from the rigid PMMA chains.

The varying level on which the PDXL and PMMA chains are mixed in the segmented networks, is further expressed by the comparison of their degradation behaviour (Figure 3.5).

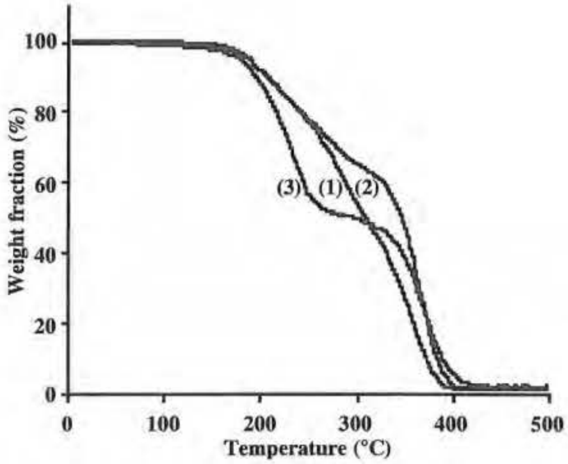

*Figure 3.5: TGA curves of the different PDXL/PMMA segmented networks: (1) network 20/80; (2) network 40/60; (3) network 60/40.*

From the TGA-curves in Figure 3.5, it is observed that the degradation behaviour strongly depends on the weight fraction of the constituting polymers. The linear homopolymer of PDXL degrades in the temperature interval between 150°C and 220°C in $N_2$ atmosphere.[13] For the network 20/80, a rather continuous degradation of the network is observed in a temperature range of 150 to 400 °C. On the other hand, network 40/60 shows a two step degradation, i.e. PDXL degrades in the region from 150 to 300 °C while PMMA degrades between 300 °C and 400 °C. For the network 60/40, the two step degradation becomes even more obvious as the degradation corresponding to PDXL is completely shifted to lower temperatures, similar to the degradation behaviour of linear PDXL. It seems that the degradation of the PDXL chains in this latter network is much less influenced by that of the PMMA chains as compared to the other networks. It is suggested that the thermal stability of these mobile PDXL chains is comparable to that of linear PDXL because of the high amount of mobile PDXL. From Table 3.2, it can indeed be observed that the relative fraction of the mobile PDXL chains ($M_0^S$) increases from about 50 to 68% for increasing PDXL contents while $T_{1\rho H}^L$ decreases.

### 3.2.3 Solid state NMR and thermal analysis of the polymer blends

Table 3.3 and 3.4 presents the $T_{1H}$ and $T_{1\rho H}$ relaxation times for the corresponding blends, respectively. In general, the polymer blends show a more heterogeneous phase morphology as compared to their network analogues. A similar $T_{1H}$ decay time for all $^{13}C$ resonances of both polymers in the blend 20/80 confirms efficient spin diffusion (Table 3.3). This means that, if molecular domains are present, they have to be smaller than 20 nm.

| Blends | $T_{1H}$ (s) | |
|---|---|---|
| | PMMA | PDXL |
| 20/80 | 0.80 | 0.80 |
| 40/60 | 0.80 | 1.10 |
| 60/40 | 0.91 | 1.10 |

*Table 3.3: $T_{1H}$ relaxation times of the polymer blends. The averaged 95% confidence limit for $T_{1H}$ is about 2%.*

On the other hand, two $T_{1\rho H}$ decay times are observed (Table 3.4). For PDXL, a $T_{1\rho H}{}^{L}$ decay time of ca. 8 ms is found which is similar to the value observed for all carbon resonances of PMMA. As for the networks, a second $T_{1\rho H}{}^{S}$ decay time of ca. 1 ms is present for the PDXL resonances. Again, $T_{1\rho H}{}^{L}$ represents the fraction of amorphous PDXL chains that are immobilised by the rigid PMMA. It means that, as for the segmented network 20/80, small PDXL domains with an estimated size between 1 nm ($T_{1\rho H}$) and 20 nm ($T_{1H}$) are present in the PMMA continuous phase.

| Blends | $T_{1\rho H}$ (ms)<br>PMMA | $T_{1\rho H}{}^{L}$ (ms)/ $M_0{}^{L}$ (%)<br>PDXL | $T_{1\rho H}{}^{S}$ (ms)/ $M_0{}^{S}$ (%)<br>PDXL |
|---|---|---|---|
| 20/80 | 8.0 | 8.0/30 | 0.9/70 |
| 40/60 | 9.0 | 6.8/65 | 1.6/35 |
| 60/40 | 9.0 | 6.8/70 | 1.6/30 |

*Table 3.4: $T_{1\rho H}$ relaxation times of the polymer blends. For $T_{1\rho H}$ of PDXL, the $T_{1\rho H}{}^{L}$ and $T_{1\rho H}{}^{S}$ fractions ($M_0^L$ and $M_0^S$) are normalised to 100. The averaged 95% confidence limit for $T_{1\rho H}$ and $M_0$ is about 4% and 7%, respectively.*

Since the PDXL chains in the blends are only constrained by physical entanglements, a reduced fraction of immobilised PDXL chains (M0L) is observed as compared to the corresponding network.

The decrease of the $T_{1\rho H}{}^{L}$ decay time from 9.4 ms for the network to ca. 8 ms for the corresponding blend reflects that the PDXL chains are less immobilised in the blend as compared to the network. This phenomenon can be ascribed to the absence of the chemical cross-links.

For the blends 40/60 and 60/40, the demixing into large molecular domains (> 20 nm), is reflected by the presence of two distinguished $T_{1H}$ decay times observed via the PMMA and PDXL carbon resonances. Due to phase separation, the $T_{1H}$ decay time of the constituting blend components becomes dependent on the spectral density of molecular motions J(ω) in the MHz range and the average proton environment in the separated domains.[20] The presence of large molecular domains in these blends results in the deviation of both $T_{1\rho H}$ decay times of PDXL (1.6 and 6.8 ms) from the one (9.0 ms) observed for PMMA. Therefore the three $T_{1\rho H}$ decay times have to originate from other phases than those described for the networks and for the blend 20/80; i.e. $T_{1\rho H}^{L}$ and $T_{1\rho H}^{S}$ no longer correspond to the fractions of the mobile and immobilised chains of the PDXL amorphous domains, respectively. Both PDXL decay times can be assigned in accordance with a previous study on linear PDXL and PDXL networks.[21]

A solid state NMR study was performed on the multiphase behaviour of linear and cross-linked (networks) PDXL.[21] Three regions with increasing molecular mobility could be investigated separately for the networks by means of a $T_{1\rho H}$ study. The regions were designated as follows: a crystalline phase, an interphase with limited molecular mobility and an elastomeric phase. For the linear PDXL, the existence of a third phase could not be demonstrated. Linear polymers allow a better organisation of the polymer chains and hence lead to a higher fraction of the crystalline phase. The mobility of the non-crystallised fraction is strongly reduced and only one other $T_{1\rho H}$, in the range of the value for the interphase of the networks, was obtained. The $T_{1\rho H}$ decay time for the elastomeric phase was 5.7 ms while 0.9 ms was observed for the crystalline PDXL domains.

The more heterogeneous phase morphology is also reflected in the results of the thermal analysis.

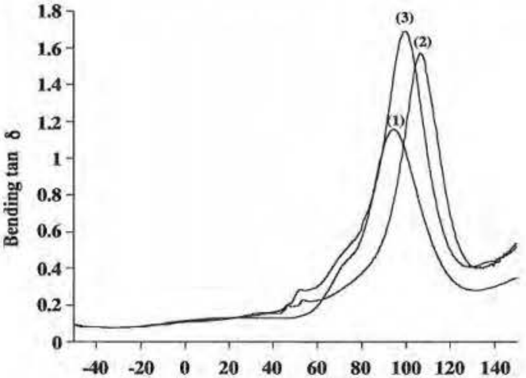

*Figure 3.6: DMA curves of the different PDXL/PMMA blends: (1) blend 20/80; (2) blend 40/60; (3) blend 60/40.*

The DMA curves of the blends 40/60 and 60/40 show two transitions, a major one at about 100-110°C of the PMMA-rich domains and a minor one at about -10°C of the PDXL- rich domains (Figure 3.6). It has been confirmed by DSC analysis that the small transitions at about 50°C are to be ascribed to the melting process of crystalline PDXL domains. On the contrary, these crystalline domains are completely absent in the blend 20/80. The more extensive mixing of the two components in this blend, as compared to blends with higher PDXL fractions, is further demonstrated by DMA. In the DMA analysis (curve 1), the major transition has the highest inward temperature shift when compared to that of the other blends, i.e. the PMMA-rich domains are better mixed up with the PDXL segments.

The presence of small crystalline PDXL domains in the PDXL phase, as demonstrated by DSC, and found in the previous study, should also be reflected in the $T_{1\rho H}$ decay times of these blends. Consequently, the $T_{1\rho H}^{L}$ (6.8 ms) and $T_{1\rho H}^{S}$ (1.6 ms) can be ascribed to the mobile, elastomeric and rigid crystalline PDXL domains, respectively. This assignment is further confirmed by the results obtained at a weaker spin-lock field (25 kHz) which show that the molecular motions of the PDXL chains become independent of those of PMMA. At this spin-lock field, a similar $T_{1\rho H}^{L}$ value is observed meaning that this decay time is situated at the short $\tau_c$ side of the correlation diagram. The PMMA $T_{1\rho H}$ decay time decreases from 9 ms to 4 ms upon decreasing the strength of the spin lock field and is situated at the long $\tau_c$ side of the correlation diagram because of the reduced molecular mobility of the PMMA-phase as compared to the phase separated PDXL.

## 3.3 Conclusions

Solid state $^{13}C$ CP/MAS NMR and thermal analysis were applied for the comparative investigation of the multiphase behaviour of PDXL/PMMA segmented networks and blends. Analysis of the proton spin-lattice relaxation decay ($T_{1H}$) indicates homogeneous phase morphology on a scale of 20 nm for the segmented networks. On the other hand, a heterogeneous phase morphology has been detected on a scale of 1 to 2 nm by means of proton spin-lock relaxation time measurements ($T_{1\rho H}$). For the small phase separated amorphous PDXL domains, two decay times are observed, the short $T_{1\rho H}{}^{S}$ decay time is assigned to amorphous PDXL chains while the long $T_{1\rho H}{}^{L}$ decay time, being similar to the one observed for the PMMA resonances due to efficient spin diffusion, can be assigned to the amorphous PDXL chains that are constrained by chemical cross-links and entanglements with rigid PMMA chains. The forced compatibility of the network components on a scale of 20 nm, which prevents the crystallisation of PDXL chains, is confirmed by DSC and DMA analysis. The decrease in compatibility of both network components with increasing weight fraction of PDXL is reflected by a more obvious two step degradation in the TGA curves.

For the blend 20/80, a similar compatibility behaviour is observed as for the networks: homogeneously mixed on a more microscopic scale ($T_{1H}$) but phase separated on the nanometer level ($T_{1\rho H}$). An increase of the PDXL weight fraction in the blends results in phase separated molecular domains having a dimension of at least 20 nm. In these blends (40/60 and 60/40) the phase separated PDXL is able to crystallise as is demonstrated by DSC analysis and $T_{1\rho H}$ relaxometry.

This detailed comparative phase behaviour study clearly demonstrated the forced compatibility of both components in this unique type of segmented network architecture. The presence of their nano-structured morphology, which is the key to high-tech applications, has been confirmed.

## 3.4 Experimental part

### 3.4.1 Material preparation

A short overview of the preparation of the PDXL/PMMA segmented networks and the analogue polymer blends will be described below in order to obtain an insight in the construction of the studied materials. The synthesis is performed at the Laboratory of Polymer Research, details of the synthesis of the bis-macromonomers (α,ω-diacrylate-PDXL and α,ω-dihydroxy-PDXL, for the networks and the blends, respectively) can be found in literature.[1,7,8,22,23,24] For the segmented networks, more detailed information about the synthesis, soluble fractions and swelling behaviour is described by Du Prez et al.[13]

For this work, $\alpha,\omega$-diacrylate- and $\alpha,\omega$-dihydroxy-PDXL with a number average molecular weight of about 4000 and an acrylate or hydroxyl functionality close to two have been prepared (characterised by GPC and NMR).

The general procedure for the synthesis of segmented networks consists of a free radical copolymerisation of the prescribed bis-macromonomer with vinyl monomers in the presence of a radical thermal initiator.[24] A certain amount of MMA and of $\alpha,\omega$-diacrylate-PDXL, according to the desired weight ratio, are mixed vigorously with 1 wt % benzoylperoxide BPO (relative to vinyl monomer) at 50°C for 3 minutes. For the synthesis of the networks with a high content of PDXL (60 wt %), a minimal amount of toluene is added to obtain a homogeneous and less viscous reaction mixture. The viscous solution was degassed for a few seconds before transferring it, by means of a syringe, between two glass plates that are kept at the desired distance (ultimate film thickness) by a silicone rubber spacer. Before use, the glass plates were treated with $H_2SO_4$ (95%) and with a solution (10%) of trimethylsilyl chloride in toluene to facilitate the recovery of the film after preparation. The glass plate mould containing the solution was kept in an oven for 80 minutes at 60°C, 3 hours at 80°C and 12 hours at 110°C. All films were subjected to a heat treatment for 12 hours in a vacuum oven at 100°C. A piece of each film was treated in a soxhlet apparatus with boiling ethanol for 12 hours. Only films with an extractable fraction of less than 5 wt % have been retained for further characterisation. The low extractable fractions indicate an almost complete copolymerisation between MMA and the bis-macromonomer.

The PDXL/PMMA polymer blends have been prepared by the same procedure. Instead, $\alpha,\omega$-dihydroxy-PDXL ($M_n$ = 3950 g/mol) has been mixed in the desired weight ratio with MMA and 1 wt % BPO. The hydroxyl end-groups of this telechelic polymer allow for the in situ preparation of polymer blends, as they do not interfere with the PMMA formation.

### 3.4.2 Thermal analysis

Values of E', E" and tan δ were measured in the dual cantilever mode by a TA Instruments DMA 2980 apparatus on rectangular films of 1mm thickness at a heating rate of 2 °C/min and at a frequency of 1 Hz. Thermogravimetrical analysis was performed with a Polymer Laboratories TGA, type PL-TG 1000 under $N_2$ atmosphere and heating rate of 10 °C/min.

DSC's were recorded on a Perkin Elmer 7 with thermal analysis controller TAC 7/DX. After keeping the samples at 110 °C in the DSC apparatus, the temperature was decreased to –20 °C (crystallisation temperature of PDXL) and held there during 15 min. Then, the samples were quenched (-90°C) and finally heated at a rate of 10 °C/min.

### 3.4.3 Solid state NMR

*Pulse sequences*

To determine the proton spin-lattice relaxation time, $T_{1H}$, the inversion recovery method has been used. The pulse sequence is shown in Figure 3.7. $T_{1H}$ relaxation times are determined indirectly via the carbon resonances by means of the CP/MAS experiment.[25]

The pulse sequence starts with a $180^{\circ}_{x'}$ pulse with a $B_1$ rf field in the rotating frame of the protons which rotates the proton magnetisation vector from the positive z-direction into the negative z-direction (Figure 3.7a-b). Due to the spin-lattice relaxation in the external field $B_0$ the evolution of the proton magnetisation is as follows: first it decreases, becomes zero and further increases in the positive z-direction, back to its internal equilibrium. After a variable time t the proton magnetisation, is rotated in the y'-direction by a $90^\circ_{x'}$ pulse (Figure 3.7d-e). The carbons are brought in contact with the proton spin system by cross polarisation and the proton magnetisation is transferred to the carbon spin system (Figure 3.7f-h). After a suitable fixed cross polarisation time or contact time, $T_{CT}$, the carbon FID is acquired under high-power proton decoupling conditions.

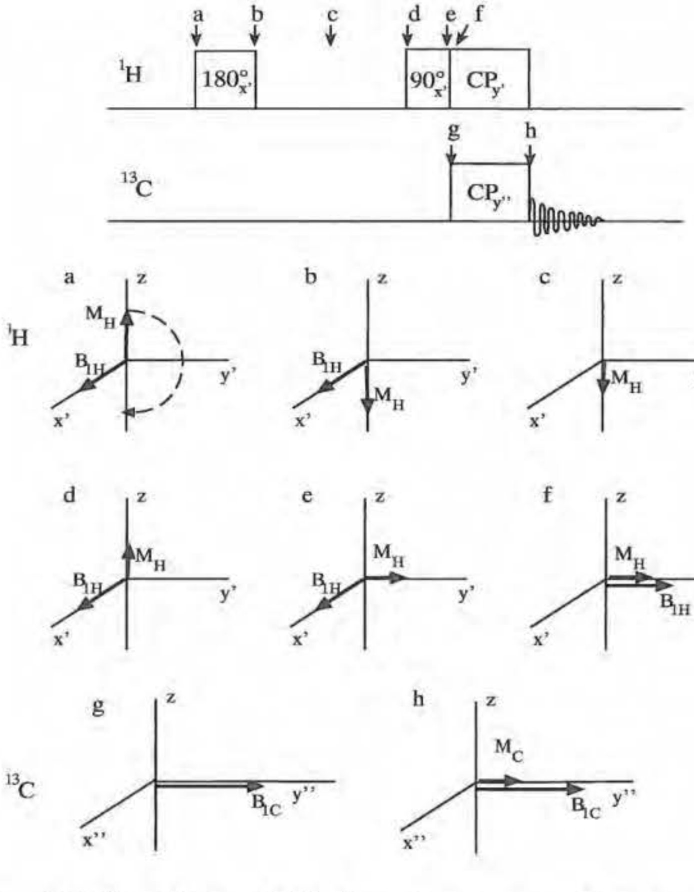

*Figure 3.7: The solid state CP/MAS inversion recovery pulse sequence.*

During the variable time t the proton magnetisation relaxes exponentially according to the spin-lattice relaxation time $T_{1H}$ which can be determined by fitting the evolution of the magnetisation as a function of the variable time t with equation 3.1.

$$M(t) = M_{\infty} - (M_{\infty} - M_0) x \exp(-\frac{t}{T_1}) \tag{3.1}$$

The inversion recovery experiment can be summarised as a ( $180^{\circ}_{x'}$ - t - $90^{\circ}_{x'}$)$_n$ pulse sequence with a repetition time between two pulses of 5 times the longest $T_{1H}$ value.

The $T_{1\rho H}$ or the spin lock pulse sequence is shown in Figure 3.8.[26] Also here, the $T_{1\rho H}$ time constants are determined indirectly via the carbon resonances by means of the CP/MAS experiment.[25]

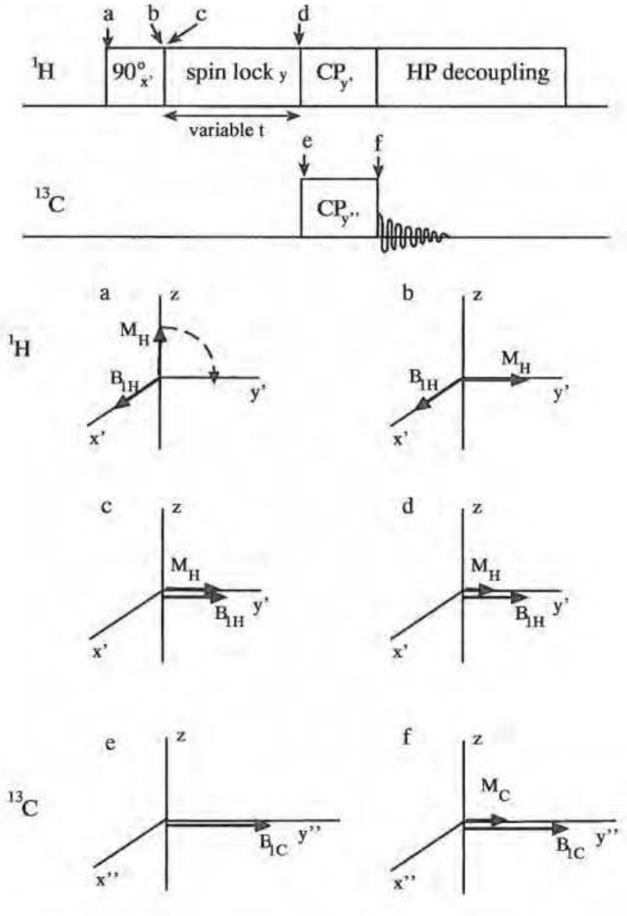

*Figure 3.8: The schematic representation of the $T_{1\rho H}$ pulse sequence.*

The pulse sequence starts with a rf field $B_1$ in the rotating frame of the protons which rotates the proton magnetisation vector $M_H$ in the y'z-plane (Figure 3.8a-b). After the 90° pulse the rf field $B_1$ is phase shifted 90° in the direction of the magnetisation vector $M_H$ (Figure 3.8c) and the protons are spin locked during a variable time t. During this spin lock time the initial proton magnetisation $M_H$ decreases exponential with a time constant $T_{1\rho H}$ (Figure 3.8c-d). After the variable time t the carbons are brought into contact with the protons during the cross polarisation time. The proton magnetisation is transferred to the carbon spin system (Figure 3.8e-f). Afterwards the carbon signal is detected under high-power proton decoupling conditions. The amount of carbon magnetisation that is detected is determined by the duration of the spin lock field i.e. by the duration of the variable spin lock time and the fixed cross polarisation time. The magnetisation as a function of the variable spin lock time t can be fitted to an exponential decay:

$$M(t) = \sum M_0^i x \exp(-\frac{CT + t}{T_{1\rho H}^i}) \qquad (3.2)$$

In this equation, M(t) is the overall magnetisation as a function of the variable evolution time t and CT is the fixed cross polarisation contact time. $M_0^i$ and $T_{1\rho H}^i$ refer to the fraction (%) and time constant, respectively, of the different phase separated domains.

All non-linear least-square analyses of relaxation data have been performed on a Macintosh computer using the program KaleidaGraph 3.0.

*Parameters*

Solid state $^{13}C$ CP/MAS NMR spectra were recorded at room temperature on an Inova 400 Varian spectrometer operating at a static magnetic field of 9.4 T. Magic angle spinning was performed at 6.0 kHz, making use of ceramic $Si_3N_4$ rotors. The aromatic signal of hexamethylbenzene was used to determine the Hartmann-Hahn condition ($\omega_{1H} = \gamma_H\, \beta_{1H} = \gamma_C\, \beta_{1C} = \omega_{1C}$) for cross polarisation and to calibrate the carbon chemical shift scale (132.1 ppm). Other spectral parameters used were a 90° pulse length of 5.0 μs, a spectral width of 50 kHz, an acquisition time of 35 ms, a recycle delay of 4.2 s and 1250 repetitions. High power decoupling was set to 65 kHz during the acquisition time. The proton spin-lattice ($T_{1H}$) and spin-lattice relaxation time in the rotating frame

($T_{1\rho H}$) were measured via the carbon nuclei by means of a multipurpose pulse sequence[27] in which a fixed contact time of 800 μs was used for cross polarisation. The spin lock field was set to 50 kHz. A preparation delay of five times the longest $T_{1H}$ value has been respected for the determination of the $T_{1\rho H}$ relaxation times.

## 3.5 References

1 Adriaensens, P.; Storme, L.; Carleer, R.; Gelan, J.; Du Prez, F. E. 'Comparative morphological study of poly(dioxalane)/poly(methyl methacrylate) segmented networks and blends by $^{13}$C solid state NMR and thermal analysis' Submitted to Macromolecules september 2001.

2 Scott, R.L. *J. Chem. Phys.* **1949**, 17, 279.

3 Barrett, L.W.; Sperling, L.H. *Trends Polym. Sci.* **1993**, 1, 45.

4 Eastmond, G.C.; Smith, E.G. *Polymer* **1976**, 17, 367.

5 Liu, J.; Liu, W.; Zhou, H.; Hou, C.; Ni, S. *Polymer* **1991**, 32, 1361.

6 Meier, W. *Macromolecules* **1998**, 31, 2212.

7 Goethals, E.J.; De Clercq, R.R.; De Clercq, H.C.; Hartmann, P.J. *Makromol. Chem., Macromol. Symp.* **1991**, 47, 151.

8 De Clercq, R.R.; Goethals, E.J. *Macromolecules* **1992**, 25, 1109.

9 Weber, M.; Stadler, R. *Polymer* **1988**, 29, 1071.

10 Tezuka, Y.; Shida, T.; Shiomi, T. Imai, K.; Goethals, E.J. *Macromolecules* **1993**, 26, 575.

11 Du Prez, F.E.; Goethals, E.J. in *Ionic Polymerizations and Related Processes,* Ed. Puskas, J.E. NATO Sciene Series, Series E, Vol. 359, Kluwer Academic Publishers, the Netherlands, 1999, 75-98.

12 Du Prez, F.E.; Christova, D.; Goethals, E.J. *Wiley Polymer Networks Group Review Vol. 2, Chapter 22* Ed. B.T. Stokke and A. Elgsaeter, John Wiley & Sons Ltd. (1999).

13 Du Prez, F.E.; Goethals, E.J.; Schué, R.; Qariouh, H., Schué, F. *Polymer Int.* **1998**, 46, 117.

14 Scherble, J.; Thomann, R.; Ivan, B.; Mülhaupt, R. *J. Polym. Sci. Pölym. Phys. PartB* **2001**, 39, 1429.

15 Reyntjens, W.; Joncheere, L.; Goethals, E.J.; Du Prez, F.E. *Macromol. Symp.* **2001**, 164, 293.

16 Fedotov, V.D.; Schneider, H. *Structure and dynamics of bulk polymers by NMR-methods* Springer-Verlag, Berlin (1989).

17 Douglas, D.C.; Jones, G.P. *J. Chem. Phys.* **1966**, 45, 956.

18 Fox, T.G. *Bull. Am. Phys. Soc.* **1956**, 1, 123.

19 Harris, R.K. *Nuclear Magnetic Resonance Spectroscopy, A Physochemical View,* Pitman Publishing Inc. (1983).

20 Sanders, J. K.M.; Hunter, B.K. *Modern NMR spectroscopy,* Oxford University Press (1987).

21 Du Prez, F.E.; Goethals, E.J.; Adriaensens, P.J.; Gelan, J.M.; Vanderzande, D.J.M. *Macromolecules* **1996,** 29, 4000.

22 Franta, E.; Kubisa, P.; Refai, J.; Ould Kada, S.; Reibel, L. *Makromol. Chem., Macromol. Symp.* **1988,** 13/14, 127.

23 Franta, E.; Gérard, E.; Gnanou, Y.; Reibel, L.; Rempp, P. *Makromol. Chem.* **1990,** 191, 1689.

24 Du Prez, F.; Goethals, E.J. *Macromol. Chem. Phys.* **1995,** 196, 903.

25 Komoroski, R. A. *High resolution NMR spectroscopy of synthetic polymers in bulk.;* VCH; Florida, 1986.

26 Aufla, R.S.; Harris, R.R.; Packer, K.J.; Parameswaran, M.; Say, B.J.; Bunn, A.; Cudly, M.E.A. *Polym. Bull.* **1982,** 8, 253.

27 Hoogmartens, I.; Adriaensens, P.; Vanderzande, D.; Gelan, J. *J. Anal. Chim. Acta* **1993**, 283,1025.

# 4 NMR relaxometry applied in MRI Materials under load

## 4.1 Introduction

Rubber-toughened plastics constitute a commercially important class of polymers, in which the mechanical properties of fracture resistance and stiffness are highly important. Each of these materials is a composite polymer, consisting of a rigid matrix and a dispersed rubbery phase. Toughness enhancement of polymeric systems has been and still is a major task in industrial laboratories of raw material manufacturers worldwide. Despite the many attempts to fundamentally understand the deformation and fracture behaviour of the generally heterogeneous polymeric systems involved, toughness enhancement in practice almost exclusively progresses along empirical routes. Progress in the field of mechanical properties of polymeric systems almost automatically implies the need for extensive experimental testing of newly developed systems on all the different length scales present (either at experimental or at application level).

A fundamental and still unsolved question concerns how the deformation on a micro-scale influences the macroscopic response. In this part of the thesis a better understanding of the deformation behaviour on the macroscopic scale is obtained from a molecular point of view on the deformation of the rubbery phase under critical load by NMR imaging.

### 4.1.1 Fracture behaviour

#### 4.1.1.1 Tough versus brittle

The use of polymer glasses to make structural components has increased significantly over the last 30 years but is still limited by the tendency of these materials to fail. Polymers often fail, usually by fracture, from the mechanical stresses that they are subjected to.

The fracture behaviour of polymers is described by two main deformation mechanisms. If permanent or plastic deformation sets in after elastic deformation at some critical stress, the material is called 'tough' (or ductile). If the material fails and ruptures at a certain tension and only a small elongation is observed, it is called 'brittle' (Figure 4.1).

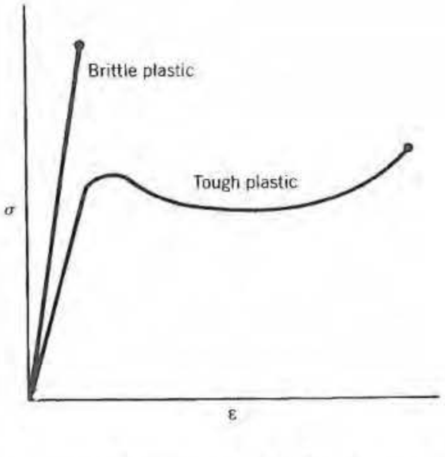

*Figure 4.1: Stress-strain behaviour of a brittle and a tough type of plastic.*

In ductile materials the main deformation mechanism due to the applied stress is shear deformation (shear yielding), involving molecular slip (Figure 4.2a).[1] The whole specimen yields by shear deformation either homogeneously or heterogeneously (localised). In the latter case localised shear deformation is obtained which gives rise to shear bands. Shear bands may be seen as birefringent entities, no void space is produced. During the plastic deformation, there is generally an increase in stress with deformation due to orientation. This process is known as hardening.

In brittle materials, subjected to tensile stresses, the deformation mechanism is initiated by crazes. Crazing is a form of non-catastrophic failure giving rise to irreversible deformation. It involves orientation of molecular chain segments in the direction of the principal stress (Figure 4.2b). These oriented segments are designated as microfibrils.[2,3,4] On further deformation, microvoids are formed between the microfibrils. Consequently the volume of the specimen is increased upon crazing (dilatation). These crazes are load bearing because their two surfaces are bridged by small fibrils even though the volume fraction of fibrils in the craze is typically less than 0.5.[5] The diameters of the fibrils are typical in the range of 5 to 30 nm.[6,7]

*Figure 4.2: Schematic comparison of the deformation processes in crazes (a) and shear bands (a').*

True cracks are formed by breakdown of the fibril structure within a craze. This leads to rapid crack growth and ultimate failure of the sample.

It seems reasonable to assume that crazing is a process which can occur quite naturally in any orientation hardening material, which exhibits plastic instability at moderate strains and in which the yield stress is much higher than the stress required for the nucleation of crazes. Under conditions conductive to brittle fracture, such as the presence of notches, alternating stresses and aggressive environmental media, crazes act as preferred low energy paths for crack propagation. Hence to control crack nucleation one must stop craze formation or make it more difficult relative to shear deformation.

Nevertheless under certain conditions crazing can be beneficial. Crazing is a process of plastic deformation and as such is the most important source of fracture toughness in polymer glasses which deform by crazing rather than shear. In a plastic the energy absorption due to the creation of crazes ahead of the growing crack appears as the major contribution to the toughness. By arranging that very high densities of crazes nucleate and grow, e.g. from small rubber particles, substantial macroscopic plastic strains can be achieved before these crazes break down to form cracks,.

To understand these sometimes contradictory effects of crazing on fracture and toughening properties a lot of experimental and theoretical work has been devoted to gain information about the crazes themselves.

#### 4.1.1.2 Craze initiation, growth and breakdown

Early in the study of crazing,[8,9] from the work of Argon and Hannoosh it was recognised that there was usually a time delay between the application of stress and the visual appearance of crazes. This delay time is evidence of a barrier to craze nucleation. Craze nucleation may occur at stress concentration sites such as surface flaws or local highly molecular orientations at the surface or in the interior of samples at the surface of second phase particles, e.g. dust particles, fillers or rubber particles. The production of small highly perfect samples of polystyrene (PS) from moulding single pellets requires stress for craze initiation substantially higher than for the normal specimen and in several instances in fact these samples underwent shear yielding before crazing.[9]

Several microscopic steps involved in craze nucleation were investigated. Regions which have locally deformed, but not crazed, have been observed by Wellinghoff and Baer[10] prior to crazing, using transmission electron microscopy (TEM) replicas of gold decorated films stretched on poly(ethylene terephthalate) (PET) substrates. Incompletely fibrillated plastically deformed zones near craze initiation sites in PS and other polymer films using TEM are frequently observed.[6] Further along the length of these deformed zones, they turn into crazes. Other microscopic models for craze initiation were proposed each postulating different critical steps.[11,12] The sensitivity of this process to the nature of the flaw structure of the surface makes a detailed comparison of data between different research groups or between experiment and theory very difficult.

Concerning craze growth, there are two main topics that have to be considered, namely the mechanism of craze tip advance and the craze thickening mechanism. Crazes in isotropic materials grow at right angle to the principal tensile stress and only propagate if the stress at their tip exceeds a certain value.

A number of authors have proposed that craze tip advance occurs by repeated void nucleation and expansion, which becomes interconnected, leading to the fibril structure of a craze.[12,13] One problem concerning this postulated theory was to explain how the void phase became interconnected while the craze was still so thin. A more widely accepted hypothesis is that the craze tip breaks up into a series of void fingers by the Taylor meniscus instability (Figure 4.3).[14,15,16] Such instabilities are commonly observed when two flat plates with a layer of liquid between them are forced apart or when adhesive tape is peeled from a solid substrate. The hypothesis in the case of a craze is that a wedge-shaped zone of plastically deformed and strain softened polymer is formed ahead of the craze tip.

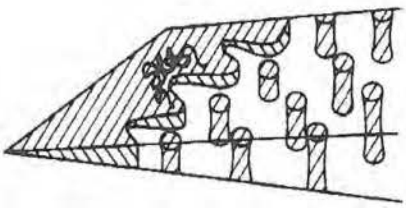

*Figure 4.3: Schematic drawing of craze tip advance by the meniscus instability mechanism.*

Stereo-TEM of craze tips has shown that the meniscus instability is the operative craze tip advance mechanism in a wide variety of glassy polymers.[17]

The craze thickening might occur by two rather different mechanisms. The first proposed mechanism is that, once fibrils are created, they extend in length by creep with no new polymer being drawn into the fibrils at the craze surfaces. As a consequence, weak fibrils are produced with a dramatically rising true stress. This model has been used as a reason for the supposed limiting craze length in rubber toughened plastics[18] and to model the kinetics of craze growth.[19] Links between the creep response of a material and its stress crack performance are studied extensively.[20,21,22,23] The second proposed mechanism of craze thickening during growth is described by drawing in fresh material from the craze-bulk interface.[5,24] Different studies have examined the thickening mechanism and made clear that the last mechanism is the dominant one.[5,24,25] It should be mentioned that an extrapolation of these results can not be exceeded for all kind of crazes (e.g. environmental crazes[26,27,28,29] or crazes undergoing fatigue loading.[30]

In the case that craze thickening should occur by mid-rib creep, one would expect to see that voids nucleate most frequently in the mid-rib, the oldest portion of the craze. Morphological observations by Yang et al. show that fibril breakdowns initiate at the craze-bulk interface together with entanglement loss.[6,31,32] Brown[33] proposed a model that describes the failure of glassy polymers in the crazing regime, based on TEM micrographs which show the existence of short fibrils running between the main fibrils. Earlier theories model these craze fibrils as straight parallel cylinders.[34] The observed crosstie fibrils give the craze some small lateral load bearing capacity so that they can transfer stress between the main fibrils. Analytical models are based on this approach.[35,36,37]

### 4.1.2 Rubber toughening

Many glassy polymers are brittle, which is clearly unwanted for structure applications. The toughening of brittle plastics by the incorporation of heterogeneities has been known for several decades and has been practised industrially on a large scale.

A preferable way to obtain the greatest overall toughness in a plastic is by combining shear yielding, crazing and cracking in the proper order to absorb the highest total energy. Usually, it is desirable to have the sample yield in shear first. This absorbs energy without serious damage to the plastic. Then crazes should be encouraged to form within the shear-banded areas. The shear bands tend to limit the propagation of the crazes. Only lastly do 'molecular engineers' want an open crack to form, because its propagation leads to failure. Microstructural adaptations in polymeric systems are often used for the enhancement of mechanical properties. Especially toughness and impact resistance of glassy and semi-crystalline polymers can drastically be improved by the addition of a fine dispersion of low modulus rubber particles.[1]

Some materials have been toughened by addition of rigid fillers to avoid the loss of inherent stiffness and strength of the thermosets.[38,39,40] Undoubtedly the best results for industrial use on a large scale are obtained by the addition of rubber particles.

Research was mainly focussed on the characteristics of the dispersed elastomeric phase in order to obtain the most favourable failure mechanisms. Many variables influence the degree of achieved toughening and a diversity of opinion exists about the underlying mechanisms.

#### 4.1.2.1 Deformation mechanism

Although it is well known that brittle materials can be toughened remarkable by the addition of a rubbery phase, a great deal of controversy during the whole history of these materials and up till now exists on the nature of the toughening mechanisms. Much of the dispute surrounds the issues of whether the rubber or the matrix absorbs most of the energy, and whether the matrix undergoes massive crazing or simple voiding. It is a prerequisite that the mechanisms resulting in the increased toughness are clearly identified, in order to be able to enhance or modify the material parameters, responsible for these mechanisms and as such to produce an optimal combination of properties.

Several principal mechanisms have been proposed to account for the toughness, for all kind of materials, which are briefly reviewed below.

Originally, it was believed that the toughening of polymers resulted from absorption of energy by the rubber particles themselves. This idea was first advanced by Merz, Claver and Baer (1956)[41] who thought that because the rubber particles were capable of greater elongation than the matrix, they actually held the fracture surfaces of the crack together. The increase of impact energy absorption was attributed to the energy required to stretch out the rubber particles. Schmitt and Keskkula[42] were the first to observe that the rubber particles served as stress concentrators for the production of large numbers of what were then thought to be cracks. Later (1965), Newmann and Strella[43] showed that the model of Merz et al. was incorrect. It was demonstrated that the matrix absorbed more energy than the rubber particles, and proposed that the rubber particles in fact triggered yielding in the matrix. The idea that toughening in polymers is enhanced by local deformation in the matrix was thus founded. All of the rubber modified glassy polymers showed a marked increase in whiteness or opacity - so called stress-whitening - produced by impact loading. Kambour[44] and Bucknall and Smith[45] associate this stress whitening that occurs in a strained polymer with crazing. The large amount of 'bands' formed at right angles to the direction of applied stress, were found to contain birefringent polymer of a lower average refractive index than the surrounding bulk polymer.[46] The association of stress-whitening with crazes gave rise to the theory of massive crazing which is based on the idea that energy is dissipated through the formation of many small crazes rather than one large crack. Matsuo[47] subsequently confirmed by electron microscopy that the stress whitening in acrylonitrile butadiene styrene (ABS) and high impact polystyrene (HIPS) arose from crazes, which initiate and terminate at the rubber particles (Figure 4.4).

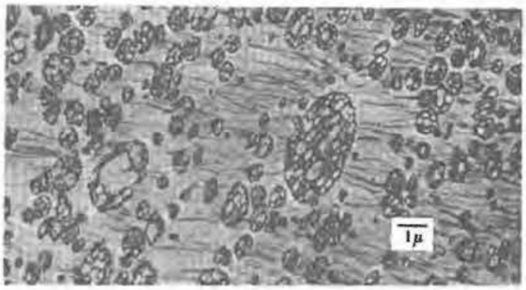

*Figure 4.4: Transmission electron micrograph of ultrasection of high impact polystyrene deformed to small strain and stained with osmium tetraoxide. Crazes and rubber both stain. Reproduced of R.P. Kambour*[48]

Kambour concluded that the rubber particles appear to act with a double function.[48] The first is to concentrate stress and cause craze initiation at the rubber/matrix interface and the second role of the rubber particles is the retardation of small cracks in their growth to catastrophic lengths ('crack stoppers').

Bucknall and co-workers[18] proposed that massive crazing and shear flow are the two energy-absorbing mechanisms in rubber-modified plastics. They used tensile creep dilatometry to study these mechanisms in rubber-modified epoxies.[49,50,51,52,53] In their analysis, they assume that shear flow creates no volume change, whereas crazing does; therefore, the slope of the volume strain $\Delta V/V_0$ against longitudinal strain $\varepsilon_1$ curve equals zero for a pure shear-flow process, and equals unity for a pure crazing process. Intermediate slopes would be produced by proportionate mixing of the two processes. However, other workers have found that volume dilatation cannot be unambiguously and exclusively attributed to crazing; voiding can also cause volume dilatation.[54,55] Breuer already concluded in 1977 that stress-whitening in rubber-modified poly(vinyl chloride) (PVC) is caused by the formation of cavities in the rubber particles; this cavities are aligned in bands. The mechanistic connection between stress whitening and shear yielding was confirmed by investigation of the stress-whitened zone in ABS polymers showing extensive cavitation of the rubber particles. In a more general way: rupture of rubber particles and formation of voids may be rather general processes during shear deformation of polymers. Bascom and co-workers proposed that cavitation increases the size of the plastic zone and that the plastic zone sizes are directly related to the toughness.[56,57,58] The notion that cavitation and shear yielding of the epoxy matrix are the energy dissipating mechanisms producing the toughening effect, is supported by Kinloch et al.[59,60] The distribution of the stress which means that a stress field develops around each individual rubber particle, has been proposed as a toughening mechanism by Yee et al.[61,62] As the stress builds during the deformation the stress fields may interact with each other. When interaction occurs, the matrix can flow around the particles creating voids. Maxwell concluded that shear banding and voiding are competitive mechanisms in modified polycarbonate (PC).[63] A quantitative model, based on the idea that elastic energy stored in the rubber during stretching is dissipated irreversibly when the particles fail, was advanced by Kunz-Douglass et al. in 1980.[64] This is the only model that attributes the toughness enhancement of rubber-modified epoxies entirely to the rubber particles. This model can account for a factor of two in the fracture toughness, which was the amount found by these authors, although higher increases were found by other authors[49,58] and typical values reported in literature could not be explained. The mechanism of impact energy dissipation in rubber toughened nylon has been determined by an energy balance during notched impact fracture by Wu.[65] Wu found that about 25 % of the impact energy is dissipated by matrix crazing and about 75 % is dissipated as heat by matrix yielding. In 1986 Yee and Pearson concluded that the rubber particles dissipate the bulk strain energy by cavitation and at the same time, the shear-strain energy is allowed to build up to the point where shear yielding can take place. A zone of voids and shear bands is formed ahead of the crack tip. The creation of this plastic zone is the principal toughening mechanism.[66,67]

Taking into account all the studies on rubber toughened plastics, it could be distillated that the increased impact toughness achieved as a result of crazing occurs most often in polymers whose matrices are brittle while shear yielding is a source of toughness found in ductile polymers.

Cavitation of rubber particles was first observed in toughened plastics 20 years ago[54,55,58] and the phenomenon has since been observed in a wide range of rubber-toughened polymers. Pearson and Yee postulated in 1991 that easily cavitating rubber particles promote shear banding, and the majority of toughness is achieved by the dissipation of energy through shear band formation. This has been demonstrated, for example, by Pearson and Yee[68] for rubber-modified epoxies, van der Sanden et al.[69] for PC/core-shell rubber systems and Magalhães and Borggreve for PS-rubber blends.[70] Ramsteiner[71] did not observe crazing during plastic deformation of nylon-rubber blends, but shear yielding in the matrix and voiding inside the rubber particles. These observations for polyamides are confirmed by Borgreve[72] and Muratoglu[73] and in recent years it has been observed in ABS and poly(methyl methacrylate) (PMMA).[74,75,76] Recently, Smit demonstrated that a stable post-yield response is a prerequisite for the distribution of plastic strains over the whole macro- and microstructure.[77] Hence, massive shearing is promoted by the introduction of voids and furthermore, it is shown that the voids reduce the macroscopic dilative stresses to safe values. Possible routes to improve the post-yield behaviour, and thus toughness, are proposed by either elimination of the strain softening or improving the strain hardening.

#### 4.1.2.2 Parameters controlling the toughening effect

In the next issue, the parameters controlling the toughening effect will be discussed in more detail. The influence of the particle size, the amount of rubber and the interparticle distance, the rubber-matrix adhesion and the properties of the rubber will be discussed.

*Particle size effect*

Even early in the study of rubber toughening it was found by McGarry et al.[78,79] that small rubber particles (< 1μm) did not toughen epoxies whereas large (1 to 22 μm) particles increased the fracture toughness by at least an order of magnitude. By the introduction of easily cavitating rubber particles, voids are generated in a controlled manner. However the internal cavitation of rubber particles is difficult if the particles are too small.

Hobbs et al.[80] found that the optimal size appears to depend on the deformation mechanisms involved. The mechanism by which the toughness is enhanced depends on the intrinsic ductility of the matrix material.[81,82] In brittle polymers such as PS the rubber particles promote crazing in the matrix and hence the rubber particles must be larger than about 1 μm[18,83,84] whereas in pseudo ductile polymers such as PC and polyamide (PA) shear yielding is usually the major energy absorbing mechanism and so the particles must be generally smaller than 1 μm.[72,85] Jang[86] postulated that for each type of material, an optimum particle size for toughening exists. In general, the critical particle size for toughening decreases with increasing ductility of the matrix polymer. Wu as well stated that it is recognised that there is an optimal particle size at which the toughness is the greatest but this only for matrices with a brittle fracture mechanism.[85] In blends with a ductile fracture mechanism of the matrix such as PA, it was found that toughness is independent of the particle size. In contrast, Borggreve[72] mentioned that the optimal particle size for rubber particles in a PA matrix must be smaller than 0.32 μm while Oshinski[87] reported that too small particles are not efficient for toughening PA6. Several contributions concerning the critical particle size have been reported.[54,88,89,90,91,92] During the past decade attention has been focussed on the optimisation of the phase morphology. In order to obtain the optimal particle size, functionalised block copolymers were extensively examined.[93,94,95,96] Nylon 6 blended with the functionalised ethylene-propylene rubber (EP rubber) has been studied a lot.[87,97,98,99,100,101,102] An acceptable explanation for the size dependence was given by Bucknall et al.,[103,104,105,106,107] who introduced an energy-balance model to show that the critical cavitation stress and thus cavitation resistance increases with a decreasing particle diameter. This energy-balance model is essentially an extension of Griffith's fracture model: the energy gained by relieving triaxial stresses through cavitation must exceed the energy needed to create new void surface.

There is general agreement that the morphology of the blend or specifically the rubber particle size is an influential factor. Although the contribution of this parameter on the toughening effect may vary widely from one system to another.

### *Amount of rubber and interparticle distance*

Bucknall and Hall[108] experimented how the properties of HIPS were changing when varying the amount of PS into the rubber particles and concluded that an increase of the volume fraction of the dispersed phase tends to raise impact toughness of HIPS. Upon decreasing the particle size, the number of particles increases which results in a decreased interparticle distance and so an improve in toughness as well. The fact that the impact strength in HIPS increases with decreasing particle size may reflect an increased crack stopping efficiency. Wu found that a sharp brittle-tough transition occurs when the average surface-to-surface interparticle distance is smaller than a critical value in nylon/rubber blends.[85] The critical particle size increases with increasing rubber volume fraction, but is uniquely related to the critical surface-to-surface interparticle distance. This critical value is independent of rubber volume fraction and particle size and it is thus proposed that the surface-to-surface interparticle distance is the only parameter determining when a blend will be tough or brittle for pseudo-ductile matrices. In 1988 Wu extended this concept to polymer/rubber blends with brittle matrices.[109] Borgreve et al. showed the interparticle distance model of Wu applicable, although its physical explanation was questioned.[72]

It is obvious that the particle size is correlated with the amount of rubber and the interparticle distance. On the basis of the model of Wu all influential parameters could be reduced to a single factor namely the surface-to-surface interparticle distance.

*Rubber-matrix adhesion*

Bucknall examined the rubber-matrix adhesion concluding that the craze termination fails when the bond between the rubber and the matrix is weak.[18] Instead of stabilising the craze, a weakly bonded rubber particle is pulled away from the matrix, leaving a hole from which the craze can propagate, and from which breakdown of the craze to form a crack is probable.

Wu[85] mentioned that strong adhesion alone does not ensure toughening. The interparticle distance must also be smaller than the critical value to achieve a transition from brittle to tough behaviour. All blends having weak adhesion and a brittle fracture behaviour, have rubber particles with a much larger particle size than the critical size for toughening. Wu stated that the minimum adhesion required, should be to avoid that the rubber particles detach from the matrix during fracture. This minimum adhesion should be equal to the tear energy of the rubber, which can be obtained from van der Waals adhesion alone without chemical bonding for toughening polymers like nylon in which the deformation mode is mainly shear yielding. Borggreve[72,97] did some experimental work on blends of nylon and EPDM-rubber with different levels of interfacial adhesion. The outcome that the interfacial adhesion has no influence on the brittle-tough transition, provided some support to Wu's conclusion that a van der Waals adhesion between the two phases is sufficient for the toughening effect. Jang[86] found that polypropylene can be toughened by physically blending in a rubbery phase without appreciable interfacial bonding.

By using functionalised elastomers, the formation of chemical bonds across the interface during processing gives an improved interfacial adhesion. Changing the interfacial adhesion may have an effect on the blending process and consequently on the size of the dispersed phase, which makes it complicated to study the influence of the adhesion in itself.

Wu concluded that for matrices with a brittle fracture mechanism, the conflicting results on the effect of particle size probably resulted from the fact that the adhesion was not strictly controlled in all cases.

### *Properties of the rubber*

The type of modifier was found to have a strong effect on the impact behaviour of the blend.[98] Oxborough and Bowden[110] calculated the stress concentration factors around low-modulus spheres in a rigid matrix. It was concluded that a decrease of the ratio of the shear modulus of the dispersed phase to the shear modulus of the matrix ($G_d/G_m$) below one-tenth, does not involve a further increase of the stress concentration factor. So all materials with a lower shear modulus have the same impact modifying effect. Bucknall states that cross-linking of the rubber particles is desirable since during impact the rubber phase is subjected to very large tensile strains, giving a craze-like structure. A moderate degree of cross-linking allows the rubber to reach high strains by fibrillation and at the same time confers mechanical strength upon the fibrils. Dao[111] found that a lightly cross-linked EPDM (ethylene propylene diene monomer) rubber is a little bit more effective as impact modifier for polypropylene (PP) than an uncross-linked EPDM. Borggreve[98] examined the mechanical properties of nylon-6 rubber blends with different impact modifiers. It looks that the impact behaviour gradually improves with decreasing modulus of the impact modifier. The function of the rubber particles is to generate voids.[84] The onset of voiding has been observed to be strongly influenced by the type of elastomer used.[99] Particles with a higher modulus, that cavitate before the matrix yields, were observed to result in more shear band formation and thus in a larger plastic zone.[112] Pearson and Bagheri[113] suggested that this could be caused by the larger cavitational resistance of the particles, which allows an increased build-up of strain energy prior to cavitation of the particles. The released energy after cavitation enables the formation of shear bands to proceed in a faster rate and more shear bands can develop before the material crazes or fractures, resulting in a larger plastic zone.

### 4.1.3 Different rubber-toughened materials

#### 4.1.3.1 The invention of toughened polystyrene

The history of rubber toughened plastics can be traced back as far as 1927. In that year, Ostromislensky patented a process for making toughened PS by polymerising a solution of styrene monomer with rubber.[114] This process was not commercially exploited, because the product was found to be cross-linked and therefore impossible to be moulded. The subsequent commercial development of toughened PS has been reviewed by Amos.[115] The availability of cheap styrene monomer led to an expansion of the PS production during the 1940s and revived interest in the rubber-toughening process. With this stimulus, the Dow Chemical Company mounted a research programme which led to the announcement in September 1948 that it was marketing a new, impact-resistant grade of PS. This product was made by dissolving styrene-butadiene rubber (SBR) in a styrene monomer solution and polymerising this (like Ostromislensky's basic invention). A method for breaking down the rubber network, converted the earlier intractable polymer into a mouldable thermoplastic; a commercial success. The research programme was continued with the aim of reducing production costs and improving the surface appearance of toughened PS. In 1952, a new continuous process in which the solution is stirred during the early stages of polymerisation was introduced by Dow. Because of the stirring, the rubber forms discrete particles rather than a continuous network what results in reduced manufacturing costs and improved surface gloss. To this day, most HIPS production is based upon continuous stirring during the early stages of the polymerisation giving a 'salami' type of morphology. A feature of this morphology is the presence within the rubber particles of rigid PS sub-inclusions, which are separated from each other and from the PS matrix by thin membranes of grafted polybutadiene (PB); only small particles are solid rubber particles. The solution-grafted polymers made by Dow were superior to those made by melt blending because of the well-bonded rubber particles with styrene due to the grafts on the rubbery chains. The most significant development after Dow's invention was the replacement of SBR by PB as the standard toughening rubber. Also other rubbers, like poly(phenylene oxide) (PPO) were successfully used as toughening rubbers. Later on, research has been focussed on toughening mechanism,[51,116,117] the internal structure of rubber particles[84] and the particle size effect.[118]

### 4.1.3.2 ABS as the successor to HIPS

The second rubber-toughened plastic to be manufactured commercially was ABS (acrylonitrile-butadiene-styrene polymer), which was launched to the market in 1952 by the US Rubber Company. The first ABS was made by melt blending SAN (styrene-acrylonitrile copolymer) with NBR (acrylonitrile-butadiene copolymer rubber).[119] Todays most important routes to ABS are the emulsion and the bulk-suspension polymerisation.[18] Most modern ABS polymers are based upon PB, although other diene rubbers are used. The use of unsaturated rubbers as toughening agents isn't entirely satisfactory, as they are easily oxidised, especially upon exposure to sunlight. As a result ABS becomes brittle upon ageing. ABS polymers have great market relevance: they are used in a wide variety of applications (from appliances to car industries) because of their good property balance. These materials represent a valuable compromise in mechanical, aesthetic and processing properties. Because of their commercial importance, a lot of research has been performed on the deformation and fracture behaviour of ABS.[95,96,120,121,122,123,124,125] The rubber particle size effect towards cavitation is extensively studied even at this moment.[74,91,126]

### 4.1.3.3 Other rubber toughened materials

*Poly(vinyl chloride) (PVC)*

Unplasticised PVC is a much more ductile polymer than PS and SAN, nevertheless it does exhibit brittle fracture. For this reason, manufacturers of

PVC took an early interest in the rubber-toughening process. In 1957 toughened grades of PVC were produced. PVC-NBR blends are capable of attaining an excellent balance of properties however, inherent to the chemistry of vinyl chloride polymerisation, grafting caused considerable difficulties. Therefore melt blending has remained an important commercial process for toughening PVC. Graft copolymers based on the monomers ABS and MBS (methacrylate-butadiene-styrene) were used to toughen PVC leading to a well-controlled morphology, a high transparency and a good impact strength. These PVC blends are widely used in the packaging field for bottles and films requiring primarily excellent clarity and only relatively short durability.[54,127]

### *Polypropylene (PP)*[69,86,128,129,130]

PP also suffers from brittle fracture problems, especially at room and low temperatures. Rubber-toughened grades of PP became commercially available in 1962, only five years after the homopolymer was first marketed. Two types of rubber toughened PP appear: a blend of PP with ethylene-propylene rubber (EPR) and a more commonly used copolymer of PP with polyethylene. The most important applications are packing films, fibres, crates and pipes.

### *Poly(methyl methacrylate) (PMMA)*

PMMA, like PS, is a brittle, glassy polymer that could obviously benefit from an increase in toughness. However PMMA is a more expensive polymer than PS. Its main applications are in glazing and signs, which require the transparency and resistance to weathering. Unfortunately, addition of rubbers tends to make the polymer both opaque and susceptible to weathering. In the past, a partial solution to the problem was represented by MBS and MABS (methyl methacrylate-acrylonitrile-butadiene-styrene) polymers, which are transparent because the refractive index of the matrix has been matched with that of the rubber by a suitable combination of monomers.[131] In the 1970s transparent polymers based upon acrylate rubbers have been developed and are still used until now.[76,92]

### *Epoxy Resins*

Another class of rubber toughened materials are thermoset resins (epoxies) with the addition of rubber. Most epoxies are extremely brittle. Sultan and McGarry[79] showed that worthwhile improvements could be effected by adding certain liquid rubbers to epoxide formulations. Due to its compatibility with the resin and the reaction with the epoxide group carboxyl-terminated butadiene-acrylonitrile (CTBN) rubber became the most important toughening rubber for epoxies. To a minor extent both amino- and vinyl-terminated butadiene-acrylonitrile (ATBN and VTBN) have also been used to toughen epoxies.[132] More recently, in order to be able to add a larger volume fraction of rubber (above 15-20 %) a liquid diglycidyl ether of bisphenol A has been used to toughen epoxy resins.[66,67,68,133]

*Polyamides (PA)*

Polyamides or nylons are tough engineering resins having high tensile impact strength and elongation values. When water is absorbed, nylons are plasticised and become even tougher. However these toughness values decrease markedly if notches are present. Upon modification with rubbers, the resistance to crack propagation increases. Rubber toughening of nylons was investigated in the 1980's,[80] they are now well established commercially as engineering polymers. The added rubbers must have sufficient resistance to oxidation and be able to withstand the high barrel temperatures used to mould nylons. Ethylene-propylene (EP) copolymers are among the most successful rubbers. The EP rubbers are treated with maleic anhydride to provide reactive sites along the chain, and then melt-blended with nylon. Reactions between terminal amine groups of the nylon and the anhydride groups bonded to the EP rubber chain produce graft copolymers which aid dispersion and enhance interfacial adhesion.[97,109,134,135,136,137]

In addition to the rubber toughened materials that are mentioned above, a number of other polymers were modified successfully with all kind of rubbers.

### 4.1.4 Scope of the work in this thesis

The mechanisms of rubber toughening have been widely examined in recent years and it is evident that the augmented toughness is obtained when the second phase is able to trigger and amplify on a microscopic scale the matrix plastic deformation mechanisms. Despite the useful studies in the past, the understanding of crack growth resistance is incomplete. Mainly due to the small scale on which the near crack tip processes occur and because crack propagation manifests under critical conditions of mechanical load, studies towards an improved insight are difficult to perform. Moreover, most of the

relevant fracture processes occur in the bulk of the material, shielded by surrounding material, limiting the usefulness of conventional microscopes.
Owing to their structure, crazes have a lower density and a lower refractive index than the bulk polymer. Their properties make it possible to measure sizes and shapes using optical interference. However this technique is restricted to materials having some important conditions like 1) transparency of the material, 2) a significant differ of the refractive index between the craze form and that of the bulk and 3) a sharp boundary between the two regions, what reduces the use of this technique to some specific materials. Transmission electron microscopy (TEM) and scanning electron microscopy (SEM) are useful techniques but are limited to the fracture surface or are investigated post-mortem. For example, Riemslag[138,139] studied a craze zone at the crack tip in PE using SEM. Therefore, slices perpendicular to the crack tip were cut out of a stress relaxed plate and SEM pictures were recorded after reloading the slices. Although illustrative, this method is elaborate and still suspect to artefacts, mainly regarding the reloading of the specimen. Another useful technique is thermal contraction/expansion tests, but this technique is limited to changes in volume of the sample. Nevertheless, by this technique Bucknall estimated successfully the volume fraction of rubber particles that have cavitated.[126] Argon Atom Emission has been used as a probe of craze initiation and craze formation.[140] Argon was introduced into the material prior to the experiment and the emission of argon was measured during loading. This procedure is a sensitive indicator of the onset and growth of crazes but is limited for crazes reaching the surface.

NMR imaging offers a possibility to overcome the described limitations. NMR imaging (MRI) is a well-established, non-destructive and non-invasive tool,[141,142] well-suited to study the microscopic spatial dependency of stress induced material response.[143,144,145] As opposed to optical and electron microscopy which only allow to study the material surface or require transparent materials, NMR micro-imaging can be performed slice selective in the bulk of the material. Moreover, material preparation like deuteration for neutron scattering, trimming and staining for TEM or coating with a conductor for SEM is not required. Several MRI techniques were previously used for characterisation of rubbers, semi-crystalline and rigid polymers under deformation.[146,147,148,149] It was shown that the method provides information on strain distribution, the direction of local strain, molecular order, variation in the local mobility, as well as inhomogeneous sample heating under dynamic mechanical load.

Although the spatial resolution of MRI, being about 50 μm or less, is rather low as compared to TEM and SEM[141,142,150] the method provides complementary information because of the large variety of molecular dependent contrast parameters, like the spin density ($M_0$) and the relaxation times $T_{1H}$, $T_{1\rho H}$ and $T_{2H}$, that can be implemented.[144,151,152] These parameters can be related to the amount of material/phases per unit volume and molecular mobility. Quantitative spin density and relaxation time images can be of particular interest for the characterisation of a growing crack and for understanding the deformation mechanism from a molecular point of view.

## 4.2 ABS: Study of the crack growth process

### 4.2.1 Introduction

The dominant property of ABS (acrylonitrile-butadiene-styrene) plastics is the very high impact strength which is coupled with the less desirable feature, namely that of low stiffness and strength for structural use. ABS has the propensity to craze with a large craze zone after mechanical load. Further loading leads to cracking and severe damage bands. The ability to visualise the deformation zone is important for the understanding of crack growth resistance in ABS.

This issue discusses a NMR imaging study of ABS under critical load. MRI investigations were performed on loaded specimens with a crack grown under critical conditions as well as on unloaded specimens. Numerous damage bands appear in the images of strained ABS which converge towards the crack tip and remain present upon unloading. Image contrast is demonstrated to arise from a reduced material density in these damage bands. Obviously severe crazing and rubber particle cavitation occurs at the crack tip.

### 4.2.2 Material characteristics

The ABS type studied is a blend of poly(styrene-*co*-acrylonitrile) (SAN) with 28 wt % polybutadiene (PB). This ABS material consists of a SAN copolymer matrix blended with sub-micron SAN grafted polybutadiene rubber particles.

#### 4.2.2.1 Tensile strength tests

Tensile strength tests were performed in order to obtain the tensile characteristics of this material. The stress-strain curve of specimens with different shapes are presented by measuring the stress at an elongation rate equal to 10 mm/minute (Figure 4.5).

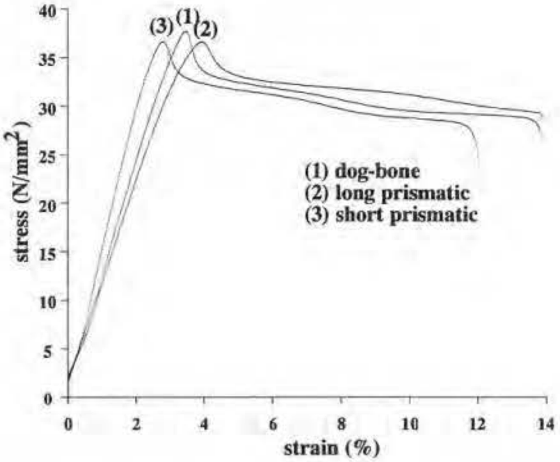

*Figure 4.5: Stress-strain curves of ABS specimen: (1) a dog-bone specimen, (2) a long prismatic specimen, (3) short prismatic specimen drawn at a tensile strength tester at a rate of 10 mm/min.*

As shown, similar stress-strain curves are obtained for a dog-bone shape (150 x 10 x 4 mm), a long prismatic tensile bar (128 x 12.75 x 3.25 mm) and a similar shorter prismatic tensile bar (80 x 10 x 4 mm). All studied specimen yield a stress-strain curve, characterised as a 'ductile cold drawing and reorientation hardening' curve (see part 4.1.1.1). Out of the tensile properties (Table 4.1), only a weak dependence of the stress-strain behaviour on the shape of the specimen can be concluded.

| Mechanical Properties | Dog-bone Shaped Specimen | Long Prismatic Specimen | Short Prismatic Specimen |
|---|---|---|---|
| E-modulus (N/mm$^2$) | 685.50 ± 107.96 | 607.59 ± 64.31 | 729.75 ± 117.50 |
| yield stress (N/mm$^2$) | 39.33 ± 0.33 | 37.11 ± 0.36 | 38.73 ± 0.64 |
| yield strain (%) | 5.23 ± 0.08 | 5.63 ± 0.28 | 4.32 ± 0.09 |
| strain at break (%) | 17.37 ± 1.98 | 19.08 ± 1.38 | 18.85 ± 2.05 |

*Table 4.1: Tensile characteristics of three different shaped specimens of ABS plates as determined at a tensile rate of 10mm/min*

By varying the elongation rate, a behaviour in accordance with the mechanical laws for plastics is observed. As expected, a higher elongation rate results in a higher yield stress but more brittle behaviour while a lower rate (1mm/min) results in a lower strength but more tough (ductile) behaviour.

To study the process of crack growth, a cracked specimen under load is required at the condition of a (very slowly) growing crack, because of the small scale on which the near crack tip fracture processes occur and because crack propagation occurs under critical conditions of mechanical load. To obtain such a condition and to exclude random effects and inhomogeneities caused by polymer engineering, a sharp notch was cut in the plates perpendicular to the strain direction z (Figure 4.6).

To examine the effect of a pre-crack perpendicular to the strain direction, some tensile strength tests were performed on specimen (40 x 12.8 x 3.25 mm) with and without a pre-crack. The pre-crack was cut by a razor blade perpendicular to the thinnest side and was 4 mm in depth.

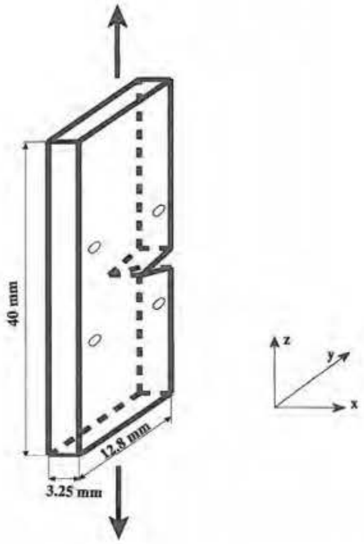

*Figure 4.6: Sample size and its position in the magnet with respect to the $B_0$ field (see later) (z-direction). The notch and the distance markers are indicated. The strain is parallel to the z-direction.*

From the stress-strain measurements an E-modulus of 318.23 ± 9.81 N/mm$^2$ and 303.67 ± 3.99 N/mm$^2$ for the sample with and without a pre-crack, respectively is obtained. The yield stress of both samples is also comparable, namely 29.85 ± 2.41 N/mm$^2$ and 30.01 ± 1.07 N/mm$^2$ for the sample with and without a pre-crack, respectively. These tensile properties confirm that the pre-crack has no influence. Especially the notch does not change the yield stress, being around 30 MPa. The fracture of such small specimens of a tough material occurs by net section yielding.

The lower E-modulus (more tough behaviour), as compared to the results in Table 4.1, is obtained due to the lower elongation rate (1mm/min).

#### 4.2.2.2 Material loading

To enable the study of crack growth under critical conditions of mechanical load, a dedicated stretching device (Figure 4.7) has been developed in our laboratory. This stretching device fits into the NMR probe head and allows us to measure under constant strain.[153]

*Figure 4.7: The stretching device which fits into the NMR probe head.*

All specimen measured under load have a dimension of 40 x 12.8 x 3.25 mm. The specimen was fixed in copper top and bottom clamps by two screws on each clamp. The distance between the screws on each clamp is 5 mm. While the glass tube fixes the bottom piece, the top piece can be pulled up by a screw bar resulting in the elongation of the specimen. The stress induced on the plate can roughly be estimated from the torque used to load the screw bar (Figure 4.8).

*Figure 4.8: The stretching device fixed in the holder to load the specimen by use of the spanner and the torque.*

The effect of the copper parts of the device was examined by making an image of the sample in and out the device. No influence was observed in the image neither on the tuning of the magnet. Distance markers were etched on one side of the plate, about 5 mm above and below the notch (see Figure 4.6). These markers make it possible to measure the average strain as a function of increasing stress.

The loading of the notched specimen is accomplished outside of the NMR magnet. The specimen was elongated up to yield stress. The load was maintained on the specimen during the NMR imaging experiments. Consequently, the crack tip region could be investigated under critical conditions. Furthermore, additional experiments were performed after unloading the specimen.

#### 4.2.2.3 Scanning electron micrographs

Scanning electron micrographs (SEM) of an ABS plate with a pre-crack that was strained to yield stress clearly show damage bands in the deformation zone ahead of the starter crack (Figure 4.9). A crack growth in line of the pre-crack is shown in Figure 4.9a. Figure 4.9b-d show magnifications of the damage zone so that straight damage bands become visualised in more detail.

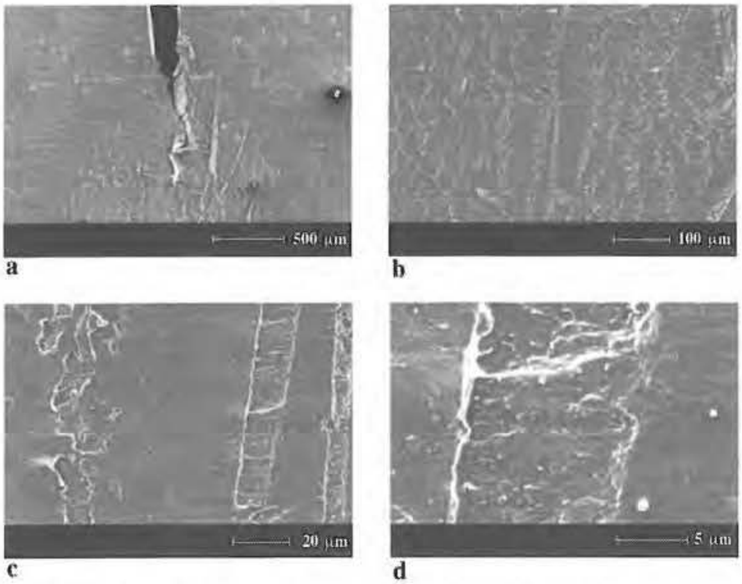

*Figure 4.9: Scanning electron micrographs of the deformation zone ahead of the crack tip of an ABS specimen with pre-crack, strained to yield stress.*

### 4.2.3 Visualisation of stress induced damage bands in ABS by NMR imaging

A reference image of a native ABS plate showing the notch and the distance markers etched at about 5 mm on both sides of the notch is shown in Figure 4.10. Since the transverse magnetisation of the rigid glassy matrix decays to zero within 100 μs, the bi-exponential $T_{2H}$ relaxation behaviour of these materials has been filtered out to a mono-exponential behaviour in our images taken with an echo time of 1.0 - 1.5 ms. The echo time acts as a highly selective $T_{2H}$ relaxation time filter resulting in images that show the strain effect only for the rubbery phase of the specimen.

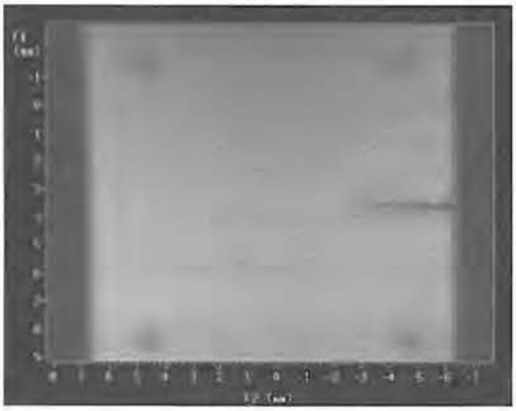

*Figure 4.10: Reference scout image of an ABS plate showing the notch and the distance markers (dark circles).*

#### 4.2.3.1 Optimisation of the MRI acquisition parameters

*Changing the gradient orientation.*
To examine the influence of the gradient orientation and the position of the crack with respect to the main magnetic field $B_0$, images are acquired to visualise the influence of these parameters.

Images with a different gradient orientation, of a piece of ABS (cut out of a prismatic plate of 40 x 12.8 x 3.25 mm) that was stretched beyond the yield point in a tensile strength tester (imaged after unloading) are shown in Figure 4.11a-b. The sample was placed with its pre-crack perpendicular to the $B_0$ field, as in the stretching device. The x-axes (were the sample dimension is 3.25 mm) was in both cases the slice gradient direction (slice thickness = 3.25 mm).

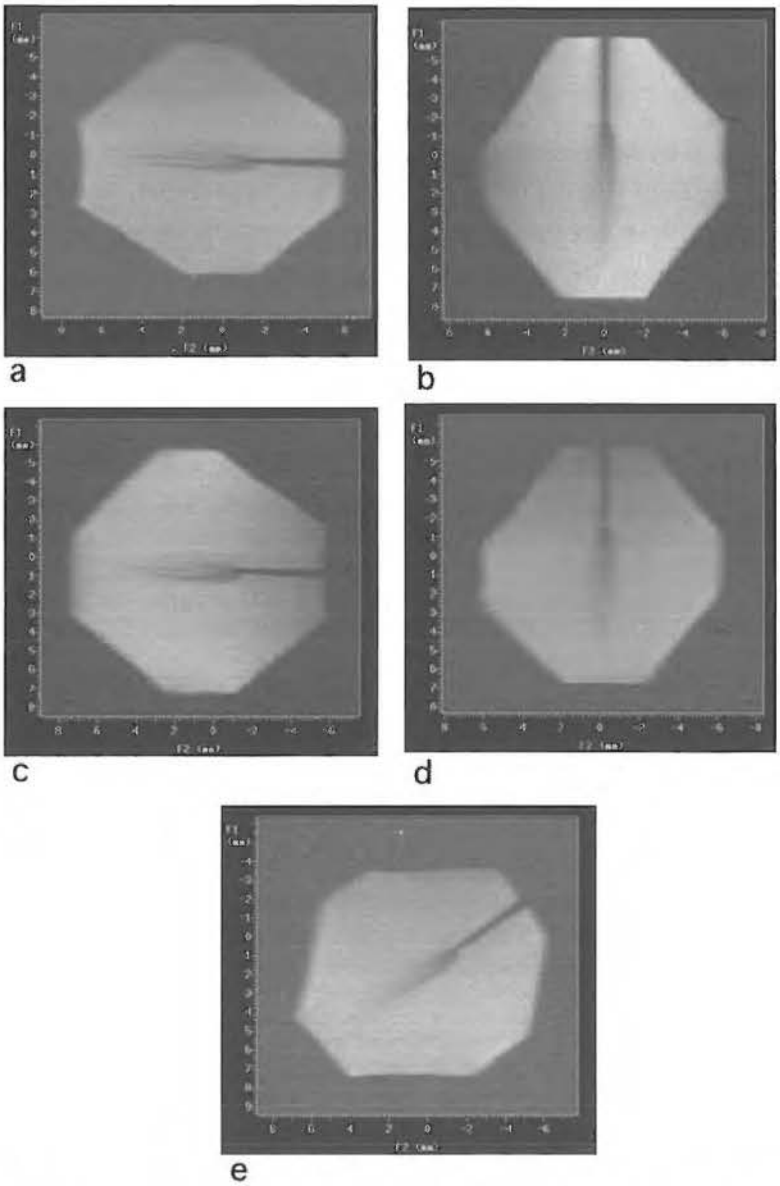

*Figure 4.11: MRI images with switched read and phase gradient orientation: (a) and (b) pre-crack perpendicular to $B_0$, yzx and zyx gradient orientation, respectively; (c) and (d) idem but with the pre-crack along $B_0$; (e) the pre-crack placed under an angle of 54° with respect to $B_0$.*

Figure 4.11a and 4.11b were recorded with switched read and phase gradient orientation. Both images were acquired with an echo time of 1 ms and a repetition time of 2 s and have an inplane resolution of 100 x 100 μm. It is clear from the images that the pre-crack direction has to be along the read direction (Figure 4.11a) to avoid the loss of almost all fine structure due to susceptibility effects.

The same kind of experiment was implemented where the pre-crack was placed along the $B_0$ field (Figure 4.11c-d). From this experiment, compared to the previous, it is clear that the position of the pre-crack with respect to the main magnetic field has no influence on the image resolution.

A loss of image detail is also observed when the sample was positioned so that the crack makes an angle of 54° with the main magnetic field $B_0$ due to susceptibility effects (Figure 4.11e).

*Increase of the inplane resolution*

An improvement of the inplane resolution from 100 x 100 μm to 66 x 66 μm results in a gain of image detail (Figure 4.12). A resolution of 66 x 66 μm will be used for further experiments (except for the images as a function of increasing load).

Tensile stress clearly results in the appearance of numerous damage bands in the material, which converge toward the crack tip.

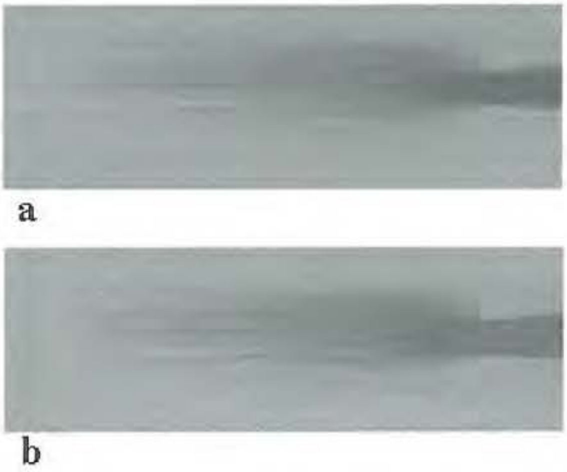

*Figure 4.12: Images of an ABS specimen strained to yield stress with an inplane resolution of 100 x 100 μm (a) and 66 x 66 μm (b).*

### 4.2.3.2 Images as a function of increasing load

A series of images of ABS plates with increasing load are presented in Figure 4.13. All images have a slice thickness of 3.25 mm and an inplane resolution of 100 x 100 μm.

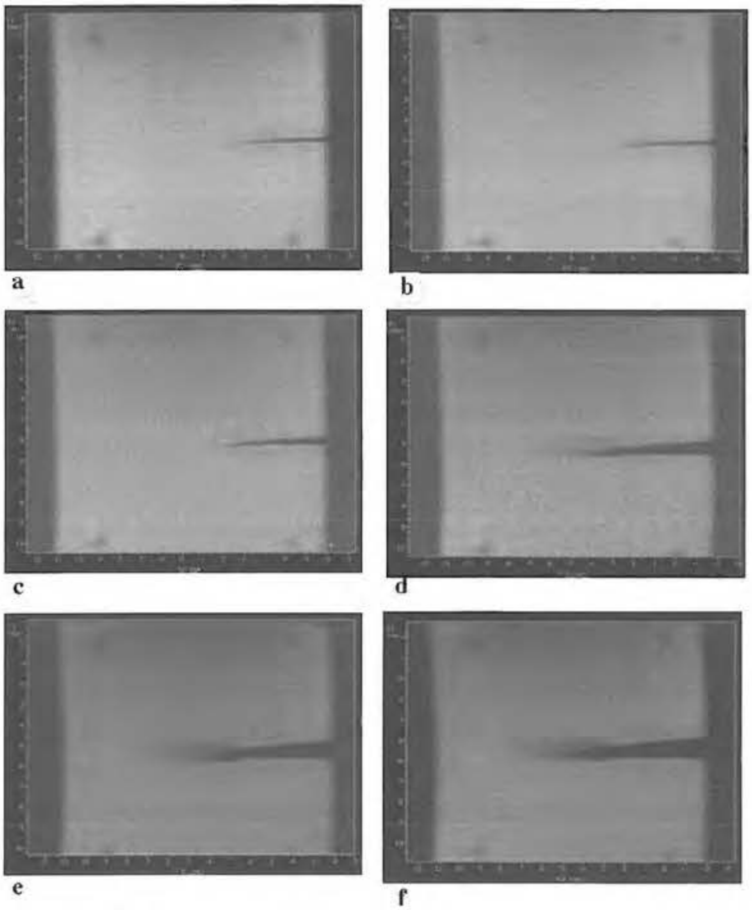

*Figure 4.13: Images of ABS plates as a function of increasing stress. (a) 7.07 MPa; (b) 14.15 MPa; (c) 23.58 MPa; (d) 30.66 MPa; (e) 33.01 MPa; (f) 37.37 MPa.*

By making use of the distance markers, visible in the MRI images, the stress-strain relation could be determined (Figure 4.14).[153] The percentage strain was determined by the relation

$$\varepsilon = \frac{l - l_0}{l_0} \times 100 \qquad (4.1)$$

in which $l_0$ is the initial distance between the markers (right side) and l the distance after stretching. Further drawing leads to a break of the material.

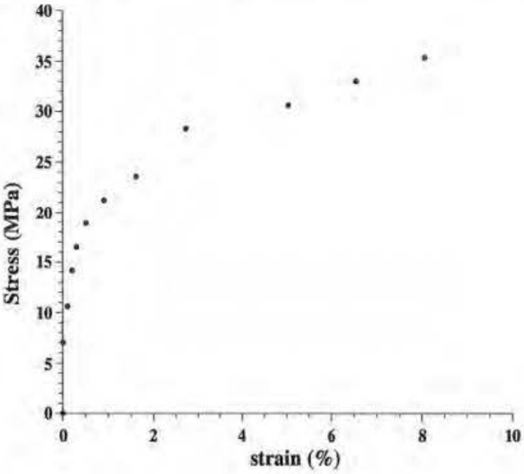

*Figure 4.14: Stress-strain curve measured for ABS with the stretching device; further loading leads to break of the material.*

The yield point is reached around 8 % elongation. The material yield stress is overestimated due to friction between the screw bar and the nut during straining. The torsion of the specimen in the device and friction between the sample and the glass tube will also have a contribution to the overestimation of the yield stress. A broader glass tube and a more sophisticated gliding surface between the screw bar and the nut could reduce the overestimation to a minimum. However, this difference is sufficiently small in view of the goal of this study.

#### 4.2.3.3 Reduction of the slice thickness

As already shown before, an improvement of the inplane resolution results in a gain of image detail. An image of ABS under critical load with an inplane resolution of 66 x 66 μm as shown in Figure 4.15a shows much more detail of the damage bands in ABS as compared to the images of Figure 4.13.

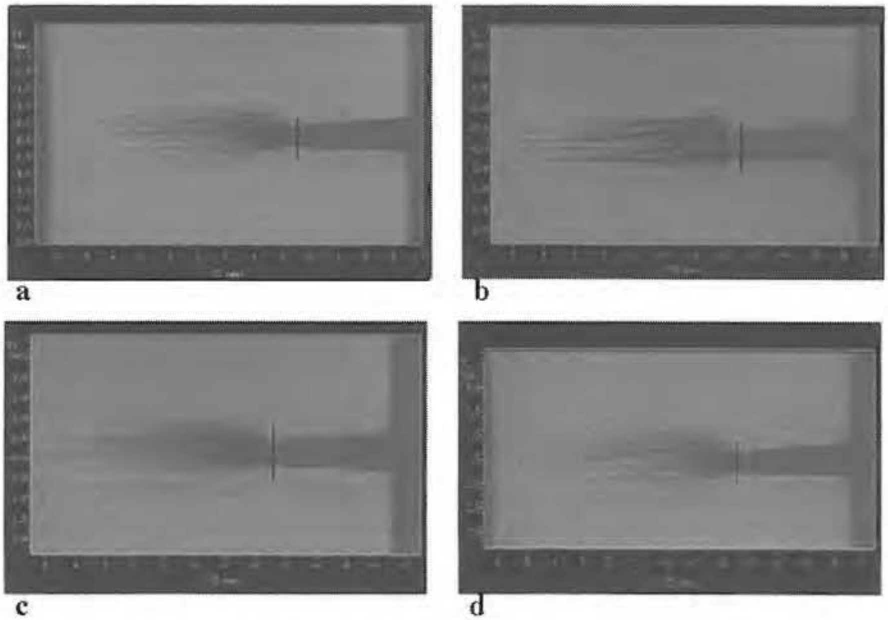

*Figure 4.15: (a) image of a 3.25 mm slice of ABS under critical load, (b) idem but with a slice thickness of 1.625 mm of the outer part of the plate, (c) idem but with a slice thickness of 1.625 mm of the inner part of the plate, and (d) idem after unloading. The depth of the original notch is indicated by a vertical line.*

An additional gain of image detail is obtained by a reduction of the slice thickness.[153] By comparing parts a and b, c of Figure 4.15 a significant improvement of the detection of morphological details in the damage bands and around the crack tip is observed. By comparing Figure 4.15b and 4.15c, it becomes clear that the structure of the damage bands is not completely homogeneous over the thickness of the plate, explaining the influence of slice thickness on image detail. To our knowledge, damage bands in ABS under deformation were not visualised in this detail so far.

Images of the same sample shortly after unloading reveal that the damage bands remain present and are almost unaffected by unloading (Figure 4.15d). The structure of the damage bands remains, even 24 h after unloading.

Figure 4.15 illustrates that useful insights in the fracture process of polymer materials can already be obtained by analysing strain induced phenomena in the viscoelastic phase using spin-echo imaging techniques without advanced solid state imaging methods.[141,154]

#### 4.2.3.4 Determination of the spatially resolved spin density ($M_0$) and the $T_{2H}$ and $T_{1H}$ relaxation decay times under load and after unloading

To study whether the image appearance of the damage bands is caused by changes in material density and/or strain induced chain orientation (molecular mobility) in the rubbery phase, the spatial dependence of $M_0$ and of the $T_{1H}$ and $T_{2H}$ relaxation times was determined. The relaxation times $T_{2H}$ and $T_{1H}$ provide information on slow, long spatial scale and fast, local chain mobility, respectively. The proton spin density ($M_0$) is directly related to the amount of rubber proton spins. A quantitative, spatial dependent determination of these parameters ($T_{2H}$ and $M_0$) is extracted out of a series of images taken as a function of TE (echo time) and as a function of TR (repetition time) ($T_{1H}$ and $M_0$). The spin density ($M_0$) and the spin-spin relaxation time ($T_{2H}$) for different picture elements (Figure 4.16) were determined by analysis of the echo amplitude as a function of TE (13 values between 1.10 ms and 2.40 ms) with a fixed TR of 1.25 s, using the following relation:

$$\ln M(\mathrm{TE}) = \ln M_0 - \mathrm{TE}/T_{2H} \qquad (4.2)$$

The spatial dependence of the spin-lattice relaxation time ($T_{1H}$) and $M_0$, were determined from a series of images taken as a function of TR (10 values between 0.25 s and 4 s) with a fixed TE of 1.10 ms, according to the following relation:[155]

$$M(TR) = M_0(1 - \exp^{-TR/T_{1H}})\exp^{-TE/T_{2H}} \qquad (4.3)$$

The reference value for the three properties is represented by an average value obtained from ten unaffected locations (Figure 4.16).

The images acquired for this quantitative analysis have a slice thickness of 1.625 mm.

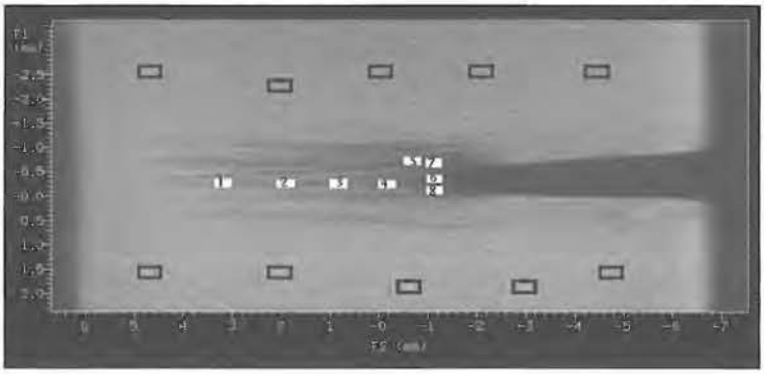

*Figure 4.16: Image of ABS showing the fixed spatial locations where the spin density ($M_0$), $T_{1H}$ and $T_{2H}$ relaxation times were determined. For values see Tables 4.2 and 4.3. All picture elements are 0.16 x 0.31 mm in dimension. The reference spots (black rectangles) have a similar dimension and are located at least 1.5 mm from the damage bands.*

| Spatial Position | Loaded | | | |
|---|---|---|---|---|
| | $T_{2H}$ (ms) | $M_0$ | $T_{1H}$ (s) | $M_0$ |
| 1 | 1.00 | 90 | 0.72 | 91 |
| 2 | 1.02 | 75 | 0.73 | 76 |
| 3 | 0.91 | 78 | 0.77 | 69 |
| 4 | 0.94 | 54 | 0.75 | 52 |
| 5 | 0.96 | 35 | 0.72 | 31 |
| 6 | 1.06 | 22 | 0.71 | 23 |
| 7 | 0.95 | 42 | 0.68 | 38 |
| 8 | 1.08 | 28 | 0.75 | 34 |
| ref. | 1.00 | 100 | 0.75 | 100 |

*Table 4.2: Spatial dependence of the spin density ($M_0$) and $T_{2H}$ and $T_{1H}$ relaxation times for ABS under critical load. The positions are indicated in Figure 4.16. The averaged 95% confidence limit is 5% for the relaxation times and 2% for the $M_0$ values.*

Table 4.2 shows the values of $M_0$, $T_{1H}$ and $T_{2H}$ for several picture elements in the image of ABS under critical load. No significant spatial differences in $T_{2H}$ and $T_{1H}$ can be detected in the damage bands under load as compared to the reference values in areas that are not affected by strain. This means that the decrease in image intensity in the damage bands can not be attributed to a strain induced decrease of segmental mobility nor to strain induced chain orientation in the rubbery phase. Concerning $T_{2H}$ and $T_{1H}$, the same conclusion can be drawn for the results of the measurements after unloading the sample (Table 4.3).

Also the $T_{2H}$ relaxation time measured on an unloaded sample at different angles with respect to the magnetic field, shows no angular dependency and confirms the absence of stress induced orientation of rubbery chains.

| Spatial Position | Unloaded | | | |
|---|---|---|---|---|
| | $T_{2H}$ (ms) | $M_0$ | $T_{1H}$ (s) | $M_0$ |
| 1 | 0.98 | 92 | 0.78 | 96 |
| 2 | 0.98 | 84 | 0.74 | 86 |
| 3 | 0.90 | 88 | 0.75 | 77 |
| 4 | 0.94 | 62 | 0.73 | 62 |
| 5 | 0.96 | 42 | 0.84 | 43 |
| 6 | 1.06 | 26 | 0.74 | 30 |
| 7 | 0.96 | 40 | 0.76 | 39 |
| 8 | 0.88 | 52 | 0.71 | 46 |
| ref. | 1.00 | 100 | 0.77 | 100 |

*Table 4.3: Spatial dependence of the spin density ($M_0$) and $T_{2H}$ and $T_{1H}$ relaxation times for ABS after unloading the sample. The positions are indicated in Figure 4.16. The averaged 95% confidence limit is 5% for the relaxation times and 2% for the $M_0$ values.*

On the other hand, a significant reduction of $M_0$ is observed in the (dark) regions of the damage bands. The material density in the near crack tip region is reduced to a maximum of about one fourth of the normal density due to severe rubber particle cavitation. Moreover, the density decrease extends to a 'large' distance from the crack tip. Unloading results in a minor recovery in the density of the material in the damage zone although the structure of the damage bands remains unchanged. The fracture resistance of rubber-toughened plastics is known to be critically dependent upon void formation in the rubber phase.[156] In most types of toughened plastics, cavitation of the rubber particles ahead of a crack tip is followed by shear yielding in the intervening matrix to form dilution bands, thereby allowing the material to yield at greatly reduced stresses. There is also a growing body of evidence that shows that rubber particle cavitation is a necessary precursor to multiple crazing in toughened glassy polymers such as ABS and HIPS (high-impact polystyrene).[74,76]

### 4.2.4 Conclusion

The strong concentration of damage in bands emanating from the crack tip indicates an unstable material behaviour against damage and deformation. This inhomogeneous damage distribution may be considered as sub optimal. Smit[77] demonstrated that material deformation instability is related to strain softening and has an adverse effect on toughness. If cavitation of the rubber particles is achieved in regions of high tensile stress, the matrix polymer can deform plastically by shear yielding before craze initiation takes place. Ideally, this plastic flow process is activated in the entire matrix thus resulting in massive energy dissipation and hence increase of fracture toughness. Indeed, ABS shows strain softening and the present investigation illustrates that material instability results in severely localised damage. However, this study also demonstrates that ABS allows an extreme amount of damage before actual material separation occurs. Further improvement of the toughness of ABS might be achieved by reducing the unstable deformation and damage behaviour.

# 4.3 PBT/PTMO: Changes in microstructure during mechanical deformation

## 4.3.1 Introduction

Block copolymers of poly(butylene terephthalate) (PBT) and poly(tetramethylene oxide) (PTMO) are poly(ether esters), which belong to the class of thermoplastic elastomers. The PBT/PTMO block copolymers are of special interest due to their excellent mechanical properties, like mechanical strength and elastic properties in a wide temperature range. The positive characteristics of both the homopolymers are combined, i.e. a high melting point ($T_m$) (PBT) and a low $T_g$ (PTMO). They consist of hard segments formed by the PBT blocks and soft segments consisting of PTMO chains.[157]

This microphase structure of hard and soft segments is strongly responsible for the mechanical properties of the copolymer system. By varying the amount and block length of the hard and soft segments, a wide range of materials with different mechanical properties can be covered. Compared to the conventional rubbers, thermoplastic elastomers are superior in properties and recycling.

For elastomeric materials it is of special interest to study the changes in microphase structure that occur in the material during mechanical deformation. Knowledge of the microphase behaviour and strain induced chain alignment is essential for a better understanding of the macroscopic properties of these materials.

NMR imaging on loaded specimens with a crack grown under critical conditions is reported. A rather continuous distribution of stress induced material response is observed that disappears almost completely upon unloading. It is studied whether image contrast arises from changes in chain mobility or in material density or a combination of both.

## 4.3.2 Material characteristics

A block copolymer of poly(butylene terephthalate) (PBT) and poly(tetramethylene oxide) (PTMO) was studied. The average block length of the PTMO blocks is 1000 g/mol and the amount of PTMO is 35 wt %. The molecular weight $M_n$ of the block copolymer is about 25000 g/mol. The $M_w/M_n$ ratio for PTMO and PBT blocks is about 1.6 and 2, respectively.[157]

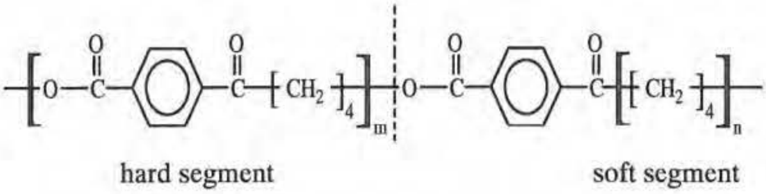

### 4.3.2.1 Scanning electron micrographs

Scanning electron micrographs of a PBT/PTMO sample with a pre-crack, strained to yield stress in the stretching device are presented in Figure 4.17. The images of a reference sample (Figure 4.17a-b) are compared with images of a sample under load (Figure 4.17c-d) and those of a sample after unloading (Figure 4.17e-f). After removing the sample of the stretching device, the crack closed largely to the original shape of the pre-crack. The crack was pulled open by means of wedge-shaped metallic piece in order to visualise the stress induced material response by SEM. A blunt notch tip without crack propagation, in contrast with ABS, is observed on a strained sample (image not shown). Remarkable differences in phase morphology are present between a reference location (a-b) and the damage zone in front of the crack tip of a sample under load (c-d). After unloading the morphology resembles this of the reference sample indicating a reversible stress induced material response.

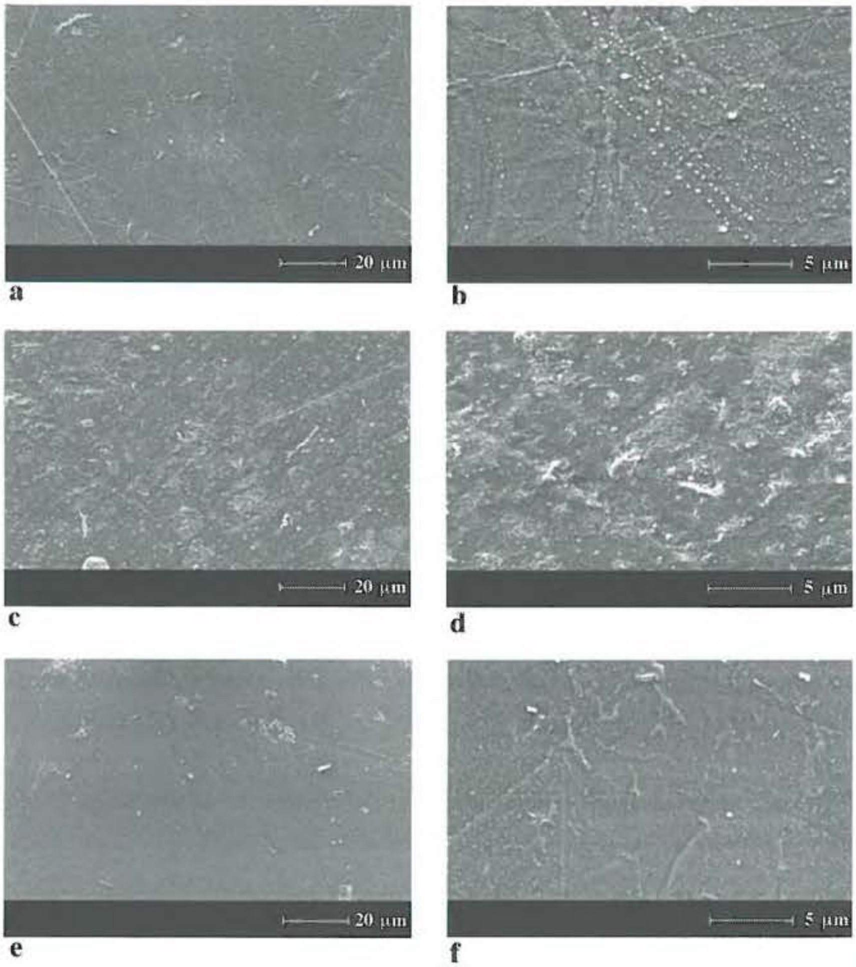

*Figure 4.17: SEM micrographs of a PBT/PTMO specimen: (a,b) images of a reference location, (c,d) damage zone of a sample under load and (e,f) images of a sample after unloading.*

### 4.3.3 Visualisation of stress induced phenomena in PBT/PTMO by MRI

A reference image of a native PBT/PTMO specimen with a pre-crack and distance markers is presented in Figure 4.18.

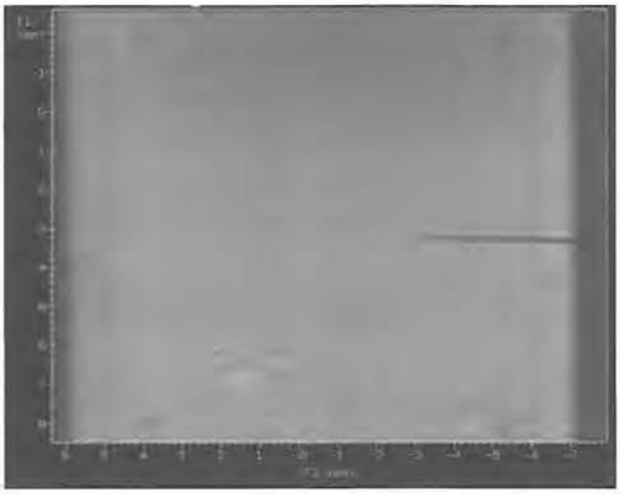

*Figure 4.18: Reference image of a PBT/PTMO plate showing the notch and the distance markers (dark circles).*

Because of the short $T_{2H}$ relaxation time (0.56 ms) of the rubbery phase (PTMO) which is visualised, it was required to reduce the echo time (TE) to a minimum value to obtain a smooth, high qualitative image as shown in Figure 4.18. A TE of 1.05 ms could be reached in combination with an inplane resolution of 100 x 100 μm.

### 4.3.3.1 Images as a function of increasing load

PBT/PTMO images as a function of increasing load are shown in Figure 4.19. All images are non-slice selective and have an inplane resolution of 100 x 100 μm. The samples are measured under load in the dedicated stretching device (see 4.2.2.2). The optimal gradient orientation has been used (see 4.2.3.1).
Strain induced response in the proximity of the crack tip for PBT/PTMO differs strongly from the response in ABS. The PBT/PTMO block copolymer reveals a more homogeneous distribution of stress induced material response, visualised as a black region around the crack tip and which emanates from the tip of the notch.[153] Since for PBT/PTMO no sharp aligned structures, like the damage bands in ABS, appear the inplane resolution was increased to 100 x 100 μm.

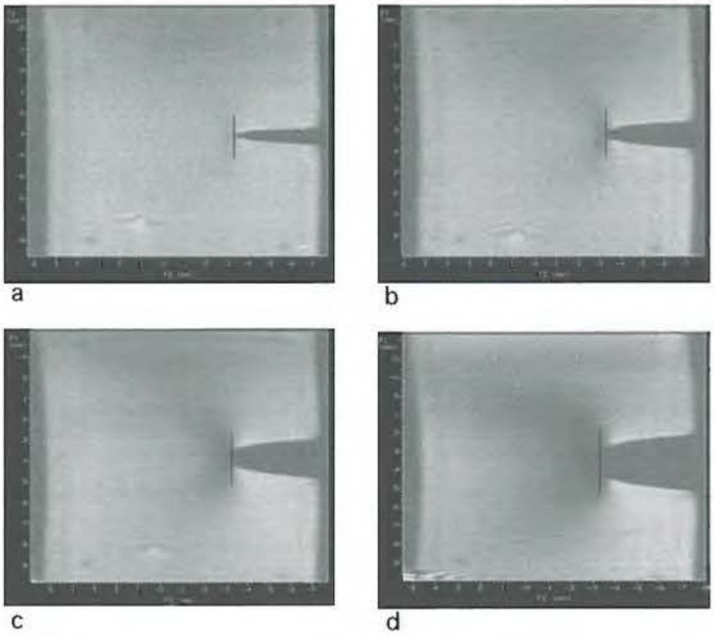

*Figure 4.19: PBT/PTMO MRI micrographs as a function of increasing stress: (a) 11.79 MPa, (b) 16.51 MPa, (c) 20.04 MPa, (d) 29.01 MPa.*

The stress-strain relation was obtained by measuring the distance between the markers (at the right side) and using equation 4.1 (Figure 4.20).

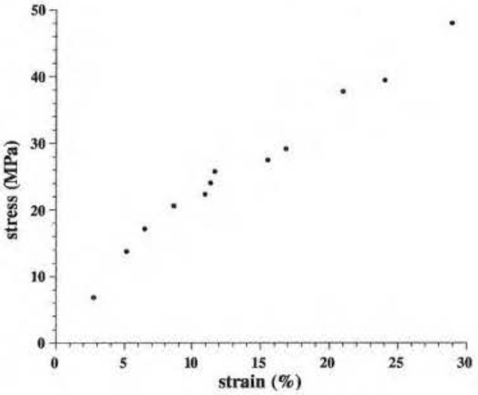

*Figure 4.20: PBT/PTMO stress-strain curve derived from images acquired as a function of increasing stress.*

The yield point is reached at around 29 % elongation with a yield stress of 48 MPa.

An image of the sample after unloading is shown in Figure 4.21. Upon unloading the stress-induced damage has quasi completely disappeared, no decrease of image intensity can be observed, only a small opening of the crack makes the difference with the reference image.

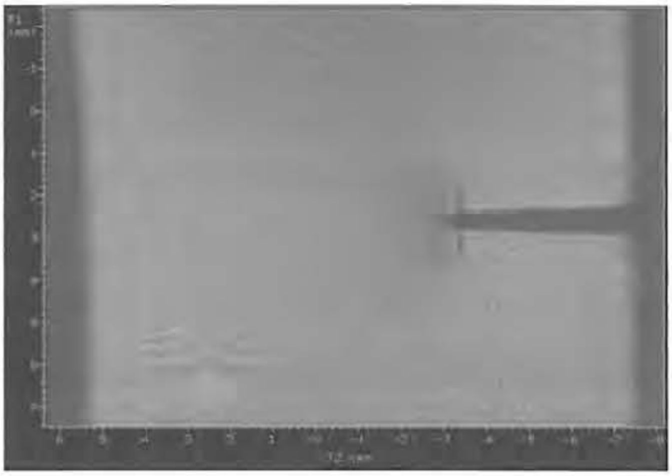

*Figure 4.21: Image of the PBT/PTMO sample, shown in figure 4.19, after removing the stress. The depth of the original notch is indicated by a vertical line.*

#### 4.3.3.2 Poisson contraction

A reduction of the sample thickness (visible by eye) in front of the crack tip occurs by putting the sample under stress. To avoid the effect of this Poisson contraction on the quantitative investigation of the spatially resolved spin density ($M_0$) (see 4.3.3.3), a slice in the centre of the sample was selected to be imaged. The thickness of the slice was derived out of an image with a different gradient orientation, namely zxy (Figure 4.22a).

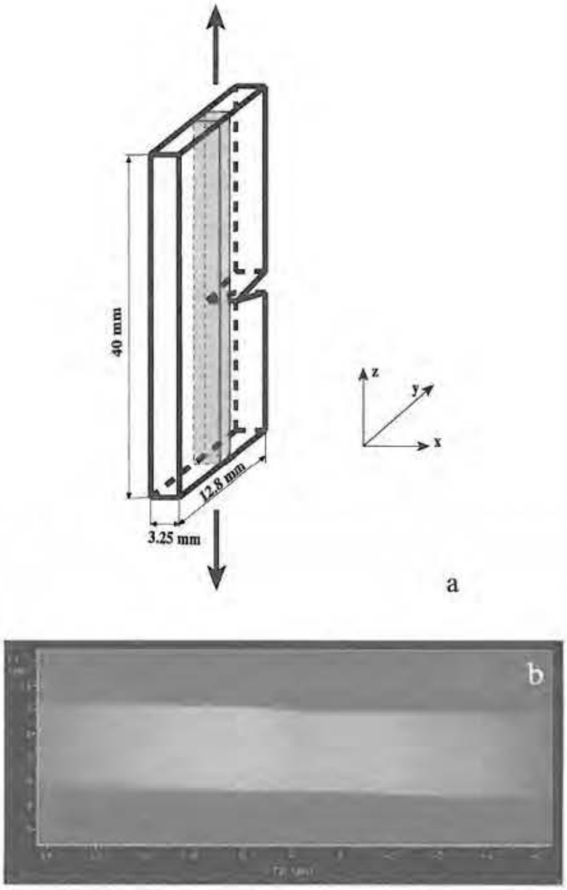

*Figure 4.22: (a) Schematic representation of the slice selection in the sample. (b) MRI image of a cross-section to visualise the Poisson contraction.*

It can be concluded that a slice selection of 2 mm in thickness, in the centre of the sample (Figure 4.22b) ensures that a reduction in spin density cannot be attributed to the Poisson contraction.

#### 4.3.3.3 Determination of the spatially resolved spin density ($M_0$) and the $T_{2H}$ and $T_{1H}$ relaxation decay times under load.

A similar study as for ABS (see 4.2.3.4) has been performed on a PBT/PTMO specimen in order to investigate whether the material response induced by stress, visible as a decrease in image intensity, is caused by changes in material density and/or strain induced chain orientation in the elastomeric phase. The spatial dependence of $M_0$ and of the $T_{2H}$ and $T_{1H}$ relaxation times was determined out of a series of images taken as a function of TE ($T_{2H}$ and $M_0$) and as a function of TR ($T_{1H}$ and $M_0$). The spin density ($M_0$) and the spin-spin relaxation time ($T_{2H}$) for different picture elements (Figure 4.23) were determined by analysing the echo amplitude as a function of TE (13 values between 1.05 ms and 2.00 ms) with a fixed TR of 1.00 s, by using equation 4.2. The spatial dependence of the spin-lattice relaxation time ($T_{1H}$) and $M_0$, was determined from a series of images taken as a function of TR (10 values between 0.25 s and 4 s) with a fixed TE of 1.10 ms, according to equation 4.3.

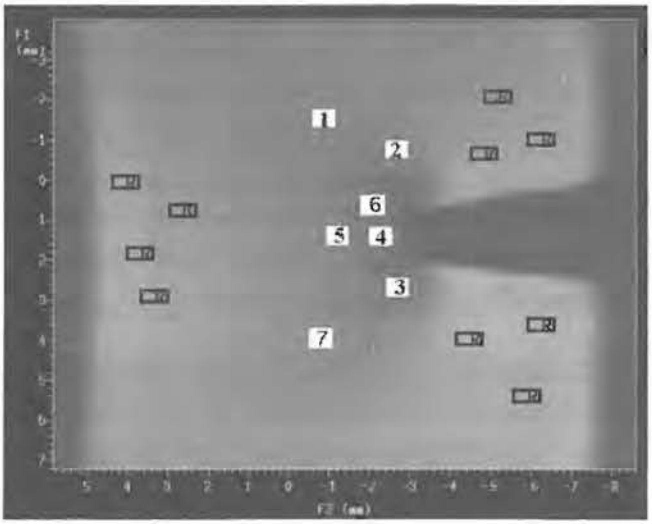

*Figure 4.23: Image of PBT/PTMO showing the fixed spatial locations for which the spin density ($M_0$), $T_{1H}$ and $T_{2H}$ relaxation times were determined. The values obtained are presented in Table 4.4. The reference spots (black rectangles) are located at least 1.5 mm from the damage zone.*

Table 4.4 shows the spatial dependent results of $M_0$, $T_{2H}$ and $T_{1H}$ for the PBT/PTMO block copolymer.

| spatial | loaded | | | |
|---|---|---|---|---|
| position | $T_{2H}$ (ms) | $M_0$ | $T_{1H}$ (s) | $M_0$ |
| 1 | 0.41 | 100 | 0.80 | 96 |
| 2 | 0.40 | 52 | 0.81 | 53 |
| 3 | 0.40 | 74 | 0.79 | 70 |
| 4 | 0.43 | 47 | 0.83 | 51 |
| 5 | 0.42 | 100 | 0.83 | 100 |
| 6 | 0.44 | 50 | 0.81 | 57 |
| 7 | 0.42 | 104 | 0.83 | 106 |
| reference | 0.56 | 100 | 0.84 | 100 |

*Table 4.4: Spatial dependence of the spin density ($M_0$) and the $T_{2H}$ and $T_{1H}$ relaxation times for PBT/PTMO under critical load. The positions are indicated in Figure 4.23. The averaged 95% confidence limit is 3% for the relaxation times and 2% for the $M_0$ values.*

In contrast to ABS, a significant reduction in the $T_2$ decay time is observed in a broad zone around the crack tip, as compared to the reference locations. The decrease in $T_{2H}$ can be ascribed to a decrease in long range mobility of PTMO chains due to strain induced chain alignment, since PBT/PTMO block copolymers with short PTMO blocks show strain induced chain orientation but no crystallisation.[158] This is confirmed by a $^{13}C$ NMR study of Schmidt et.al.[157] Unstrained PBT/PTMO block copolymers with a large block length (1500 - 2000 g/mol) and high amount of PTMO (60 wt %) show a clear phase separation into mobile PTMO-rich domains and more rigid mixed PTMO/PBT domains. Uniaxial stretching of these block copolymers results in a strain induced crystallisation in the mobile PTMO-rich domains. The crystallinity increases with increasing PTMO content and block length. Non-crystalline PTMO chains become oriented but less than the crystalline.

A decrease in the spin density ($M_0$) is observed only close to the crack tip (Table 4.4; see location 2, 3, 4 and 6). Cavitation is more moderate and is only observed in the immediate neighbourhood of the crack tip. Chain stretching is observed in a more extended region around the tip.

Figure 4.21 shows that unloading of the PBT/PTMO block copolymer results in an almost complete vanishing of strain induced chain orientation ($T_{2H}$ effect) and spin density effect.

### 4.3.3.4 Determination of the spatially resolved spin density ($M_0$) and the $T_{2H}$ and $T_{1H}$ relaxation decay times under load and after unloading at 50 °C

An increase in temperature results in an increase of molecular chain motions which translates in a slower spin-spin relaxation and thus a longer $T_{2H}$ relaxation time (see section 1.2.1.4). As a consequence measurements at higher temperature (and with the same echo time) result in images with a higher sensitivity because a smaller fraction of the proton magnetisation is relaxed at the detection of the echo signal (Figure 4.24).

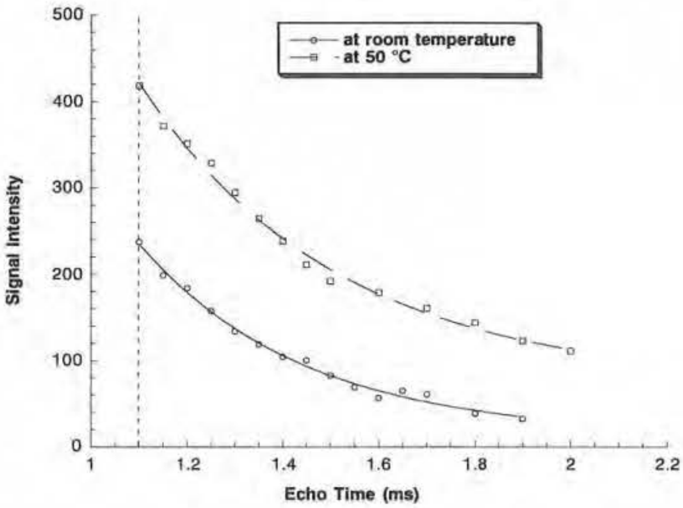

*Figure 4.24: Curve fit of the evolution of the echo amplitude (signal intensity) as a function of the echo time according to equation 4.2.*

Upon rising the temperature from room temperature to 50 °C, an increase in the $T_{2H}$ decay time from 0.56 ms to 0.76 ms is observed. The spatially resolved $M_0$, $T_{2H}$ and $T_{1H}$ obtained under load (same conditions and spatial locations as at room temperature) are presented in Table 4.5.

| Spatial position | Loaded | | | |
|---|---|---|---|---|
| | $T_{2H}$ (ms) | $M_0$ | $T_{1H}$ (s) | $M_0$ |
| 1 | 0.68 | 94 | 0.94 | 90 |
| 2 | 0.58 | 86 | 0.95 | 79 |
| 3 | 0.62 | 86 | 0.96 | 85 |
| 4 | 0.65 | 84 | 0.94 | 81 |
| 5 | 0.71 | 94 | 0.94 | 88 |
| 6 | 0.60 | 100 | 0.96 | 96 |
| 7 | 0.70 | 104 | 0.94 | 99 |
| reference | 0.76 | 100 | 0.92 | 100 |

*Table 4.5: Spatial dependence of the spin density ($M_0$) and the $T_{2H}$ and $T_{1H}$ relaxation times for PBT/PTMO under critical load at 50 °C. The positions are indicated in Figure 4.23. The averaged 95% confidence limit is 4 % and 2 % for the $T_{2H}$ and $T_{1H}$ relaxation times, respectively and 3 % for the $M_0$ values.*

A remarkable change in the localised $T_{2H}$ relaxation times is observed. A decrease in $T_{2H}$ is still observed for all locations with respect to the reference value but in a different amount. Close to the crack tip (locations 2, 3, 4 and 6) a considerable larger decrease (21 %) as compared to the locations 1, 5 and 7 (8 %) is obtained. These locations also showed a remarkable decrease in $M_0$ at room temperature.

A decrease in the spin density ($M_0$) is only observed for locations close to the crack tip (locations 2, 3 and 4) but the decrease is reduced to ± 15 %.

In order to find out if the remaining decrease of 15 % in $M_0$ is due to cavitation a spatially dependent study of the contrast parameters at 50 °C is performed after unloading the sample. These contrast parameters are presented in Table 4.6.

| Spatial position | Unloaded |  |  |  |
|---|---|---|---|---|
|  | $T_{2H}$ (ms) | $M_0$ | $T_{1H}$ (s) | $M_0$ |
| 1 | 0.67 | 94 | 0.96 | 90 |
| 2 | 0.67 | 84 | 0.94 | 84 |
| 3 | 0.73 | 80 | 0.94 | 81 |
| 4 | 0.68 | 79 | 0.94 | 80 |
| 5 | 0.70 | 84 | 0.94 | 84 |
| 6 | 0.65 | 96 | 0.95 | 93 |
| 7 | 0.73 | 98 | 0.94 | 99 |
| reference | 0.72 | 100 | 0.93 | 100 |

*Table 4.6: Spatial dependence of the spin density ($M_0$) and the $T_{2H}$ and $T_{1H}$ relaxation times for PBT/PTMO after unloading at 50 °C. The positions are indicated in Figure 4.23. The averaged 95% confidence limit is 4 % for $T_{2H}$, 2 % for $T_{1H}$ and 3 % for the $M_0$ values.*

While the reduction in $M_0$ remains after unloading, the decrease in long range mobility ($T_{2H}$) of the PTMO chains due to strain induced chain alignment has almost completely vanished. An important conclusion can be drawn from of these results: the induced chain orientation is a reversible effect while the reduction in $M_0$ close to the tip is an effective reduction of the proton density which can be ascribed to cavitation of the elastomeric particles.

### 4.3.4 Conclusions

Under the conditions of critical load the PBT/PTMO block copolymer reveals a rather continuous stress distribution in the proximity of the crack tip. The quantification of image contrast, by the spatial resolved values of the spin density and the $T_{2H}$ and $T_{1H}$ relaxation times, has been shown to provide information for a better understanding of the stress induced material response. A significant orientation of the PTMO chains is observed in a broad region around the crack tip together with a small decrease in spin density in the immediate proximity of the tip. While the decrease of the spin density due to cavitation of the elastomeric particles is irreversible, chain alignment in PBT/PTMO block copolymers with rather short block length and small amount of PTMO largely disappears upon unloading.

## 4.4 Stress induced material response in rubber modified Polyamide 6

### 4.4.1 Introduction

Polyamides (PA) are well known as strong engineering polymers. They exhibit high resistance to crack initiation, which imparts high toughness to unnotched material. However, their low resistance to crack propagation leads to embrittlement in the presence of a notch. Upon modification with rubbers, the resistance to crack propagation increases, leading to tough materials. Previous research on rubber toughened polyamides mainly focussed on the influence of the particle size, the interparticle distance, the cavitation behaviour, the rubber concentration and the rubber-matrix interfaces on the toughening effect.[73,80,87,97,102,109] The role of rubber particles in the toughening of semi-crystalline polymers is now understood rather well.[66,67,91,126,129] Rubber particles enhance plastic deformation and promote cavitation. Both mechanisms result in enhanced toughness by the formation of a plastic zone in front of the crack tip, which blunts the sharp crack. Consequently, cracking and crazing is suppressed. During this process, the cavitated rubber particles will change substantially in shape and in volume.[134] Ideally, the plastic deformation is activated in the entire matrix resulting in massive energy dissipation and hence improved fracture toughness. For rubber toughened polyamide 6.6, Bucknall et al. demonstrated the acceleration of local plastic deformation of the matrix by cavitation.[134,135]

In the present study the difference in fracture behaviour of two different types of polyamide 6 (PA6) specimen are examined in which maleic anhydride grafted ethylene-propylene rubber (EPM-*g*-MA) is dispersed in the PA6 matrix. One blend type contains pure rubber particles dispersed in the PA6 matrix, the other type contains PA6 occlusions within the rubber particles and is significantly more tough. The enhanced toughness of the blends with occlusions can be attributed to a more pronounced delocalisation of energy, which is suggested to result from a different deformation mechanism in which the load bearing capacity of the rubbery chains plays an important role.[159]

### 4.4.2 Material Characteristics

Two types of PA6-*blend*-(EPM-*g*-MA) blends were investigated. One type of blends consists of pure EPM-*g*-MA rubber dispersed in the PA6 matrix and is represented by a sample containing 20 wt % dispersed phase and which is designated as the standard blend (Bl-st). In the other type of blends, PA6 occlusions are introduced in the dispersed rubbery phase (Bl-oc). Bl-oc1 contains 20 wt % dispersed phase (14 wt % EPM-*g*-MA) while a larger amount of 28.6 wt % (20 wt % EPM-*g*-MA) is introduced in Bl-oc2. An overview is presented in Table 4.7.

| Samples | EPM-*g*-MA wt % | occluded PA6 wt % | dispersed phase wt % |
|---|---|---|---|
| Bl-st | 20 | — | 20 |
| Bl-oc1 | 14 | 6 | 20 |
| Bl-oc2 | 20 | 8.6 | 28.6 |

*Table 4.7: Composition of the PA6/EPM-g-MA blends.*

#### 4.4.2.1 Morphology

Clear differences are observed in the morphology of the specimens as demonstrated by TEM micrographs (Figure 4.25). Whereas in the standard blend (Bl-st) homogeneous rubber particles are dispersed into the PA6 matrix (Figure 4.25a), the rubber particles of the occluded type of blends (Bl-oc1 and Bl-oc2) show a 'salami'-type structure caused by the PA6 occlusions introduced in the dispersed phase (Figure 4.25b-c).

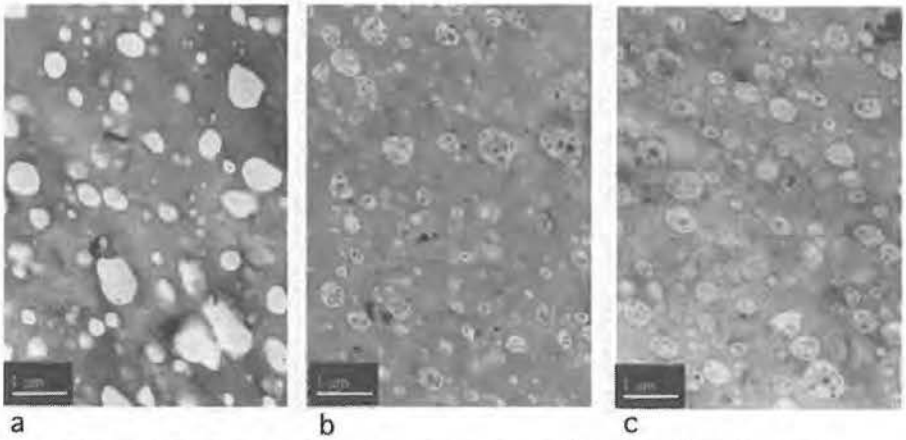

*Figure 4.25: Transmission electron micrographs of the Bl-st (a), the Bl-oc1 (b) and the Bl-oc2 (c) blends.*

### 4.4.2.2 Tensile and impact strength tests

Notched charpy impact tests and tensile strength tests were performed in order to demonstrate the differences in toughness properties between both types of material. Having the same volume fraction of dispersed phase, the Bl-oc1 blend is more tough as compared to Bl-st (Table 4.8) in spite of its lower rubber content and higher E-modulus (Table 4.9).

| Temperature | Bl-st | Bl-oc1 | Bl-oc2 |
|---|---|---|---|
| | I (kJ/m$^2$) | I (kJ/m$^2$) | I (kJ/m$^2$) |
| 23°C | 39.9 ± 0.8 | 51.6 ± 0.3 | 78.0 ± 1.4 |
| -30°C | 16.1 ± 1.1 | N.D. | 24.1 ± 0.7 |

*Table 4.8: Results of the notched charpy impact test, as determined according the ISO 179 standard.*

According to Oshinski et al., non-occluded blends having a 20 wt % dispersed rubbery phase content only reach their optimal impact strength (73 kJ/m$^2$) if a narrow particle size distribution of around 200 - 300 nm is present.[87] Both the Bl-st and Bl-oc1 blends are not situated in this optimal region due to the presence of a rather broad particle size distribution (Figure 4.25). This means that the impact strength probably can be further improved by increasing the volume fraction of the dispersed phase. The Bl-oc2 blend, having a higher volume fraction of the dispersed phase, yields the highest toughness and lowest E-modulus (Table 4.9).

| Mechanical Properties | Bl-st | Bl-oc1 | Bl-oc2 |
|---|---|---|---|
| E-modulus (N/mm$^2$) | 2052 ± 52 | 2266 ± 37 | 1820 ± 36 |
| yield stress (N/mm$^2$) | 50.95 ± 0.22 | 58.08 ± 0.24 | 45.76 ± 0.17 |
| yield strain (%) | 3.96 ± 0.10 | 3.94 ± 0.06 | 4.02 ± 0.02 |
| stress at break (N/mm$^2$) | 41.23 ± 1.24 | 41.75 ± 0.60 | 39.85 ± 1.05 |
| strain at break (%) | 32.10 ± 5.24 | 36.96 ± 11.92 | 29.33 ± 8.05 |

*Table 4.9: Tensile properties as determined according the ISO 527 standard at a rate of 50 mm/min.*

The goal of this study is to explain the improved toughness of the blends containing PA6 occlusions in the dispersed rubbery phase from a molecular point of view.

#### 4.4.2.3 SEM micrographs

Scanning electron micrographs (SEM) of blend plates that were strained to yield stress clearly show a rather similar degree of cavitation of the rubber particles in the deformation zone ahead of the starter crack (Figure 4.26).

As is extensively described in literature, cavitation is an important energy dissipating deformation mechanism in rubber toughened thermoplastic materials.[160] Upon loading, the rubber particles become elongated and enlarged as can be judged from the shape and dimension of the cavities. The elongation of the rubber particles, along the direction of local deformation of the PA6 matrix,[74] results in void growth due to high stress near the crack tip. Cavity walls are lined with a layer of rubber as demonstrated by Pearson et al. by means of back scattered electron imaging.[68] It is clear that the macroscopically observed stress whitening results mainly from simple void growth rather than from multiple crazing.

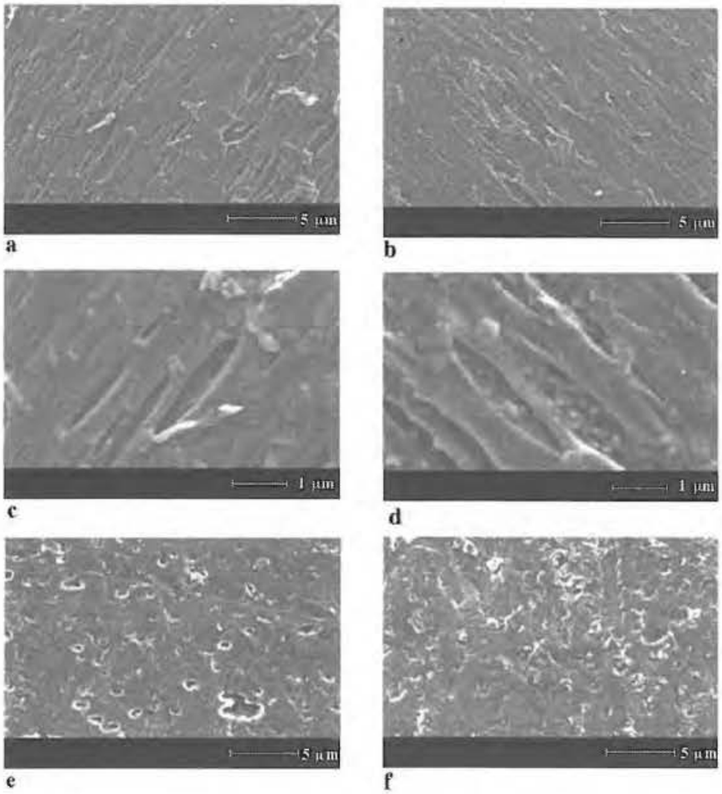

*Figure 4.26: Scanning electron micrographs in the near proximity of the crack tip of the Bl-st blend (a,c) and of the Bl-oc2 blend (b,d) and of the deformation zone 500 μm ahead of the crack tip of the Bl-st blend (e) and of the Bl-oc2 blend (f).*

### 4.4.3 Visualisation of stress induced material response in the PA6-(EPM-*g*-MA) blends by MRI

#### 4.4.3.1 Images as a function of increasing load

Images of the Bl-st blend and the Bl-oc2 are presented in Figure 4.27. The stress induced material response ahead of the crack tip can be differentiated as a hypo-intense deformation zone. For the nylon blends the damage in the material is more localised in front of the crack tip as compared to the stress induced damage for the PBT/PTMO blend.

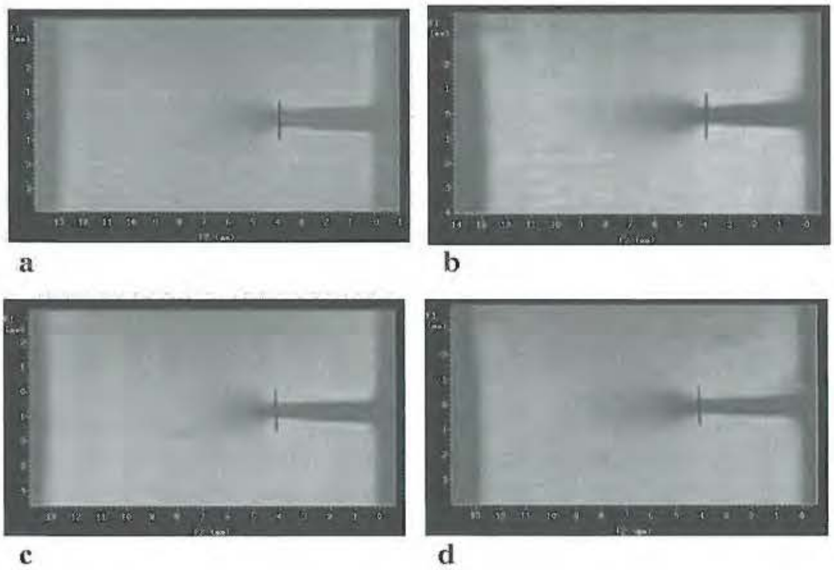

*Figure 4.27: (a-b) MRI images of the Bl-st and Bl-oc2 blends under 54 MPa, respectively; (c-d) images of the Bl-st and Bl-oc2 blends after unloading, respectively . A vertical bar indicates the depth of the original notch (4 mm).*

An appreciable larger deformation zone is observed for the Bl-oc2 blend as compared to the Bl-st blend. This improved dissipation of stress energy confirms the big gain in toughness for the occluded blend. The stress induced material response is quite irreversible as can be judged from the images obtained after unloading (Figure 4.27c-d). Images of notched plates that were drawn to yield stress on a commercial straining instrument show identical dimensions of stress induced material response and confirm that critical load is retained during the MRI experiment.

The stress-strain relations for Bl-st and Bl-oc2 obtained out of a series of images acquired as a function of increasing load are shown in Figure 4.28.

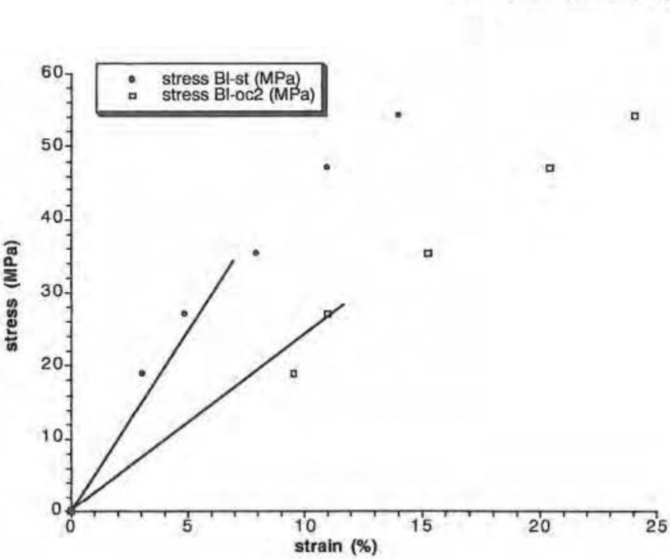

*Figure 4.28: Stress-strain curves for Bl-st and Bl-oc2 plates obtained from images acquired as a function of increasing load.*

Both samples were elongated until a stress of 54 MPa was reached. The higher toughness of the Bl-oc2 is reflected by the smaller initial slope of the stress-strain curve (conform the E-modulus).

### 4.4.3.2 Determination of the spatially resolved spin density ($M_0$) and the $T_{2H}$ and $T_{1H}$ relaxation decay times of the Bl-st and the Bl-oc2 blends under load and after unloading

A similar study as for ABS and PBT/PTMO has been performed for the nylon blends. Since image intensity can be a rather complex function of the local concentration of protons of the rubbery material ($M_0$) and the $T_{1H}$ and $T_{2H}$ relaxation times, the spatial dependence of these MRI contrast parameters was investigated in order to determine whether the hypo-intensity of the deformation zone is caused by cavitation and/or strain induced molecular chain elongation of the rubbery chains. Please keep in mind that these images only visualise the rubbery phase since the rather long echo time (1.1 ms) acts as a highly selective $T_{2H}$ relaxation time filter, excluding the fast $T_{2H}$ decaying PA6 proton magnetisation. Therefore, the spatial dependent proton spin density ($M_0$) is directly related to the local amount of rubber. Concerning the relaxation of elastomers, the spin-spin relaxation time $T_{2H}$ provides information about the slow, large scale chain mobility while the spin-lattice relaxation time $T_{1H}$ is sensitive towards the fast, local mobility (spectroscopic solid-echo proton wideline $T_{1H}$ measurements demonstrate that spin diffusion of proton magnetisation[161] is not taking place efficiently between the PA6 matrix and the dispersed rubbery phase in these blend materials).

Table 4.10 shows the localised values of the MRI parameters obtained for the Bl-st blend under load (Figure 4.29; locations 1-6). The values determined for the Bl-oc2 blend, having a more extended damage zone (Figure 4.29; locations 1-9), are presented in Table 4.11. The average reference values, derived from several undeformed locations, are given for comparison.

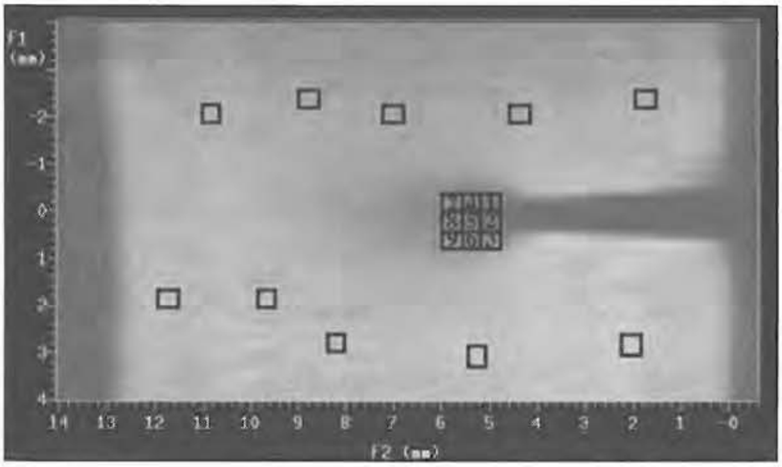

*Figure 4.29: MRI image of the Bl-oc2 blend under critical load. The numbered locations correspond to the spatial locations for which the quantitative spin density ($M_0$) and the $T_{1H}$ and $T_{2H}$ relaxation times were determined. The unmarked squares represent the locations which were used to obtain the $T_{1H}$ and $T_{2H}$ reference values (see tables 4.10- 4.13).*

| Spatial | Bl-st Loaded | | | |
|---|---|---|---|---|
| Position | $T_{2H}$ (ms) | $M_0$ | $T_{1H}$ (s) | $M_0$ |
| 1 | 0.93 | 23 | 0.64 | 21 |
| 2 | 0.98 | 21 | 0.61 | 18 |
| 3 | 0.89 | 36 | 0.66 | 35 |
| 4 | 0.91 | 35 | 0.63 | 31 |
| 5 | 0.91 | 31 | 0.54 | 28 |
| 6 | 0.88 | 35 | 0.66 | 35 |
| ref. | 0.93 | 100 | 0.63 | 100 |

*Table 4.10: Spatial dependence of the spin density ($M_0$) and the $T_{2H}$ and $T_{1H}$ relaxation times under critical load for the Bl-st blend. The spatial locations are indicated in Figure 4.29. The averaged 95% confidence limit for $T_{1H}$, $T_{2H}$ and $M_0$ is about 5%, 8% and 8%, respectively.*

For both the Bl-st and Bl-oc2 blends, a significant decrease of the proton spin density (locations 1-6) is observed in the deformation zone as compared to the undeformed locations. This decrease in spin density, which becomes more pronounced towards the notch tip, provides a measure of the degree of cavitation of the rubbery particles. In the plastic zone, a gradual increase of rubber cavitation takes place towards the tip of the starter crack. Although close to the crack tip (locations 1-6) the amount of cavitation is quite similar for both blends, the volume affected by cavitation is more extended for Bl-oc2 (locations 7-9).

Concerning the $T_{1H}$ relaxation, no significant differences are detected in the stress-whitened zone as compared to the unaffected locations. This means that the local mobility of the remaining, non-cavitated rubber chains is hardly affected by the applied stress.

| Spatial | | | Bl-oc2 Loaded | |
|---|---|---|---|---|
| Position | $T_{2H}$ (ms) | $M_0$ | $T_{1H}$ (s) | $M_0$ |
| 1 | 0.69 | 27 | 0.68 | 27 |
| 2 | 0.74 | 18 | 0.67 | 20 |
| 3 | 0.70 | 31 | 0.62 | 33 |
| 4 | 0.67 | 36 | 0.67 | 38 |
| 5 | 0.61 | 41 | 0.62 | 40 |
| 6 | 0.65 | 40 | 0.63 | 44 |
| 7 | 0.71 | 48 | 0.68 | 50 |
| 8 | 0.67 | 51 | 0.66 | 51 |
| 9 | 0.65 | 59 | 0.65 | 64 |
| ref. | 0.81 | 100 | 0.66 | 100 |

*Table 4.11: Spatial dependence of the spin density ($M_0$) and the $T_{2H}$ and $T_{1H}$ relaxation times under critical load for the Bl-oc2 blend. The spatial locations are indicated in Figure 4.29. The averaged 95% confidence limit for $T_{1H}$, $T_{2H}$ and $M_0$ is about 5%, 8% and 8%, respectively.*

As far as $T_{2H}$ relaxation is concerned, no significant changes are observed in the deformation zone of the Bl-st blend as compared to the average reference value. It means that no stress induced chain elongation takes place in this blend. For Bl-oc2 on the other hand, the $T_{2H}$ decay of the proton spins in the plastic zone is significantly faster as compared to this of the unaffected locations. This faster relaxation of rubbery protons can be assigned to a drop in the long-range mobility of the rubbery chains.

To examine whether some overall preferential orientation direction of the rubbery chains is present in the occluded blends, the $T_{2H}$ decay value was evaluated as a function of the angle between the strain direction and the static magnetic field $B_0$. No angular dependency of the $T_{2H}$ relaxation time however was observed, indicating that no overall preferential orientation of the rubbery chains takes place within the deformation volume (2 x 2 x 4 mm) ahead of the crack tip.

Table 4.12 and 4.13 show the spatial dependent results of $M_0$, $T_{2H}$ and $T_{1H}$ for the Bl-st and the Bl-oc2 after unloading, respectively.

| Spatial | Bl-st Unloaded | | | |
|---|---|---|---|---|
| Position | $T_{2H}$ (ms) | $M_0$ | $T_{1H}$ (s) | $M_0$ |
| 1 | 0.91 | 25 | 0.64 | 26 |
| 2 | 0.98 | 19 | 0.59 | 25 |
| 3 | 0.92 | 52 | 0.62 | 52 |
| 4 | 0.89 | 35 | 0.63 | 37 |
| 5 | 0.90 | 33 | 0.65 | 31 |
| 6 | 0.94 | 51 | 0.64 | 53 |
| ref. | 0.96 | 100 | 0.68 | 100 |

*Table 4.12: Spatial dependence of the spin density ($M_0$) and the $T_{2H}$ and $T_{1H}$ relaxation times after unloading for the Bl-st blend. The spatial locations are indicated in Figure 4.29. The averaged 95% confidence limit for $T_{1H}$, $T_{2H}$ and $M_0$ is about 5%, 8% and 8%, respectively.*

The decrease in $M_0$ is still observed after unloading. Only a slight recovery of the spin density, and almost only for the locations 3, 6 and 9 which are situated at the border of the damage zone, is observed.

While for the PBT/PTMO block copolymer a recovery of the chain mobility after unloading was observed, the drop in long-range mobility, expressed by the decrease of $T_{2H}$, is irreversible for the Bl-oc2 blend (Table 4.13). The $T_{1H}$ relaxation time remains similar after unloading.

In contrast to Bl-st, for which the molecular chain mobility is mainly determined by entanglements, the occlusions in Bl-oc2 not only result in a larger amount of interphase but also introduce topological constraints that can result in strain amplification similar to that observed in filled rubbers. While the hypo-intensity observed in the deformation zone for Bl-st can fully be assigned to the reduction in rubber spin density (cavitation), for Bl-oc2 both cavitation and stress induced chain elongation contribute to the hypo-intensity.

| Spatial | Bl-oc2 Unloaded | | | |
|---|---|---|---|---|
| Position | $T_{2H}$ (ms) | $M_0$ | $T_{1H}$ (s) | $M_0$ |
| 1 | 0.73 | 34 | 0.62 | 27 |
| 2 | 0.78 | 17 | 0.61 | 20 |
| 3 | 0.72 | 45 | 0.59 | 44 |
| 4 | 0.67 | 45 | 0.65 | 41 |
| 5 | 0.62 | 39 | 0.60 | 39 |
| 6 | 0.63 | 50 | 0.61 | 54 |
| 7 | 0.74 | 46 | 0.65 | 51 |
| 8 | 0.70 | 48 | 0.64 | 52 |
| 9 | 0.62 | 70 | 0.61 | 74 |
| ref. | 0.83 | 100 | 0.61 | 100 |

*Table 4.13: Spatial dependence of the spin density ($M_0$) and the $T_{2H}$ and $T_{1H}$ relaxation times after unloading for the Bl-oc2 blend. The spatial locations are indicated in Figure 4.29. The averaged 95% confidence limit for $T_{1H}$, $T_{2H}$ and $M_0$ is about 5%, 8% and 8%, respectively.*

However, while the degree of cavitation drops towards the borders of the deformation zone, the degree of stress induced chain elongation seems to be spatially independent in the damage zone. It is suggested that the physical/topological constraints, introduced by the occlusions, results in a different deformation mechanism in which the load bearing capacity of the rubbery chains has an important contribution. A deformation mechanism in which the rubber particles not only promote cavitation but moreover carry a load bearing capacity can explain the improved toughness of the occluded blends. Although Bl-oc1 has a similar volume fraction of dispersed phase (but less rubber) as compared to Bl-st, an improvement in impact strength of about 12 kJ/m$^2$ is reached at a similar particle size distribution. Although the increased volume fraction of dispersed phase in Bl-oc2 will certainly contribute to the improved toughness of this blend,[162] a high impact strength of 78 kJ/m$^2$ is obtained despite of the broad particle size distribution.

#### 4.4.3.3 Conclusion

This MRI study indicates a difference in the deformation mechanism for extruded PA6-EPM-*g*-MA blends with and without PA6 occlusions in the rubbery phase. Stress induced elongation of the rubbery chains, caused by physical and topological constraints results in an improved impact strength for the occluded blends that originates from the load bearing capacity of the rubbery chains as is demonstrated by the localised $T_{2H}$ decay times. The toughness of the occluded type blends is not solely provided by simple rubber cavitation, which can be quantified by means of the localised proton spin density, but is significantly enhanced by a more pronounced delocalisation of the local strain as a result of favourable conditions for stress induced chain elongation of the rubbery chains.

Positron annihilation lifetime spectroscopy (PAL) would be a possible nondestructive technique to investigate the size of the cavities.[163]

## 4.5 Overall conclusion

The spin-warp NMR imaging technique has been demonstrated to be a useful method to study the damage behaviour under load of rubber toughened materials. Three different types of materials have been studied showing remarkable differences in the material response towards stress.

The image contrast in the damage bands of ABS has been shown to originate from a reduction in the spin density due to severe rubber particle cavitation. The damage bands remain present upon unloading and only a minor recovery in the density of the material has been determined. The spatial independence of the $T_{2H}$ relaxation time demonstrates that no significant elongation of the rubbery chains takes place under load.

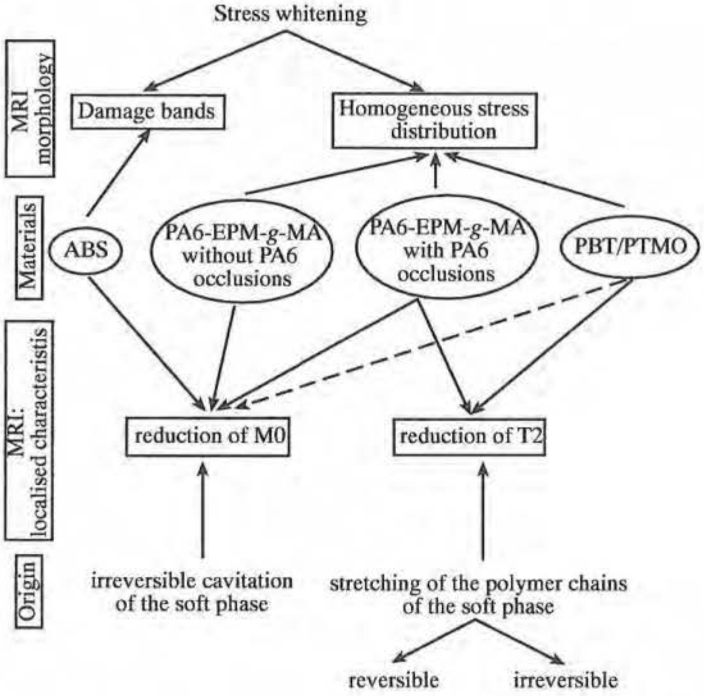

*Scheme 4.1: Schematic overview of the experimental MRI results obtained for the four studied rubber toughened materials.*

For the PBT/PTMO block copolymer a reduction of the chain mobility in combination with a minor reduction of the spin density near the crack tip has been detected. The elongation of the rubbery chains under load almost completely vanishes upon unloading while the decrease in $M_0$, due to cavitation of the rubber particles, remains present in the immediate surrounding of the crack tip.

A different deformation mechanism for two types of PA6-EPM-*g*-MA blends has been determined by NMR imaging. For the Bl-st blend no chain elongation has been detected while for the Bl-oc2 blend the $T_2$ relaxation time became spatial dependent. This irreversible stress induced elongation of the rubbery chains has been shown to be the major reason for the improved toughness.

An overview is presented in the scheme 4.1.

## 4.6 Experimental part

### 4.6.1 Materials

The ABS, PBT/PTMO and PA6/EPM-*g*-MA blends are obtained from DSM Geleen. MRI measurements were accomplished on rectangular plates with a dimension of 40 x 12.8 x 3.25 mm. The samples were sawn out of an original injection moulded plate of 120 x 12.8 x 3.25 mm. The plates were sharply notched (4mm in depth) perpendicular to the strain direction (z) to obtain the condition of a growing crack. Loading of the notched plates was accomplished in a 'home-developed' stretching device (see part 4.2.2.2) that fits in the MRI probe head.

### 4.6.2 MRI experiments

*Pulse sequence*

The Hahn-echo pulse sequence, used to acquire the MRI images is represented in Figure 4.31.[142,164,165]

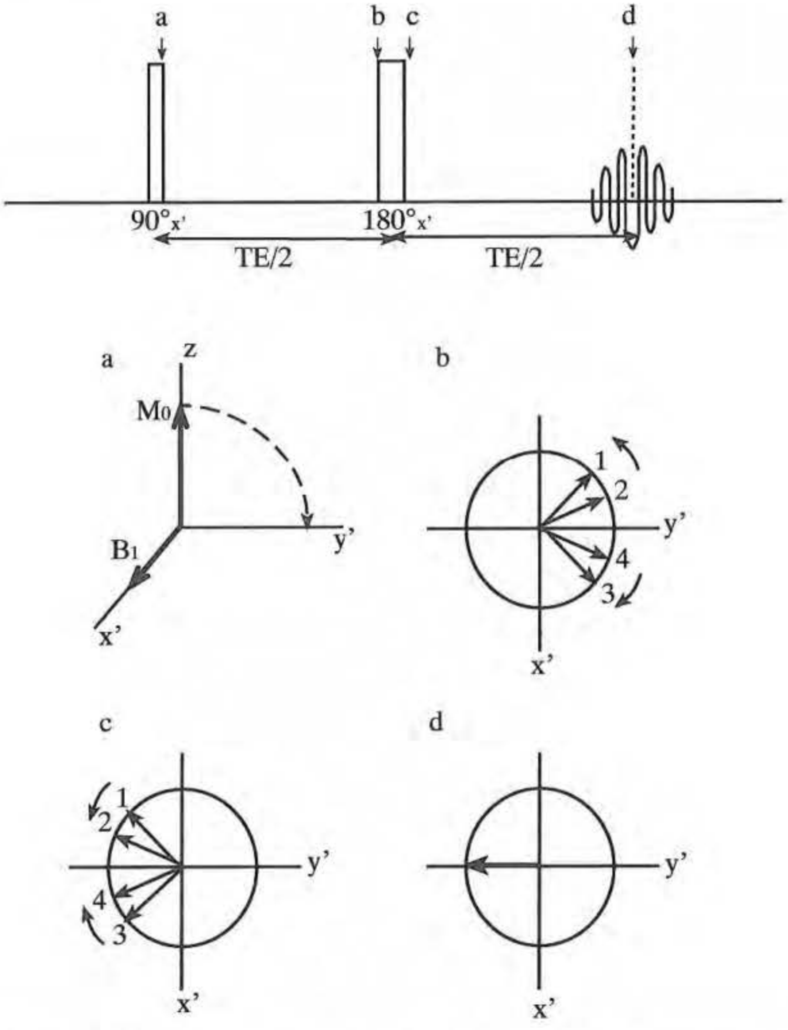

*Figure 4.31: Schematic representation of the Hahn-echo pulse sequence.*

The magnetisation is excited by a 90° pulse and brought into the x'y'-plane (Figure 4.31a). After application of the $90_{x'}^{\circ}$ pulse, the spins start to dephase (Figure 4.31b). After a period of dephasing, TE/2, a 180° refocusing pulse along the x' direction, is applied (Figure 4.31c). The isochromats continue to move in their original sense and so rephase along the negative y'-axis after a further time TE/2 (Figure 4.31d). The echo amplitude M(TE) then seen will be reduced in amplitude by an amount that depends solely on the natural $T_2$. As the time TE/2 between the pulses is varied, the amplitude of the echo, will vary as:

$$M(TE) = M_0 \ e^{-TE/T_2} \tag{4.4}$$

The time between two successive 90° pulses is the repetition time (TR). For a constant TE and a varying TR, the amplitude of the echo is described as follows:

$$M(TR) = M_0 \ (1 - e^{-TR/T_1}) e^{-TE/T_2} \tag{4.5}$$

*Parameters*

$^1$H MRI spin-echo images are generated at 9.4 T on an Inova 400 Varian vertical bore spectrometer with a spin-warp pulse sequence in a micro-imaging probe with a coil of 16 mm in diameter. The sample was positioned such that the static magnetic field $B_0$ was parallel to the straining direction (Figure 4.6).

Images of ABS are acquired with an echo time (TE) of 1.51 ms and a repetition delay (TR) of 1 s and a field of view (FOV) of 16 x 20 mm. The images with different gradient orientations and those acquired as a function of increasing load have an in-plane pixel resolution of 100 x 100 μm and a slice thickness of 3.25 mm (48 accumulations). The images used for the quantitative analysis of $M_0$, $T_2$ and $T_1$ have an in-plane pixel resolution of 66 x 66 μm and a slice thickness of 1.625 mm.

Images of PBT/PTMO are acquired with TE = 1.05 ms and TR = 1 s, have an in-plane resolution of 100 x 100 μm, a FOV of 16 x 20 mm, a slice thickness of 2 mm and 100 accumulations. Slice selective images were always taken nicely in the centre of the plates by tuning the offset frequency in the slice direction. Typical gradient strengths used were 30.8 G/cm, 13.2 G/cm and 25.9 G/cm for phase, read and slice direction, respectively.

All images of the PA6/EPM-*g*-MA blends have an inplane pixel resolution of about 120 x 120 μm in a field of view of 16 x 20 mm. A spin-warp pulse sequence with a repetition delay (TR) of 3 s and an echo time (TE) of 1.1 ms was used. Image slices of 2.5 mm in thickness were selected in the middle of the specimen by tuning the offset frequency in the slice direction. Typical gradient strengths used were 27 G/cm, 8 G/cm and 18 G/cm for phase, read and slice direction, respectively.

The determination of the $T_{2H}$ relaxation time as a function of the angle between the strain direction and the static magnetic field $B_0$ was accomplished on a small rectangular specimen, cut in the proximity of the crack tip, by analysing the intensity of 1D projections as a function of TE (15 values between 1.1 ms and 2ms).

All type of materials used in this study consists of a rigid and a soft, rubbery phase. All images selectively visualise the rubber phase since transverse magnetisation of the rigid matrix decays to zero within 100 μs. The bi-exponential $T_2$ relaxation behaviour of these materials, due to glassy polymer and rubbery phase, is filtered by the rather long spin-echo time (TE).

### 4.6.3 Tensile strength tests

The tensile strength tests were performed at a Zwick tensile testing machine. The tests on ABS samples were executed at an elongation rate of 10 mm/min and at 1 mm/min. All tests on the nylon/rubber blends were done with an elongation rate of 50 mm/min. All tests were performed at room temperature.

### 4.6.4 Scanning electron microscopy

Specimens for scanning electron microscopy were prepared from loaded samples that were used for the MRI experiments. To view the morphology of the damage zone, the surface was coated with carbon and examined in a Philips XL30FEG Scanning Electron Microscope.

### 4.6.5 Transmission electron microscopy

The morphology of undeformed PA6-EPM-*g*-MA specimens was studied by means of transmission electron microscopy at DSM Geleen. Samples were trimmed and subsequently stained with a 1:1 $OsO_4$/formaline mixture. Sections of 70 nm were cut at -110 °C and studied in a Jeol 2000FX transmission electron microscope.

### 4.6.6 Impact tests

The notched charpy impact tests were executed at DSM Geleen, according the ISO 179 standard at 23°C and at -30°C.

## 4.7 References

1 Sperling, L.H. *'Introduction to physical polymer science'*, John Wiley & Sons, Inc.; New York (1992).

2 Hsiao, C.C.; Sauer, J.A. *J. Appl. Phys.* **1950**, 21, 1071.

3 Kambour, R.P. *Polymer* **1964**, 5, 143.

4 Beahan, P.; Bevis, M.; Hull, D. *Phil. Mag.* **1971**, 24, 1267.

5 Lauterwasser, B.D.; Kramer, E.J. *Phil. Mag. A* **1979**, 39, 469.

6 Kramer, E.J. *Adv. Polym. Sci.* **1983**, 52 (1), 1.

7 Van Krevelen, D.W. *'Properties of Polymers'* Elsevier Science Publishers B.V., Amsterdam, (1990).

8 Maxwell, B.; Rahm, L.F. *J. Soc. of Plastics Eng.* **1965**, 6, 473.

9 Argon, A.S.; Hannoosh, J.G. *Phil. Mag.* **1977**, 36, 1195.

10 Wellinghoff, S.; Baer, E. *J. Macromol. Sci.-Phys.* **1975**, B11, 367.

11 Kawagoe, M.; Kitagawa, M. *J. Polymer Sci.-Polymer Phys.* **1981**, 19, 1423.

12 Gent, A.N. *J. Materials Sci.* **1970**, 5, 925.

13 Argon, A.S. *J. Macromolec. Sci. B* **1973**, 8, 573.

14 Argon, A.S.; Salama, M.M. *Mat. Sci. & Eng'rg.* **1977**, 23, 219.

15 Taylor, G.I. *Proc. Roy. Soc. A* **1950**, 201, 192.

16 Saffman, P.G.; Taylor, G.I. *Proc. Roy. Soc. A* **1950**, 245, 312.

17 Donald, A.M.; Kramer, E.J. *Phil. Mag. A* **1981**, 43, 857.

18 Bucknall, C.B. *'Toughened Plastics'*, Applied Science Publishers, London, (1977).

19 Verheulpen-Heymans, N.; Bauwens, J.C. *J. Mat. Sci.* **1976**, 11, 7.

20 Verheulpen-Heymans, N. *Polym. Eng. and Sci.* **1984**, 24, 10,809.

21 Cawood, M.J.; Channell, A.D.; Capaccio, G. *Polymer* **1993**, 34, 423.

22 O' Connell, P.A.; Bonner, M.J.; Duckett, R.A.; Ward, I.M. *Polymer* **1995**,36, 12, 2355.

23 Döll, W. *Adv. Polym. Sci.* **1983**, 52 (3), 105.

24 Donald, A.M.; Kramer, E.J.; Bubeck, R.A. *J. Polymer Sci.-Polymer Phys.* **1982**, 20, 1129.

25 Trent, J.S.; Palley, I.; Baer, E. *J. Mat. Sci.* **1981**, 16, 331.

26 Wright, D. *'Environmental Stress Cracking of Plastics'* Rapra Technology LTD., United Kingdom, (1996).

27 Lagaron, J.M.; Dixon, N.M.; Reed, W.; Pastor, J.M.; Kip, B.J. *Polymer* **1999**, 40, 2569.

28 Turnbull, A.; Maxwell, A.S.; Pillai, S. *J. of Mat. Sci.* **1999**, 34, 451.

29 Ulrich, J.; Brion, H.-G.; Kirchheim, R. *Polymer* **1999**, 40, 1807.

30 Sauer, J.A.; Chen, C.C. *Adv. Polym. Sci.* **1983**, 52 (4), 169.

31 Yang, A.-C. M.; Kramer, E.J.; Kuo, C.C.; Phoenix, S.L. *Macromolecules* **1986**, 19, 2010.

32 Yang, A.-C. M.; Kramer, E.J.; Kuo, C.C.; Phoenix, S.L. *Macromolecules* **1986**, 19, 2020.

33 Brown, H.R. *Macromolecules* **1991**, 24, 2752.

34 Brown, H.R.; Ward, I.M. *Polymer* **1973**, 14, 468.

35 Hui, C.Y.; Ruina, A.; Creton, C.; Kramer, E.J. *Macromolecules* **1992**, 25, 3948.

36 Sha, Y.; Hui, C.Y.; Ruina, A.; Kramer, E.J. *Macromelecules* **1995**, 28, 2450.

37 Marissen, R. *Polymer* **2000**, 41, 1119.

38 Kim, J.K.; Robertson, R.E. *J. of Mat. Sci.* **1992**, 27, 161.

39 Young, R.J.; Beaumont, P.W.R. *J. of Mat. Sci.* **1977**, 12, 684.

40 Kinloch, A.J.; Maxwell, D.L.; Young, R.J. *J. of Mat. Sci.* **1985**, 20, 3797.

41 Merz, E.H.; Claver, G.C., Baer, M.J. *J. Polym. Sci.* **1956**, 22, 325.

42 Schmitt, J.A.; Keskkula, H. *J. Appl. Polym. Sci.* **1960**, 3, 132.

43 Newman. S; Strella,S. *J. Appl. Polym. Sci.* **1965**, 9, 2297.

44 Kambour, R.P. *Macromolec. Rev.* **1971**, 7, 134.

45 Bucknall, C.B.; Smith, R.R. *Polymer* **1965**, 6,437.

46 Elias, H.G. *'An Introduction to Plastics'* VCH Publishers, Inc., New York, 1993.

47 Matsuo,M. *Polymer* **1966**, 7, 421.

48 Kambour, R.P. *J. Polym. Sci.: Macromolecular Rev.* **1973**, 7, 1.

49 Bucknall, C.B.; Yoshii, T. *Br. Polym. J.* **1978**, 10, 53.

50 Bucknall, C.B.; Clayton, D. *J. Mater. Sci.* **1972**, 7,202.

51 Bucknall, C.B.; Clayton, D.; Keast, W.E. *J. Mater. Sci.* **1972**, 7, 1443.

52 Bucknall, C.B.; Clayton, D.; Keast, W.E. *J. Mater. Sci.* **1973**, 8, 514.

53 Bucknall, C.B.; Drinkwater, I.C. *J. Mater. Sci.* **1973**, 8, 1800.

54 Breuer, H.; Haaf, F.; Stabenow, J. *J. Macromol. SCi.-Phys.* **1977**, B14(3), 387.

55 Maxwell, M.A.; Yee, A.F. *Polym. Eng. and Sci.* **1981**, 21, 4, 205.

56 Bascom, W.D.; Cottington, R.L.; Jones, R.L.; Peyser, P. *J. Appl. Polym. Sci.* **1975**, 19, 2545.

57 Bascom, W.D.; Cottington, R.L. *J. Adhesion* **1976**, 7, 333.

58 Bascom, W.D.; Ting, R.Y.; Moulton, R.J.; Riew, C.K.; Siebert, A.R. *J. Mat. Sci.* **1981**, 16, 2657.

59 Kinloch, A.J.; Shaw, S.J.; Tod, D.A.; Hunston, D.L. *Polymer* **1983**, 24, 1341.

60 Huang, Y.; Kinloch, A.J. *J. Mat. Sci. Letters* **1992**, 11, 484.

61 Yee, A.F.; Olszewski, W.V.; Miller, S. *ACS, Adv. Chem. Ser.* **1976**, 154, 97.

62 Yee, A.F. *J. Mat. Sci.* **1977**, 12, 757.

63 Maxwell, M.A.; Yee, A.F. *Polym. Eng. and Sci.* **1981**, 21, 4, 205.

64 Kunz-Douglas, S.; Beaumont, P.W.R.; Ashby, M.F. *J. Mat. Sci.* **1980**, 15, 1109.

65 Wu, S. *J. Polym. Sci., Polym. Phys. Edn.* **1983**, 21, 699.

66 Yee, A.F.; Pearson, R.A. *J. Mat.Sci.* **1986**, 21, 2462.

67 Pearson, R.A.; Yee, A.F. *J. Mat.Sci.* **1986**, 21, 2475.

68 Pearson, R.A.; Yee, A.F. *J. Mat.Sci.* **1991**, 26, 3828.

69 van der Sanden, M.C.M.; Kok, J.M.M.; Meijer, H.E.H. *Polymer* **1994**, 35, 2995.

70 Magalhaes, A.M.L.; Borggreve, R.J.M. *Macromolecules* **1995**, 28, 5841.

71 Ramsteiner, F.; Heckmann, W. *Polymer* **1985**, 26, 199.

72 Borggreve, R.J.M.; Gaymans, R.J.; Schuijer, J.; Ingen Housz, J.F. *Polymer* **1987**, 28, 1489.

73 Muratoglu, O.K.; Argon, A.S.; Cohen, R.E.; Weinberg, M. *Polymer* **1995**, 36, 25, 4771.

74 Giaconi, G.F.; Castellani, L.; Maestrini, C.; Riccò, T. *Polymer* **1998**, 39, 25, 6315.

75 Ayre, D.S.; Bucknall, C.B. *Polymer* **1998**, 39, 20, 4785.

76 Bucknall, C.B.; Rizzieri, R.; Moore, D.R. *Polymer-Letchwork* **2000**, 41, 11, 4149.

77 Smit, R.J.M. *'Toughness of heterogeneous polymeric systems, a modeling approach'* Ph. D. Thesis, Eindhoven University of Technology, June 1998.

78 Sultan, J.N.; Laible, R.C.; McGarry, F.J. *Appl. Polym. Symp.* **1971**, 16, 127.

79 Sultan, J.N.; McGarry, F.J. *J. Polym. Sci.* **1973**, 13, 29.

80 Hobbs, S.Y.; Bopp, R.C.; Watkins, V.H. *Polym. Eng. and Sci.* **1983**, 23, 7, 380.

81 Wu, S. *Polym. Int.* **1992**, 29, 229.

82 van der Wal, A.; Mulder, J.J.; Oderkerk, J.; Gaymans, R.J. *Polymer* **1998**, 39, 26, 6781.

83 Donald, A.M.; Kramer, E.J. *J. Appl. Polym. Sci.* **1982**, 27, 3729.

84 Donald, A.M.; Kramer, E.J. *J. Mat. Sci.* **1982**, 17, 2351.

85 Wu, S. *Polymer* **1985**, 26, 1855.

86 Jang, B.Z.; Uhlmann, D.R.; van der Sande, J.B. *Polym. Eng. Sci.* **1985**, 25, 10, 643.

87 Oshinski, A.J.; Keskkula, H.; Paul, D.R. *Polymer* **1992**, 33, 2, 268.

88 Cimmino, S.; D'Orazio, L.; Greco, R.; Maglio, G.; Malincinico, M.; Mancarella, C.; Martuscelli, E.; Palumbo, R.; Ragosta, G. *Polym. Eng. and Sci.* **1984**, 24, 1, 48.

89 D'Orazio, L.; Mancarella, C.; Martuscelli, E. *J. Mat. Sci.* **1988**, 23, 161.

90 Dompas, D.; Groeninckx, G. *Polymer* **1994**, 35,22,4743.

91 Steenbrink, A.C.; Litvinov, V.M.; Gaymans, R.J. *Polymer* **1998**, 39, 20, 4817.

92 Cho, K.; Yang, J.; Park, C.E. *Polymer* **1998**, 39, 14, 3073.

93 Dompas, D.; Groeninckx, G.; Isogawa, M.; Hasegawa, T.; Kadokura, M. *Polymer* **1994**, 35, 22, 4750.

94 Dompas, D.; Groeninckx, G.; Isogawa, M.; Hasegawa, T.; Kadokura, M. *Polymer* **1995**, 36, 2, 437.

95 Donald, A.M.; Kramer, E.J. *J. Mat. Sci.* **1982**, 17, 1765.

96 Bucknall, C.B.; Stevens, W.W. *J. Mat. Sci.* **1980**, 15, 2950.

97 Borggreve, R.J.M.; Gaymans, R.J. *Polymer* **1989**, 30, 63.

98 Borggreve, R.J.M.; Gaymans, R.J.; Schuijer, J. *Polymer* **1989**, 30, 71.

99 Borggreve, R.J.M.; Gaymans, R.J.; Eichenwald, H.M. *Polymer* **1989**, 30, 78.

100 Thomas, S.; Groeninckx, G. *Polymer* **1999**, 40, 5799.

101 Dedecker, K.; Groeninckx, G. *Macromolecules* **1999**, 32, 2472.

102 Dijkstra, K.; Laak, J.; Gaymans, R.J. *Polymer* **1994**, 35, 315.

103 Lazzari, A.; Bucknall, C.B. *J. Mat. Sci.* **1993**, 28, 6799.

104 Bucknall, C.B.; Karpodinis, A.; Zhang, X.C. *J. Mat. Sci.* **1994**, 29, 3377.

105 Lazzari, A.; Bucknall, C.B. *Polymer* **1995**, 36, 15, 2895.

106 Bucknall, C.B.; Soares, V.L.P.; Yang, H.H.; Zhang, X.C. *Macormol. Symp.* **1996**, 265.

107 Lin, C.S.; Ayre, D.S.; Bucknall, C.B. *J. Mat. Sci. Leeters* **1998**, 17, 669.

108 Bucknall, C.B.; Hall, M.M. *J. Mat. Sci.* **1971**, 6,95.

109 Wu, S. *J. Appl. Pol. Sci.* **1988**, 35, 549.

110 Oxborough, R.J.; Bowden, P.B. *Phil. Mag.* **1974**, 30, 171.

111 Dao, K.C. *J. Appl. Polym. Sci.* **1982**, 27, 4799.

112 Schwier, C.E.; Argon, A.S.; Cohen, R.E. *Polymer* **1985**, 26, 1985.

113 Pearson, R.A.; Bagheri, R. *J. Mat. Sci.* **1996**, 31, 3945.

114 Ostromislensky, I.I. (to Naugatuck Chem.), US Pat. 1, 613, 673 (11 Jan. 1927).

115 Amos; J.L. *Polym. Engng. Sci.* **1974**, 14, 1.

116 Gilbert, D.G.; Donald, A.M. *J. Mat. Sci.* **1986**, 21, 1819.

117 O'Connor, B.; Bucknall, C.B.; Hahnfeld, J.L. *Plastics, Rubber and Composites Processing and Applications* **1997**, 26, 8, 360.

118 Bucknall, C.B.; Davies, P.; Partridge, I.K. *J. Mat. Sci.* **1987**, 22, 1341.

119 Daly, L.E. (to US Rubber), US Pat. 2, 439, 202 (6 Apr. 1948).

120 Beahan, P.; Thomas, A.; Bevis, M. *J. Mat. Sci.* **1976**, 11, 1207.

121 Dover, I.R.; Smith, I.O.; Chadwick,G.A. *J. Mat. Sci.* **1977**, 10, 1176.

122 Nusbaum, H.J. *J. Mat. Sci. Letters* **1979**, 14, 2755.

123 Gilchrist, A.; Mills, N.J. *J. Mat. Sci.* **1987**, 22, 2397.

124 Newmann, L.V.; Williams, J.G. *J. Mat. Sci.* **1980**, 15, 773.

125 Sridharan, N.S.; Broutman, L.J. *Polym. Eng. Sci.* **1982**, 22, 12 760.

126 Bucknall, C.B.; Ayre, D.S.; Dijkstra, D.J. *Polymer* **2000**, 41, 5937.

127 van der Vegt, A.K. *'Polymeren van keten tot kunststof'*; Delfste Universitaire Pers, Delft, (1996).

128 Bhattacharya, S.K.; Brown, N. *J. Mat. Sci.* **1984**, 19, 2519.

129 Sugimoto, M. Ishikawa, M.; Hatada, K. *Polymer* **1995**, 36, 19, 3675.

130 Liang, J.Z.; Li, R.K.Y. *J. Appl. Pol. Sci.* **2000**, 77, 409.

131 Gesner, B.D. *J. Appl. Pol. Sci.* **1967**, 11, 2499.

132 Garg, A.C.; Mai, Y.W. *Composites Science and Technology* **1988**, 179.

133 Franco, M.; Mondragon, I.; Bucknall, C.B. *J. Appl. Pol. Sci.* **1999**, 72, 427.

134 Bucknall, C.B.; Heather, P.S.; Lazzeri, A. *J. Mater. Sci.* **1989**, 16, 2255.

135 Bucknall, C.B.; Lazzeri, A. *J. Mater. Sci.* **2000**, 35,427.

136 Speroni, F.; Castoldi, E.; Fabbri, P.; Casiraghi, T. *J. Mat. Sci.* **1989**, 24,2165.

137 Majumbar, B.; Keskula, H.; Paul, D.R. *Polymer* **1994**, 35, 1399.

138 Riemslag, T. *'Crack Growth in Polyethylene'*, Ph.D. Thesis, Delft University of Technology, June 1997.

139 Riemslag, A.C. *Journal of Testing and Evaluation, JTEVA* **1994**, 22,410.

140 Dickinson, J.T.; Jensen, L.C.; Langford, S.C.; Dion,R.P. *J Pol. Sci.: Part B: Polymer* Physics 1993, 31, 1441.

141 Blümich, B.; Kuhn, W. Eds *'Magnetic Resonance Microscopy : Methods and Applications in Materials Science, Agriculture and Biomedicine'* VCH Publishers: New York, (1992).

142 Callaghan, P.T. *'Principles of Nuclear Magnetic Resonance Microscopy'*. Clarendar Press: Oxford, 1991.

143 Weigand, F.; Spiess, W. H. *Macromolecules* **1995**, 28, 6361.

144 Blümler, P.; Blümich, B. *Acta Polymerica* **1993**, 44, 125.

145 Traub, B.; Hafner, S.; Wiesner, U.; Spiess, H. W. *Macromolecules* **1998**, 31, 8585.

146 Günther, E.; Blümich, B.; Spiess, H.W. *Macromolecules* **1992**, 25, 3315.

147 Hepp, M.A.; Miller, J.B. *J.Magn. Res. A* **1994**, 111, 62.

148 Klinkenberg, M.; Blümler, P.; Blümich, B. *Macromolecules* **1997**, 30, 1038.

149 Hauck, D.; Blümler, P.; Blümich, B. *Macromol. Chem. Phys.* **1997**, 198, 2729.

150 Kuhn, W. *Angew. Chemie Int. E.D. Engl.* **1990**, 29, 1.

151 A driaensens, P.; Pollaris, A.; Vanderzande, D.; Gelan, J.; White, J.L.; Dias, A.J.; Kelchtermans, M. *Macromolecules* **1999**, 32, 4692.

152 Ercken, M.; Adriaensens, P.; Vanderzande, D.; Gelan, J. *Macromolecules* **1995**, 28, 8541.

153 Adriaensens, P.; Storme, L.; Carleer, R.; Vanderzande, D.; Gelan, J.; Litvinov, V. M.; Marissen, R. *Macromolecules* **2000**, 33,4836.

154 Weigand, F.; Hafner, S.; Spiess, H. W. *J. Magn. Reson.* **1996**, 120, 201.

155 Liu, J.; Nieminen, A.O.; Koenig, J. L. *J. Magn. Reson.* **1989**, 85, 95.

156 Bucknall, C.B., Chapter 22 in *'Polymer Blends: Formulation and Performance'*, eds D.R. Paul and C.B. Bucknall, Wiley, New York, 1999.

157 Schmidt, A.; Veeman, W.S.; Litvinov, V.M.; Gabriëlse, W. *Macromolecules* **1998**, 31, 1652.

158 Soliman, M. private communication.

159 Adriaensens, P.; Storme, L.; Carleer, R.; D'Haen, J.; Gelan, J.; Litvinov, V. M.; Marissen, R.; Crevecoeur, J. *Macromolecules* accepted august **2001**.

160 Ishikawa, M. *Polymer* **1995**, 36, 2203.

161 Schneider, M.; Demco, D.E.; Blümich, B. *Macromolecules* **2001**, 34, 4019.

162 Litvinov, V. M.; Steeman, P. A. M. *Macromolecules* **1999**, 32, 8476

163 Simon, G.P. *Trends in Polym. Sci.* **1997** 5, 394.

164 Hahn, E.L. *Phys. Rev.* **1950**, 80,580.

165 Foster, M.A.; Haase, A. *'Relaxation measurements in imagign studies' Enclyclopedia of Nuclear Magnetic Resonance* 4034-4041 (1996).

# 5

# Summary, general conclusions and perspectives

In this work, the possibilities of NMR relaxometry are exploited to study the molecular mobility and morphology of different multidomain polymer systems with liquid and solid state NMR and MRI.

The gelation mechanism of polymers is investigated in the liquid state. The complex multidomain behaviour of segmented networks and blends is examined with solid state NMR. NMR imaging reveals localised information of the polymer chains in the damage zone in polymers under mechanical load.

Chapter one represents a brief overview of the basic principles of NMR microscopy and relaxometry.

In chapter two the gelation mechanism of syndiotactic poly(methyl methacrylate) (sPMMA) in toluene is examined in detail by means of $^{13}C$ liquid state NMR. A two step gelation mechanism is proposed for the gelation in the literature. By cooling down a mixture of sPMMA in toluene a coil-to-helix transition is observed in a first step followed by an association of the helices to form the physical junctions in the gel. These observations are confirmed by FTIR analysis published by other research groups. A line width analysis of NMR resonances as a function of temperature clearly demonstrated the transition region from coil to helix although a quantification of the fraction incorporated in the helix conformation couldn't be executed.

The NMR relaxometry provided a quantification of the fractions with different molecular mobility by means of an extensive spin-spin relaxation time ($T_2$) investigation. For atactic PMMA (aPMMA) in toluene, which is used as a reference system, one $T_2$ decay time is observed for the $\alpha$-methyl groups. For sPMMA on the other hand, two $T_2$ relaxation times (and corresponding fractions) are obtained for the $\alpha$-methyl signal in a temperature range up to 50 °C. The additional $T_2$ relaxation time, representing a fraction of 25%, could be assigned to the $\alpha$-methyl groups incorporated in the helical structures, since the helical structures only exist for sPMMA up to 50 °C. For the methoxy signal of aPMMA two $T_2$ decay times (and corresponding fractions) are observed in the whole temperature range up to 80 °C). For sPMMA three $T_2$ relaxation times are observed for the methoxy signal in a temperature range up to 50 °C. The additional one as compared to aPMMA is ascribed to the methoxy groups in helix conformation in agreement with the results of the $\alpha$-methyl groups. An investigation of aPMMA in $CDCl_3$ (good solvent) allowed to assign the additional $T_2$ relaxation time for the methoxy groups, as compared to the $\alpha$-methyl groups, (with intermediate mobility), to the ester groups which are immobilised by intermolecular polymer-polymer interactions.

Besides the quantification of the helix phase, the presented $T_2$ relaxation time study has been used to calibrate a FTIR method for the quantification of the amount of helical phase. It has been shown that NMR relaxometry in the liquid state can have an important contribution in the explanation of the gelation mechanisms of polymer systems.

In the third chapter, a comparative relaxometry study in the solid state is performed on poly(1,3-dioxalane)/poly(methyl methacrylate) (PDXL/PMMA) segmented networks and corresponding blends with different PDXL weight fractions (namely 20%, 40% and 60%). The study on the morphology is performed by means of the spin-lattice ($T_{1H}$) and the spin-lattice in the rotating frame ($T_{1\rho H}$) relaxation times. A homogeneous phase morphology on a scale of 20 nm is indicated by the same $T_{1H}$ relaxation time for both constituents (PDXL and PMMA) in the segmented networks and in the blend with the lowest PDXL fraction. An increase of the PDXL fraction in the polymer blends leads to a heterogeneous phase morphology on the $T_{1H}$ scale (domains larger than 20 nm). The examination of the $T_{1\rho H}$ relaxation times shows phase separation on a smaller scale. For the phase separated amorphous PDXL domains, two decay times are observed for the networks and the blend with 20 wt % PDXL. A fraction of the amorphous PDXL is submitted to spin diffusion with PMMA due to the immobilisation of the PDXL chains by the rigid PMMA chains. This results in two $T_{1\rho H}$ decay times for PDXL: one similar to this of PMMA and another observed for the amorphous phase. It means that for the segmented networks and the blend with 20 % PDXL, small PDXL domains with an estimated size between 1 nm ($T_{1\rho H}$) and 20 nm ($T_{1H}$) are present in the PMMA continuous phase.

For the blends with a higher PDXL fraction one $T_{1\rho H}$ relaxation time is assigned to amorphous PDXL while the second could be dedicated to crystalline PDXL domains larger than 1-2 nm in size. The appearance of the crystalline phase is confirmed by means of DSC. The phase behaviour of these systems is also reflected in the DMA and TGA analysis.
This detailed comparative phase behaviour study clearly demonstrated the forced compatibility of both components in this unique type of segmented network architecture. Knowledge about the nanometer morphology has become a hot topic in view of developing those high-tech materials whose properties and applications rely especially on the specific nanometer morphology of the network. NMR relaxometry has been proving to yield very useful information concerning the nanometer morphology of polymer networks and blends in the bulk.

The fourth chapter concerns a MRI relaxometry study, which allows to obtain localised information about cavitation and molecular chain mobility and cavitation induced by mechanical load. The pre-cracked specimens were mechanically loaded to yield stress in a stretching device that fits into the probe head. The four materials studied in this work contain a rigid matrix and a soft, elastomeric phase. Only the soft phase is visualised in the MRI images acquired with a spin-echo pulse sequence since the transverse magnetisation of the rigid matrix decays to zero before the echo can be detected.
Under conditions of critical load, sharply localised damage bands appear in the images of ABS, a blend of poly(styrene-co-acrylonitrile) (SAN) with 28 wt % SAN grafted polybutadiene (PB). These damage bands are visualised in detail in the MRI images. Spatial resolved determination of the spin density and the $T_2$ and $T_1$ relaxation times clearly indicates that the damage bands in ABS mainly arise from a strong decrease in material density caused by severe rubber particle cavitation.
The second material investigated by MRI is a block copolymer of polybutadiene/poly(tetramethylene oxide) (PBT/PTMO). This material reveals a more continuous, largely extended stress distribution as compared to ABS. The spatial dependent analysis of the spin density and the relaxation times indicated a significant decrease of the molecular mobility (decrease of $T_2$) of the elastomeric chains under load. This is explained by chain alignment of PTMO chains and is confirmed by solid state NMR measurements under load.

The third kind of material studied in this work, is a blend of polyamide 6 (PA6) blended with maleic anhydride grafted ethylene-propylene rubber (EPM-*g*-MA). Two different types of this blend are studied, one with pure EP rubber particles dispersed in the PA6 matrix (Bl-st) while the other contains PA6 occlusions in the dispersed rubbery phase (Bl-oc2). A different material behaviour under load is observed: while the Bl-oc2 shows both cavitation of the rubber particles and some irreversible chain alignment of the rubbery chains, the Bl-st only shows cavitation.

It is shown that spin-echo NMR imaging provides information on cavitation, the local strain distribution and variations in the local chain mobility under mechanical load. The material characteristics on a molecular level, like the detected cavitation and chain alignment under load, can be related with macroscopic material behaviour like toughness and impact strength. This relation can contribute to an optimisation of the material properties limited by the synthesis pathway on the molecular scale.

With this imaging technique only the soft, elastomeric phase in these polymer materials is detected. To image the matrix or rigid phase, techniques like single point imaging have to be used. Better quantitative accordance with the stress-strain measurements on a tensile testing machine can be obtained by an optimisation of the stretching device. To decrease the friction between the copper screws and between the screw and the nut, a ball bearing surface has to be incorporated in the device. To avoid friction with the glass tube, a broader tube compared to the sample size has to be used.

NMR relaxometry has been demonstrated to be a versatile, non-invasive and non-destructive technique to obtain information about the molecular mobility and the morphology of polymer materials in the bulk as well in the liquid as in the solid state. MRI on the other hand reveals localised information about these nanometer-scale material characteristics.

# 6

# Samenvatting, algemeen besluit en perspectieven

In deze thesis werden de moleculaire dynamica en de morfologie van verschillende multifase polymeer systemen bestudeerd met NMR relaxometrie. Een onderzoek naar het geleringsmechanisme van een polymere gel is uitgevoerd in de vloeibare fase. Met vaste stof NMR is de morfologie van gesegmenteerde netwerken en de analoge mengsels uitgebreid onderzocht. NMR beeldvorming van verschillende polymere materialen onder mechanische belasting leverde gelokaliseerde informatie over de mobiliteit van de ketens en over de materiaal dichtheid in de beschadigde zone voor de breuk.

In hoofdstuk één worden de basisprincipes van NMR en relaxometrie beknopt uitgelegd. Hoofdstuk twee behandelt het geleringsmechanisme van syndiotactisch poly(methyl methacrylaat) (sPMMA) in tolueen, onderzocht met $^{13}C$ vloeistof NMR. Een twee-staps mechanisme voor deze gelering was reeds voorgesteld in de literatuur. Bij het afkoelen van een oplossing van sPMMA in tolueen werd in de eerste stap een overgang van een keten naar een helix structuur vastgesteld, gevolgd door een associatie van de helices tot het vormen van de fysische knooppunten in de gel.

Een analyse van de lijnbreedte op halve hoogte van de NMR signalen als functie van de temperatuur, duidde duidelijk het overgangsgebied van de keten naar de helix structuur aan in het gebied van 45 °C tot 50 °C. Met deze methode was een toekenning van de hoeveelheid ketens in de helixstructuur echter onmogelijk.

Met NMR relaxometrie metingen kon op basis van een spin-spin relaxatietijd ($T_2$) studie aan iedere verschillende moleculaire mobiliteit de juiste fractie toegewezen worden. Atactisch PMMA (aPMMA) in tolueen, bestudeerd als referentie systeem, had over het hele temperatuurgebied één $T_2$ relaxatietijd voor de _-methyl groep. Voor het mengsel van sPMMA werden er echter twee verschillende $T_2$ relaxatietijden gemeten waarvan er één verdwijnt bij 50 °C.

Aan elke relaxatietijd kon een significante fractie worden toegewezen. De extra $T_2$ relaxatietijd, met een fractie van 25 % die voor sPMMA waargenomen werd, kon worden toegewezen aan de $\alpha$-methyl groepen die zich in de helixfase bevinden. Deze helixfase verdwijnt immers tussen de 45 °C en de 50 °C. De analyse van het methoxy signaal voor aPMMA gaf echter twee relaxatietijden, met een welbepaalde fractie, aan over het hele temperatuursdomein (tot 80 °C). Voor sPMMA werden er drie verschillende $T_2$ relaxatietijden gevonden, elk met een corresponderende fractie. De extra gemeten relaxatietijd voor sPMMA ten opzichte van aPMMA, met een fractie van 25%, was opnieuw de fractie van methoxygroepen die zich in de helixfase bevinden. Een onderzoek van aPMMA in gedeutereerde chloroform ($CDCl_3$), wat een goed solvent is voor PMMA, liet toe de fractie met intermediaire mobiliteit, die niet terug te vinden was voor de $\alpha$-methyl groepen, toe te schrijven aan geïmmobiliseerde estergroepen. Deze estergroepen zijn geïmmobiliseerd door intermoleculaire polymeer-polymeer interacties.
Naast de toekenning van de hoeveelheid ketens in de helixstructuur werden deze resultaten ook gebruikt om een ijking van een infraroodspectroscopie methode uit te voeren zodat deze ook kan gebruikt worden om een kwantificatie van de helixfase te doen. Met deze studie werd aangetoond dat vloeistof NMR door middel van relaxatiestudies een belangrijke bijdrage kan leveren in het opklaren van geleringsmechanismen van polymere systemen.

Een relaxometrie studie in de vaste fase werd uitgevoerd op poly(1,3-dioxalaan)/poly(methyl methacrylaat) (PDXL/PMMA) gesegmenteerde netwerken en mengsels met een verschillende gewichtsfractie aan PDXL (namelijk 20%, 40% en 60%). Deze vergelijkende studie naar de morfologie van deze systemen is uitgevoerd aan de hand van spin-rooster relaxatiemetingen ($T_{1H}$) en spin-rooster relaxatiemetingen in het draaiend assenstelsel ($T_{1\rho H}$). Eenzelfde $T_{1H}$ relaxatietijd voor beide componenten van de netwerken en het mengsel met 20 % PDXL duidden op een homogene fasemorfologie op een schaal van 20 nanometer (nm). Een toename van de hoeveelheid PDXL in de mengsels geeft aanleiding tot fasescheiding op $T_{1H}$ schaal, een verschillende $T_{1H}$ relaxatietijd voor de PDXL fase en de PMMA fase gaven aan dat de gebieden groter dan 20 nm zijn.
De analyse van de $T_{1\rho H}$ relaxatietijden toonden een fasescheiding op een kleinere schaal aan. Voor de fase gescheiden PDXL domeintjes werden twee $T_{1\rho H}$ relaxatietijden gemeten. Voor de netwerken en het mengsel met 20 %

PDXL was één van deze $T_{1\rho H}$ relaxatietijden gelijk aan deze die voor PMMA gemeten werd. Dit komt doordat een deel van de PDXL ketens geïmmobiliseerd zijn door de rigide PMMA fase en zo onderhevig zijn aan spindiffusie. De andere $T_{1\rho H}$ relaxatietijd werd gemeten voor het amorfe PDXL niet onderhevig aan spin diffusie. Deze resultaten duidden aan dat welbepaalde PDXL domeintjes tussen 1 à 2 nanometer ($T_{1\rho H}$) en 20 nanometer ($T_{1H}$) aanwezig zijn in de continue PMMA fase. In de mengsels met een grotere fractie PDXL werd één $T_{1\rho H}$ relaxatietijd toegewezen aan amorf PDXL en de tweede aan kristallijne domeinen die op hun beurt groter zijn dan 1 à 2 nanometer. Deze laatste fase werd eveneens met behulp van DSC-metingen waargenomen. Het specifieke ontmenggedrag voor ieder systeem werd ook in DMA en TGA teruggevonden.

Deze gedetailleerde studie naar de fasemorfologie van de gesegmenteerde netwerken toont de gedwongen compatibiliteit van beide componenten aan. Deze is geïnduceerd door de unieke opbouw van deze netwerken. Veel hoogtechnologische toepassingen van deze materialen zijn gebaseerd op de specifieke morfologie op nanometerschaal. Gericht onderzoek naar deze morfologie kan dan ook in belangrijke mate bijdragen tot een verdere ontwikkeling van deze toepassingen. Hierbij kan een NMR relaxometrie studie substantieel bijdragen daar specifieke informatie over de domeingrootte van polymere netwerken en mengsels in de bulk kan bekomen worden.

Hoofdstuk vier omvat een relaxometrie studie uitgevoerd aan de hand van MRI beelden die gelokaliseerd het gedrag van de polymeerketens onder mechanische spanning weergeven. De plaatjes, met een vooraf aangebrachte breuk, werden in een zelf ontworpen strek-instrument tot yield-spanning getrokken. Dit strek-instrument past in de probe zodat onder spanning gemeten kon worden. Vier verschillende soorten materialen die elk een harde en een zachte polymeerfase bezitten, werden onderzocht. Alleen de zachte fase kon gedetecteerd worden met de spin-echo beeldvorming doordat de magnetisatie van de rigide fase reeds weggerelaxeerd is voordat de echo kan gedetecteerd worden.

In een beeld van ABS (een mengsel van poly(styreen-co-acrylonitrile) (SAN) met 28 gewichtsprocent polybutadieen is de beschadiging van het materiaal tengevolge van de mechanische belasting duidelijk geconcentreerd in banden in het verlengde van de aangebrachte breuk. Een plaatsafhankelijke analyse van de materiaaldichtheid (spin dichtheid) en de $T_2$ en $T_1$ relaxatietijden toonde aan dat de beschadigde banden het gevolg zijn van een daling in de dichtheid van het materiaal. Deze spin dichtheidsdaling is het gevolg van holtevorming in de rubberdeeltjes (cavitatie) als gevolg van de opgelegde spanning. Voor $T_2$ werden geen plaatsafhankelijke veranderingen vastgesteld. Deze sterk geconcentreerde beschadiging is onomkeerbaar.

Het tweede materiaal dat onder belasting onderzocht werd, is een blokcopolymeer van polybutadieen en poly(tetramethyleen oxide) (PBT/PTMO). In de beelden van dit materiaal werd een vrij uitgestrekte en homogeen beschadigde zone zichtbaar. Een plaatsafhankelijke analyse van de spindichtheid en de relaxatietijden toonde aan dat $T_2$ daalde als gevolg van de opgelegde mechanische belasting en dat de dichtheid van het materiaal enkel in de buurt van de breuk afnam. De daling van de $T_2$ relaxatietijd duidde de afgenomen beweeglijkheid van de PTMO ketens aan die gestrekt zijn door de spanning.

Het derde soort materiaal is een mengsel van polyamide 6 (PA6) en ethyleen-propyleen rubber, deze rubber is geënt met maleïnezuuranhydride (EPM-*g*-MA). Van dit materiaal werden twee types bestudeerd: het eerste type had een zuivere EPM-*g*-MA rubber fase in de nylon matrix (Bl-st) terwijl het tweede type in de rubber fase opnieuw PA6 deeltjes bevatte (Bl-oc2). Het Bl-oc2 mengsel bezit een opmerkelijk hogere taaiheid dan het Bl-st mengsel. De beschadiging in dit materiaal was eveneens vrij homogeen maar was minder uitgestrekt ten opzichte van PBT/PTMO. De plaatsafhankelijke bepaling van de materiaaldichtheid en van de relaxatietijden toonden aan dat er een verschillend vervormingsgedrag bij beide types optreedt tengevolge van de aangelegde trekkracht. In het Bl-st mengsel werd enkel een daling van de spindichtheid opgemeten tevens werd er naast deze daling in spindichtheid voor het Bl-oc2 mengsel ook een daling in $T_2$ gemeten. De daling van de spindichtheid is te wijten aan holtevorming in de rubberdeeltjes (cavitatie). De daling in $T_2$ is het gevolg van een daling in de beweeglijkheid van de ketens die teruggevonden werd bij het Bl-oc2 mengsel doordat de PA6 deeltjes in de rubberfase beperking aan de rubberketens oplegden wanneer het staal onder spanning gebracht werd. Deze ketenstrekking bleek de oorzaak te zijn van de verhoogde taaiheid.

Hier werd aangetoond dat met de klassieke spin-echo pulssequentie heel wat informatie kan bekomen worden over cavitatie, de lokale spanningsverdeling in het materiaal en de beweeglijkheid van de rubberketens. Om de harde fase in deze materialen (met zeer korte $T_2$ relaxatietijd) te kunnen meten, moet er

echter gebruik gemaakt worden van technieken zoals 'single point' beeldvorming.
Een verbetering van het binnen de onderzoeksgroep ontworpen strek-instrument zou een betere overeenkomst met de spanning-rek metingen opleveren. Hiervoor dient de wrijving tussen de schroef en de moer en de wrijving tussen de moeren onderling vermindert te worden door middel van een kogellager. Om wrijving tussen het glas en het staal te voorkomen, zou een bredere glasbuis ten opzichte van de breedte van het staal ontworpen moeten worden.

In deze thesis werd aangetoond dat NMR relaxometrie een veelzijdige, niet-destructieve en niet-invasieve techniek is waarmee informatie over de materiaaldichtheid, de moleculaire beweeglijkheid en de morfologie kan bekomen worden. Deze techniek kan zowel in de vloeistoffase als in de vaste fase worden aangewend. Bovendien kan men via een combinatie van beeldvorming en relaxometrie plaatsafhankelijke informatie bekomen over deze materiaaleigenschappen op nanometerschaal.

# 7 List of abbreviations

| | |
|---|---|
| $B_0$ | main magnetic field |
| $B_1$ | spin-lock field |
| $M_0$ | magnetization at time $t = 0$ |
| $M_\infty$ | equilibrium magnetization at time $t = \infty$ |
| $\gamma$ | gyromagnetic ratio |
| I | nuclear spin quantum |
| $\mu$ | magnetic moment |
| $\omega_L$ | Larmor frequency |
| $\tau_c$ | correlation time |
| CT | Contact Time |
| $T_1$ | spin-lattice relaxation time |
| $T_{1\rho}$ | spin-lattice relaxation time in the rotating frame |
| $T_2$ | spin-spin relaxation time |
| TE | Echo Time |
| TR | Repetition Time |
| FID | Free Induction Decay |
| CP | Cross Polarization |
| MAS | Magic Angle Spinning |
| sPMMA | syndiotactic poly(methyl methacrylate) |
| aPMMA | atactic poly(methyl methacrylate) |
| PDXL | polydioxalane |
| ABS | acrylonitrile butadiene styrene |
| PBT | poly(butadiene terephthalate) |
| PTMO | poly(tetramethylene oxide) |
| PA6 | polyamide 6 |
| EPM | ethylene propylene rubber |
| MA | maleic anhydride |